VTT

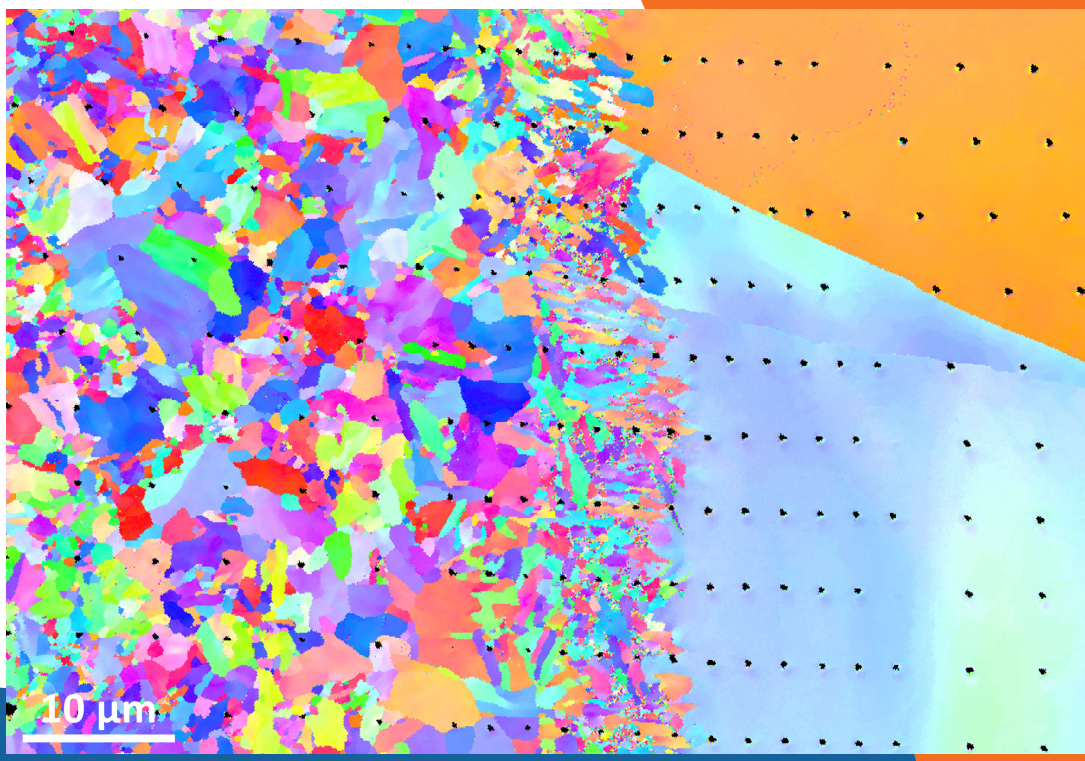

Forum for the Effect of Thermal Aging and Microstructure on Mechanical and EAC Behaviour of Ni-base Alloy Dissimilar Metal Welds (FEMMA)

Zaiqing Que | Sebastian Lindqvist | Noora Hytönen | Yanling Ge | Pekka Nevasmaa | Jari Lydman | Laura Sirkiä | Pentti Arffman | Antti Forsström | Ulla Ehrnstén

VTT TECHNOLOGY 420

VTT TECHNOLOGY 420

Forum for the Effect of Thermal Aging and Microstructure on Mechanical and EAC Behaviour of Ni-base Alloy Dissimilar Metal Welds (FEMMA)

Zaiqing Que, Sebastian Lindqvist, Noora Hytönen, Yanling Ge, Pekka Nevasmaa, Jari Lydman, Laura Sirkiä, Pentti Arffman, Antti Forsström, Ulla Ehrnstén

VTT Technical Research Centre of Finland

VTT

ISBN 978-951-38-8783-4

VTT Technology 420

ISSN-L 2242-1211
ISSN 2242-122X (Online)
DOI: 10.32040/2242-122X.2023.T420

JULKAISIJA – PUBLISHER

VTT
PL 1000
02044 VTT
Puh. 020 722 111
https://www.vtt.fi

VTT
P.O. Box 1000
FI-02044 VTT, Finland
Tel. +358 20 722 111
https://www.vttresearch.com

Preface

The FEMMA (Forum for the Effect of Thermal Aging and Microstructure on Mechanical and EAC Behaviour of Ni-base Alloy Dissimilar Metal Welds) project is primarily addressed to the needs of the nuclear power plant industry, and it is a fifth consecutive cooperative project on dissimilar metal weld (DMW) topics. The earlier projects, ERIPARI, PERDI, SINI and NIWEL covered topics like weldability, hot cracking, environment-assisted cracking and structural integrity of Ni-base Alloy DMWs. The main focus of the FEMMA project is to assess the effects of thermal aging and welding technique on the performance of Alloy 52 DMWs.

The long-term behaviour of the DMWs is of particular interest in Finland and Sweden because there are nuclear power plants that are at critical stages of their lifetime: either beginning their operation or reaching lifetime extensions. In both cases, understanding of the aging phenomena is of utmost importance to ensure safe operation for lifetimes that can reach 60 years or even beyond that.

The narrow-gap DMW without a buttering layer in the OL3 EPR plant safe-end is a first-of-a-kind design. The Ringhals DMW mock-up consisting of Alloy 52 buttering on both sides, which is representative of Ringhals pressurizer surge nozzle DMW repair solution, is also a first-of-a-kind in Europe. Therefore, their characteristic microstructural features as well as mechanical performance must be studied carefully. It has been shown earlier that thermal aging and welding technique cause changes in the properties of the DMWs in elevated temperature long-term service. Thus, the main aim of the FEMMA project is to characterize the properties, both microstructural and mechanical, of two fully representative DMW mock-ups before and after thermal aging.

Developing and maintaining the knowledge of DMW-related issues is vital for the Nordic nuclear power industry. Taking part in the most important international forums and dissemination of the experiences to the industry has been an essential theme for the FEMMA project, as well as developing research competence in Finland and Sweden. Many younger generation researchers have been introduced to the field of DMW research during the project. A prerequisite for the plant-relevant, high-quality work is to access the relevant industrial materials. Without the commitment of the nuclear industry stakeholders, providing the materials, as well as giving guidance to the most important topics, the project would not have been possible.

Contents

Preface **3**
Contents **4**
List of symbols **7**
1 Introduction **11**
1.1 DMWs in nuclear power systems 11
1.2 SCC of DMWs 12
1.3 Interface features of DMWs 12
1.4 Thermal aging of DMWs 13
2 The studied DMW mock-ups **16**
2.1 TVO mock-up 16
2.2 Ringhals mock-up 19
3 Microstructural characterization of the DMW mock-ups **21**
3.1 Characterization methods 21
3.2 Microstructural characterization of TVO mock-up 23
3.2.1 NG DMW general microstructure and microhardness 23
3.2.2 CPZ microstructure and carbide analysis 26
3.2.3 CDZ microstructure and carbide analysis 32
3.2.4 HAZ microstructure and carbide analysis 34
3.2.5 WAXS of carbides in HAZ 38
3.2.6 APT analysis 39
3.3 Microstructural characterization of Ringhals mock-up 42
3.3.1 Macro-, micro- and nano-hardness measurements 42
3.3.2 Fusion boundary characterization 45
3.3.3 Carbide analysis 50
3.3.4 XRD measurements for tempered martensite FB 57
4 Fracture mechanical testing **60**

4.1 Specimens and methods 60
4.1.1 Test matrix and specimens 60
4.1.2 Extraction of the specimens 63
4.1.3 Tensile testing 68
4.1.4 J-R testing according to ASTM E1820 71
4.1.5 T_0 testing according to ASTM E1921 72
4.1.6 Charpy-V testing 73
4.1.7 Metallography, crack path and fractography 76
4.2 Fracture mechanical tests of TVO mock-up 77
4.2.1 Fractography and crack/notch location 77
4.2.2 T_0 fracture toughness 81
4.2.3 Discussion on T_0 for 15 000 h aged condition 85
4.2.4 Impact toughness 88
4.3 Fracture mechanical tests of Ringhals mock-up 90
4.3.1 Tensile tests 90
4.3.2 J-R curves for Ringhals mock-up 99
4.3.3 Ductile-to-brittle transition testing 103
4.3.4 Macroscopic homogeneity screening of the T_0 data 109
5 Discussion 111
5.1 TVO mock-up 111
5.1.1 Microstructure and carbides of TVO mock-up 111
5.1.2 Fracture mechanical behaviour of TVO mock-up 113
5.2 Ringhals mock-up 120
5.2.1 Fusion boundary microstructure of Ringhals mock-up 120
5.2.2 Microstructure on local mechanical properties 123
5.2.3 Fracture mechanical behaviour of Ringhals mock-up 124
6 Conclusions 127
6.1 TVO mock-up 127
6.2 Ringhals mock-up 128
6.3 Future work 130
Acknowledgements 132
References 133
Appendix A: Publications and oral presentations from FEMMA project 140

List of symbols

a_0	Initial crack length
a_p	Final crack length
APT	Atom probe tomography
AR	As-received
ASME	American Society of Mechanical Engineers
b	Specimen thickness
BCC	Body-centre cubic
BCT	body-centre tetragonal
BF	Bright-field
BM	Base metal
BSD	Backscatter detector
BSE	Backscattered electrons
CDZ	Carbon-depleted zone
CMOD	Crack mouth opening displacement
CPZ	Carbide precipitation zone
CVN	Charpy-V notch
C(T)	Compact tension
DBTT	Ductile-to-brittle transition temperature
DDC	Ductility dip cracking
DF	Dark-field
DMW	Dissimilar metal weld
Δa	Crack growth

EAC	Environmentally-assisted cracking
EBSD	Electron backscatter diffraction
EDS	Energy dispersive X-ray spectroscopy
EDM	Electrical discharge machining
ε	Strain
Fa	Arrest force
F_m	Maximum force
F_u	Initiation force
FB	Fusion boundary
FCC	Face-centre cubic
GTAW	Gas tungsten arc welding
HAADF	High-angle annular dark-field
HAZ	Heat-affected zone
IPF	Inverse polar figures
J	J-integral
J_{1mm}	J-integral at 1 mm of ductile crack growth
J_{3mm}	J-integral at 3 mm of ductile crack growth
J_{IC}	value of J-integral near the initiation of stable crack growth, a size independent value of fracture toughness
J_Q	value of J-integral near the initiation of stable crack growth, interim fracture toughness or fracture resistance
KAM	Kernel average misorientation
K_{Jc}	Stress intensity factor
L	Length
LAS	Low alloy steel
LOM	Light optical microscopy
NDE	Non-destructive examination
NIZ	Near-interface zone
NG	Narrow-gap
NPP	Nuclear power plant
OES	Optical emission spectroscopy

PMZ	Partially-mixed zone
PWHT	Post-weld heat treatment
PWSCC	Primary water stress corrosion cracking
RSM	Reciprocal space maps
SE	Secondary electrons
SEM	Scanning electron microscope
SS	Stainless steel
STEM	Scanning transmission electron microscope
σ	Stress
σ_{TS}	Tensile strength
σ_{YS}	Yield strength
SCC	Stress corrosion cracking
SE(B)	Single edge-notched bend
T_0	Ductile-to-brittle transition temperature based on fracture toughness
T	Temperature
TA	Thermal aging
T_{28J}	CVN 28 J transition temperature
T_{41J}	CVN 41 J transition temperature
T_{fa4}	Reference temperature for arrest force
T_{KIa}	Temperature
TEM	Transmission electron microscope
USE	Upper-shelf energy
v	Poisson's ratio
W	Specimen width
WAXS	Wide-angle X-ray scattering
WD	Working distance
WM	Weld metal
XRD	X-ray diffraction

1 Introduction

1.1 DMWs in nuclear power systems

The main structural materials used in the components and piping of primary circuits of the pressurized water reactors (PWRs) are ferritic low alloy steels (LAS), stainless steels and nickel-base alloys [1]. LAS alloyed with low contents of Cr, Ni, Mo and V can reach high strength levels and are used for structural components [2], of which the most important is the reactor pressure vessel (RPV). Austenitic stainless steels are used for structural components (Types 304, 304L, 316 and 316L) and as a corrosion-resistant cladding of the RPV and pressurizer (Types 308 and 309). Nickel-base alloys are used for high-strength components where good corrosion properties are required, some critical applications and welds. In a dissimilar metal welds (DMW), these three materials of different composition and crystal structure are joined. A typical example of a DMW is the RPV nozzle to safe-end weld between the SS-cladded RPV ferritic LAS and an austenitic stainless steels pipe, using a Ni-base filler metal.

DMWs can be potential concerns regarding the structural integrity of the nuclear power systems, structures and components [3] [4] [5]. The amount of information available in the open literature on the microstructural and fracture mechanical changes occurring at the fusion boundary (FB) after buttering, welding, and post-weld heat treatment (PWHT) is relatively limited and often very case dependent [6]. In particular, the knowledge on the local strength mismatch at the LAS/Ni-based alloy weld metal (WM) interface upon PWHT and during long-term ageing is lacking [7] [8]. There are challenges to accurately characterize the local mechanical behaviours of the different materials constituting the DMW [9]. The effect of FB microstructure on the performance of DMWs has been a topic of increased interest in the nuclear power community [10] [11]. Despite various studies have been conducted, some important questions remain to be confirmed or answered.

The two-sided Alloy 52 buttering welding technique and subsequent PWHT exhibit different microstructures at the weld FBs compared to the other welding techniques, *e.g.* narrow-gap (NG) weld without buttering [12] [13].

1.2 SCC of DMWs

DMWs are important from the design and performance point of view. However, they have been related to a number of incidents involving intergranular stress corrosion cracking (IGSCC) [14] [15] [16], with sensitized microstructures found in SS and Ni-base alloy safe-ends and within WMs [17] [18]. Nickel-base WMs such as Alloys 182 and 82, with a composition similar to wrought Alloy 600, have increased the service life of DMWs by reducing carbon migration at the interface and differential expansion strains [19]. They are, however, susceptible to IGSCC and cracking incidents, involving Alloys 600 and 182 in the RPV safe ends and head penetrations as well as steam generators, have been observed in many plants due to the presence of corrosive environment, high temperature, residual stresses/strains, and material sensitization effects [14] [16]. While crack propagation along the DMW interface is most often limited to the WM and the cracks typically grow in axial orientation of the pipe in safe-end weld cracking incidents [20], an increasing susceptibility to loss of ductility has been observed especially at the weld interface region [21]. In order to improve the SCC resistance, Alloy 690 has replaced Alloy 600 in steam generator tubes and vessel head penetration tubes. The filler metals Alloy 52, 152 and 52M were developed based on the composition of Alloy 690 and are nowadays used in DMWs. Due to the higher chromium content, they show a better SCC resistance than Alloys 182 and 82, with marked improvement in crack initiation times and SCC crack growth rate [22].

Moreover, there is still limited data available for the behaviour of the DMWs manufactured using high-Cr Ni-based Alloy 52 WM (based on wrought Alloy 690 composition) [23], in replacement of the earlier used Alloy 182/82 WMs (based on wrought Alloy 600 composition) [10]. Though Alloy 52 itself has higher environmentally-assisted cracking (EAC) resistance than Alloy 182 [24], the electrochemical potential gap and thus the galvanic corrosion susceptibility of Alloy 52/LAS is higher than Alloy 182/LAS [25].

1.3 Interface features of DMWs

The welding techniques and parameters of DMW studies in the majority of the research programs are different from the ones used in real NPPs, which may result in completely different microstructure and mechanical properties [26] [27]. A detailed study of FB microstructure and local mismatch of NPP relevant DMW mock-ups need to be performed.

The difference in the crystal structure between bainitic reactor pressure vessel steel with body-centre cubic (BCC) crystal structure and austenitic WM with face-centre cubic (FCC) crystal structure result in a crystallographic mismatch at the FB and a significant chemical composition gradient, specifically carbon (C) and chromium (Cr), at the dissimilar metal interface. Therefore, a complex microstructure and a physical and mechanical properties mismatch (*e.g.* corrosion and strength) are formed at the interface [28] [29] [30]. The reduced chromium and

nickel contents in the transition region due to the dilution effects are assumed to increase the SCC susceptibility [31], while the formation of hard and soft layers, driven by the composition gradients, lead to lower strength area in the carbon-depleted zone (CDZ) and increase the strength mismatch at the interface [32] [33] [34]. Furthermore, the metal dissimilarity at the FB can cause residual stresses due to the thermal mismatch at weld solidification and subsequent cooling [35]. Different microstructural regions can be identified in the complex DMW interface such as heat-affected zone (HAZ), CDZ, partially-mixed zone (PMZ) and carbide precipitation zone (CPZ) [7] [21], *etc*. As a result of PWHT, adjacent to the FB are the CDZ grains from which carbon has diffused to the low-C/high-Cr Ni-base weld metal side of the interface and normally it exhibits the lowest hardness across the FB [36]. Simultaneously, carbon pile-up in CPZ happens close to the FB due to the low diffusivity of carbon in the nickel matrix [37].

The mechanical properties in the interface zone between SA 508 and Alloy 52 are affected by the local and global strength mismatch and the local microstructures [8]. A typical feature of DMWs is that the crack does not grow along the initial pre-crack plane in a test specimen but can deviate to adjacent locations. In single edge-notched bend (SE(B)) specimens of Alloy 52 NG DMWs, HAZ cracks approximately 0.5 mm from the FB can deviate from the initial crack growth plane to the FB with lower tearing resistance than the adjacent zones or bulk materials [38] [37]. Since the crack tends to grow towards the material region with lower strength [33], HAZ cracks further than 0.5 mm from the FB can also grow from the hard HAZ towards the softer base material. The crack deviation towards the FB is controlled by the strength mismatch but is also affected by residual stresses and the microstructure. The strength mismatch affects the local constraint which is observed as localization of the stress triaxiality and the plastic strain ahead of the crack. Plastic damage is promoted in the regions with high stress triaxiality and plastic strain.

Understanding the effects of the welding techniques and materials on the detailed FB microstructures and local mechanical properties are crucial for the assessment and improvement of nuclear component integrity and development of repair welding solutions to ensure safe long-term operation of nuclear power plants (NPPs) [39] [40]. Furthermore, the segregation of impurity elements during heat treatment and ageing, such as phosphorus segregation in the HAZ [13] [41] and carbide diffusion to the type-II boundaries together with the residual stresses and strains at the interface, are known to increase susceptibility to cracking and stress corrosion cracking (SCC) [42] [43]. The roles of FB structures and types and how they promote or reduce weld-related cracking remains still unclear [44].

1.4 Thermal aging of DMWs

Of the materials in the DMW, ferritic LAS reactor pressure vessel (RPV) steel is considered to be the most important from thermal ageing point of view, due to its ductile-to-brittle transition (DBT) behaviour and tendency to thermal embrittlement. Several different processes can lead to thermal embrittlement and degradation of

the fracture mechanical properties of the RPV steel during long periods of operation in high (325 °C) temperature. Those mechanisms include precipitation hardening, such as precipitation of copper-rich phases, phosphorous segregation at the grain boundaries leading to intergranular fracture, solution of cementite and widening of the CDZ leading to softening of the LAS in that region, and segregation of impurities to dislocations leading to strain ageing [45]. Of these processes, phosphorous segregation is assumed to have the most significant effect on the behaviour of DMW [13]. Hudson *et al.* [46] showed that thermal ageing causes phosphorous segregation at the grain boundaries of LASs, which degrades the fracture toughness and impact toughness of the material.

The thermal stability of Alloy 690 and its WMs (Alloys 152 and 52) in the long-term operation of NPPs, operating as long as 60-80 years, remains an important topic of research [47]. The susceptibility of welds to SCC depends not only on the properties of the base and WMs, but also on the microstructural changes taking place at the interface during welding and PWHT [48]. Thermal ageing can also affect the SCC susceptibility of Alloy 690 and its WMs. In particular, there is still little knowledge on the long-term behaviour of these interfaces since no in-service experience is available, yet, and very few laboratory investigations have been performed on aged materials. Therefore, it is essential to characterize the microstructural changes occurring at the RPV nozzle to safe-end ferrite/austenite interface upon thermal ageing.

Most of the thermal aging data for Mn-Mo-Ni LASs (like SA 508, A533, 18MND5 and 16MND5) indicates that the materials are resistant to thermal aging in the temperature range of 260–320 °C for an aging time of 100 000 h and even up to 250 000 h. However, for a few LASs, a shift of 60 °C in ductile-to-brittle transition temperature (DBTT) was reported [49]. In these cases, the alloys were not given a proper PWHT or quench-and-temper heat treatment, or the reference and aged materials were sampled from different depths in thickness direction. These exceptions underline the need to investigate and understand the effects related to thermal aging.

An exceptionally high P or Ni content can result in a significant shift in DBTT due to thermal aging. Ni can affect the grain boundary absorption capacity of P atoms and increase the sensitivity to thermal embrittlement [50]. The DBTT shifted with 150 °C for a Mn-Mo-Ni LAS containing 1.7% Ni, after aging at 330 °C for 20 000 h. VVER-1000 forgings and WMs, Cr-Ni-Mo LASs, with Ni > 1.3 %, show shifts up to 30 °C after thermal aging at 310–320 °C for 200 000 h [51]. The effect of Ni on the aging behaviour has been connected to synergetic effects with other elements, *e.g.* Mn [52] [53].

P segregation to the grain boundaries is considered to be the main thermal aging mechanism for LAS in NPPs. Therefore, the P content has been restricted to 0.015% and later to 0.008% [54]. Thermal aging of LAS in NPPs is to a minor extent affected by segregation of other interfacial mobile elements, and other mechanisms, like hardening and strain aging [55]. As the LAS is subjected to a relatively high temperature, the amount of P on the grain boundaries increases with aging time. P segregation to grain boundaries is connected to an increase in the ratio of

intergranular fracture and a larger shift in DBTT. A larger P content in the matrix enhances the P segregation to the grain boundaries, which is also dependent on the initial P content on the grain boundaries [56]. However, a larger P content in the matrix (0.007 versus 0.016%) does not always lead to a larger shift in DBTT [57].

Besides the chemical composition and the aging temperature, thermal embrittlement is affected by the heat treatment, the resulting microstructure and aging time [46] [58]. Typically, due to the heat treatment, the coarse-grained WM and HAZ are considered to be more prone to thermal aging [55]. Compared to the base metal (BM), the sensitivity of the HAZ to thermal aging can be 3–6 times higher at 330 °C [59]. BMs are considered less vulnerable to temper embrittlement due to a finer prior austenitic grain size and the heat treatment consisting of quenching and tempering. Lower DBTTs are obtained when the grain size is smaller, 66 µm compared to 430 µm [57]. Yet, the shift in DBTT is not always dependent on the grain size. For the HAZ of a submerged-arc weld with 18MND5 as BM, the largest shift is reported to occur at 1 mm from the FB in the fine-grained HAZ region, and not in the grain-coarsening region [60].

The carbides formed at the FB and in the LAS HAZ can act as brittle fracture initiators and thus the type, morphology and size of carbides significantly influence the brittle fracture behaviour [61]. In addition, hardness mismatch at the DMW FB was governed by the change of precipitate morphology and size due to dislocation cutting or bowing phenomenon [25]. However, the amount of information available in the open literature on the microstructural changes and carbides formation occurring at the FB upon PWHT and during long-term thermal ageing is very limited [7] [8] [9]. Furthermore, the segregation of impurity elements during heat treatment and ageing and carbon diffusion from LAS to Alloy 52, are known to increase susceptibility to cracking and SCC [42] [43]. Moreover, the NG weld without buttering and subsequent PWHT exhibit different microstructures at the FB and HAZ compared to Alloy 52 buttering welding technique [12] [13]. Understanding the effects of long-term thermal aging on the detailed FB microstructures and carbide formation are crucial for the integrity evaluation and safe long-term operation of nuclear components with NG DMW [39] [40].

2 The studied DMW mock-ups

In this study, two different DMW mock-ups representative of actual component weld solutions in Nordic NPPs are investigated, *i.e.* the TVO mock-up and the Ringhals mock-up.

2.1 TVO mock-up

The TVO mock-up is an industrially manufactured 1:1 scale DMW safe-end mock-up. The shape of the mock up is a ring, thus enabling it to be fully representative to the real component. The FB of specific interest, SA 508 - Alloy 52 weld FB, is located roughly in the middle of the mock-up. The technical details of the DMW mock-up are given in Table 1. The weld is manufactured by applying the NG gas tungsten arc welding (GTAW) method without buttering and using Alloy 52 as welding consumable. The joint is welded one bead per layer. After welding, the mock-up was post-weld heat treated at 550 °C for 890.4 min and at 610 °C for 458.4 min. The mock-up is ~9 mm wide and ~94 mm thick. The mock-up consists of an Alloy 52 NG weld joining SA508 nozzle and stainless steel AISI 316LN safe-end. The inner surface of the LAS wall has a 308L stainless steel cladding. The chemical compositions of the materials are presented in Table 2.

Table 1: Technical details of the NG mock-up investigated.

	TVO NG mock-up
Nozzle	SA508 Gr.2
Cladding	SS308L/309L
Weld	Alloy 52 NG
Safe-end	AISI 316LN
PWHT	17 h at 550 °C + 7h at 610 °C
Welding method	TIG welding
Conditions	PWHT or thermal aged at 400 °C for 15 000 h

An optical cross-section image of the mock-up showing the SA 508 LAS, AISI 308 cladding, Alloy 52 WM and AISI 316L stainless steel is presented in Figure 1 together with a higher magnification optical image showing the LAS HAZ. Also, the directions used for determining the orientations are seen in Figure 1.

Table 2. Chemical compositions (in wt.%) of the materials used in the DMW mock-up (courtesy of Areva).

	16MND5/SA 508	**AISI 316L**	**AISI 308L**	**Alloy 52**
C	0.18	0.021	0.007	0.023
Si	0.19	0.40	0.37	0.15
Mn	1.42-1.46	1.62	1.9	0.26
P	0.005	0.020	0.013	<0.005
S	0.001	0.002	0.001	0.0007
Cr	0.11-0.12	17.23	20.3	29.93
Ni	0.76-0.78	11.56	10.3	58.86
Mo	0.49-0.50	2.34	0.1	<0.01
Nb				<0.01
N		0.067	0.04	0.021
Ti				0.54
Fe	Bal.	Bal.	Bal.	10.43
Al	0.02			0.66
Co	0.01-0.02	0.022		<0.01
As	0.003-0.005			
Sn	0.003-0.004			

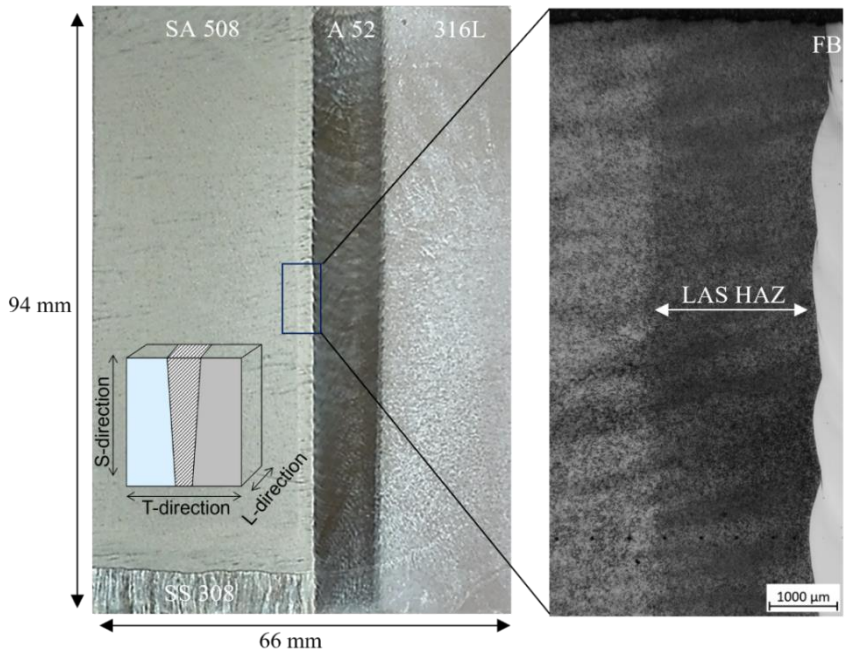

Figure 1. An optical image on the left, showing the cross-section of the NG DMW mock-up, and a larger magnification optical image on the right, where the HAZ, FB and nominal pre-crack location are shown. The directions used for determining the specimen orientations are schematically presented in a drawing on the left.

The DMWs located in the outlet pipe of the reactor pressure vessel are subjected to a temperature of 330 °C that increases the susceptibility to thermal embrittlement. In the pressurizer, the temperature can be up to 350 °C. Thermal ageing was conducted in a furnace at 400 °C for an additional 5000 h on top of the 10 000 h thermal aging conducted in NIWEL project. The temperature during thermal ageing was monitored using thermocouples and stayed within about ±1 °C during the thermal treatment. The validity of the thermal ageing temperature 400 °C was evaluated based on the possible known mechanisms, which are segregation of impurities to the grain boundaries, strain ageing and carbide coarsening. The ageing times were chosen based on the assumption that phosphorous segregation is the main mechanism controlling the degradation of fracture toughness of the pressure vessel steel during ageing. Phosphorous segregation is enhanced at 400 °C without changing its mechanism, compared to the operation temperature. According to the calculations presented by Joly *et al.* [13], the ageing time of 15 000 h at 400 °C is representative to about 90 years of operation at 325 °C from the phosphorous segregation point of view.

2.2 Ringhals mock-up

Ringhals mock-up is a DMW mock-up consisting of Alloy 52 buttering on both sides, which is representative of Ringhals pressurizer surge nozzle DMW repair solution. It consists of nozzle material SA508M Grade 2 Class 1, Ni-based Alloy 52 buttering weld, Alloy 52 V-groove weld, Alloy 52 buttering weld, joined to the austenitic stainless steel 316LN safe-end. The inner surface of the nozzle LAS is cladded with stainless steel (SS) 308L. The illustrative figure of the DMW structure is shown in Figure 2. The LAS side with buttering weld was subjected to PWHT at 615 °C for 1 hour 17 minutes with heating and cooling rates of 55 °C/h from 300 °C. The V-groove weld and stainless-steel side buttering were welded at a workshop afterwards. The butterings were welded in transverse orientation and the V-groove in longitudinal orientation. The welding parameters can be found in Table 3. The chemical compositions of each material in the DMW provided by Ringhals were verified with glow-discharge optical emission spectroscopy (GD-OES) and are given in Table 4.

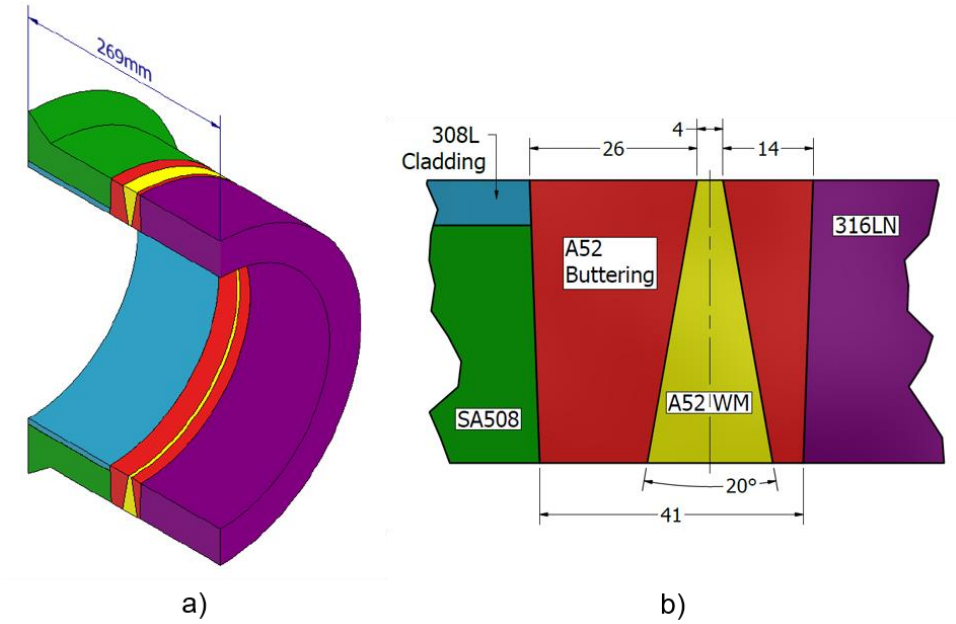

Figure 2: The illustrative figure showing (a) the location of the weld in the surge nozzle safe-end and (b) the DMW structure. All dimensions are in millimetres.

Table 3. Welding parameters for the investigated DMW.

Welding process	Mechanized Gas Tungsten Arc Welding
Welding position	"Horizontal" – PC
Wire diameter	0.9 mm
Shielding gas	Argon
Type of current	DC
Interpass temperature (max)	100 °C
Heat input	0.67–1.49 kJ/mm

Table 4. Chemical composition of the LAS nozzle and Ni-based WMs materials provided by Ringhals. The GD-OES analysis was applied to verify the chemical compositions in SA508 and Alloy 52 buttering weld.

	SA508M Gr.2 Cl1		**Alloy 52**	
	Nozzle	**GD-OES**	**Buttering**	**GD-OES**
C	0.20	0.23	0.029	0.034
Cr	0.35	0.36	28.94	30.24
Mo	0.63	0.75	<0.01	<0.02
Ni	0.87	0.93	Bal.	Bal.
Mn	0.91	0.98	0.29	0.37
Si	0.23	0.25	0.16	0.15
P	0.008	0.015	<0.003	<0.003
S	0.004	0.004	<0.0005	<0.0005
Al	0.019	-	0.73	0.79
Ti	-	0.002	0.5	0.7
Cu	0.05	0.05	<0.1	<0.2
V	0.01	0.009	-	-
Nb	-	-	<0.002	-
Fe	Bal.	Bal.	9.2	10.6

3 Microstructural characterization of the DMW mock-ups

Various advanced characterization methods have been applied to investigate the microstructure of the DMW mock-ups [62] [63]. The characterization methods are introduced in Chapter 3.1. The results of the microstructural characterization of TVO and Ringhals mock-ups are shown in Chapter 3.2 and 3.3, respectively.

3.1 Characterization methods

Samples covering the LAS base material, HAZ, PMZ, UMZ and the WM were extracted for microstructural characterization using electrical discharge machining (EDM). Samples were ground with Struers SiC grinding papers up to 4000 grit and then polished with 3 µm, 1 µm and 0.25 µm Struers DiaPro diamond solutions. Vibratory polishing with Buehler VibroMet in a colloidal alkaline suspension (MasterMet 2 non-crystallizing amorphous 0.02 µm colloidal silica suspension) was used as final polishing to remove the last deformation layers from grinding.

Light optical microscopy (LOM) and scanning electron microscopy (SEM) were used to characterize the microstructures. The metallographic microstructure was examined using LOM after etching the specimen. The LAS was etched with Nital 3% and the Alloy 52 with aqua regia (HNO_3 + HCl + glycerol). A Zeiss Crossbeam 540 equipped with a solid-state four-quadrant backscatter detector (BSD) and an EDAX Hikari Plus EBSD detector was used. The near-surface FB microstructure was investigated using SEM secondary electrons (SE) and backscattered electrons (BSE) imaging techniques. BSE imaging was conducted at an acceleration voltage of 15 keV with a working distance (WD) of 6–7 mm and a probe current 1.5–3.0 nA. Electron backscatter diffraction (EBSD) was used for grain size measurement. EBSD mapping was conducted at an acceleration voltage of 15 keV and a WD of 13–15 mm with 70° tilting and a probe current of 1.5 nA. The EBSD phase maps, inverse polar figures (IPF), Kernel average misorientation (KAM) maps by TSL OIM Analysis 8 software. Energy dispersive X-ray spectroscopy (EDS) was used to characterize the composition gradients at the weld interface. To reduce the interaction volume between incident electrons and matrix, the EDS line scan with an accelerating voltage of 5 keV and a probe current of 1.5 nA was applied to obtain

local chemical differences across the FB from LAS to the weld with a measurement step size of 200 nm.

Microhardness and nanoindentation measurements were carried out with instrumented testers to study hardness profiles across the LAS HAZ and the weld interface. Microhardness measurement was performed using Struers DuraScan-80 hardness measurement device. Nanoindentation maps were measured with Anton Paar UNHT. Microhardness measurements were done with a Vickers tip using an indentation load of 350 mN and a 50 µm step size, while nanoindentation measurements were performed with a Berkovich tip using an indentation load of 1.5 mN and a 5 µm step size. The nanoindentation mappings cover distance of ~120 µm in the SA508 side (over the CDZ) and ~50 µm in the Alloy 52 buttering side measured from the FB. The step size is 2.5 µm in the area close to FB and 5 µm for the rest of the mapping area. The line spacing is constant at 5 µm.

Transmission electron microscope (TEM) was used to characterize the carbides. The specimen was cut by EDM to a thickness of ~0.5 mm and mechanically thinned to ~100 µm. The final thinning was carried out by twin jet electropolishing using a Struers TenuPol-5 electropolisher with an environmentally friendly salt-based electrolyte. The electrolyte consists of 1 M concentration of NaCl in ethylene glycol and 200–400 ml ethanol. Scanning TEM (STEM) high-angle annular dark-field (HAADF) and bright-field (BF) images and chemical information of carbides were acquired on FEI Talos F200X STEM equipped with Super-X EDS system operating at 200 kV. Some of thin foils were further ion milled to obtain thin area near the FB by Gatan Precision Ion Polishing System (PIPS, model 691).

The different phases, *i.e.*, BCC SA508, FCC Alloy 52 and BCC tempered martensite, at FB region were studied with XRD. A set of high-resolution reciprocal space maps (RSM) were collected from LAS to Ni-based alloy across FB with Rigaku SmartLab diffractometer. The parallel beam size of about 200–250 µm was used with a 0.2 mm collimator on the incident beam and a two-dimensional (2D) detector without optics on the diffracted beam path. Wide-angle X-ray scattering (WAXS) was performed with a Xenoxs Xéuss 3.0 system with Mo tube. Selected TEM foils were also studied with WAXS in transmission mode with Mo tube of 700 µm beam size. The measured area is located at HAZ. The 2D WAXS patterns are integrated and converted into 1D profiles and refined with MAUD program [64].

The atom probe tomography (APT) measurement was carried out at Chalmers University of Technology. The APT specimens were electropolished using a standard two-step method. A LEAP 3000X HR with a detection efficiency of 37% was used for the APT analysis. The pulse frequency was 200 kHz, the pulse fraction was 20%, and the temperature 70 K. For the reconstruction and analysis, IVAS 3.6 was used. Care was taken for the analysis of the P content. P evaporated mostly as P^{2+} and P^{3+}. P^{+} was also included in the deconvolution of peaks as it overlaps with Ni^{2+}. It was found to not give a significant contribution to the P content.

3.2 Microstructural characterization of TVO mock-up

The microstructure and carbides type, morphology and size in the CPZ (up to 1.5 µm from FB), CDZ (up to 40–50 µm from FB) and HAZ (up to 2 mm from FB) of TVO DMW in post-weld heat-treated and thermally-aged (400 °C for 15 000 h) conditions are analysed with various methods including analytical electron microscopy, wide-angle X-ray scattering and APT [65]. The investigated conditions are as-received post weld heat-treated condition ("NG AR") and the thermally aged condition after 15 000 h at 400 °C ("NG TA"). The effects of long-term thermal aging on the microstructures and carbide formation and the fracture mechanical behaviour are discussed in Chapter 5.1.

3.2.1 NG DMW general microstructure and microhardness

The general microstructure of the NG DMW is shown in Figure 3. The LAS and WM were etched with different reagents. In Figure 3, (a) shows the LAS side etched and (b) shows the A52 weld. In Figure 3(a), the HAZ is ~2.5 mm wide and mild ghost lines, *i.e.*, macro-segregations, appear in the SA508 base material (BM) and HAZ can be observed in NG mock-up. In Figure 3(c-e), the HAZ and FB are shown, revealing the CDZ and grain-coarsened region adjacent to the FB. In Figure 3(b), the multi-pass NG weld appears with large A52 grains growing across the weld beads. One weld bead is highlighted in the Figure 3(b). The FB undulates with the subsequent weld beads.

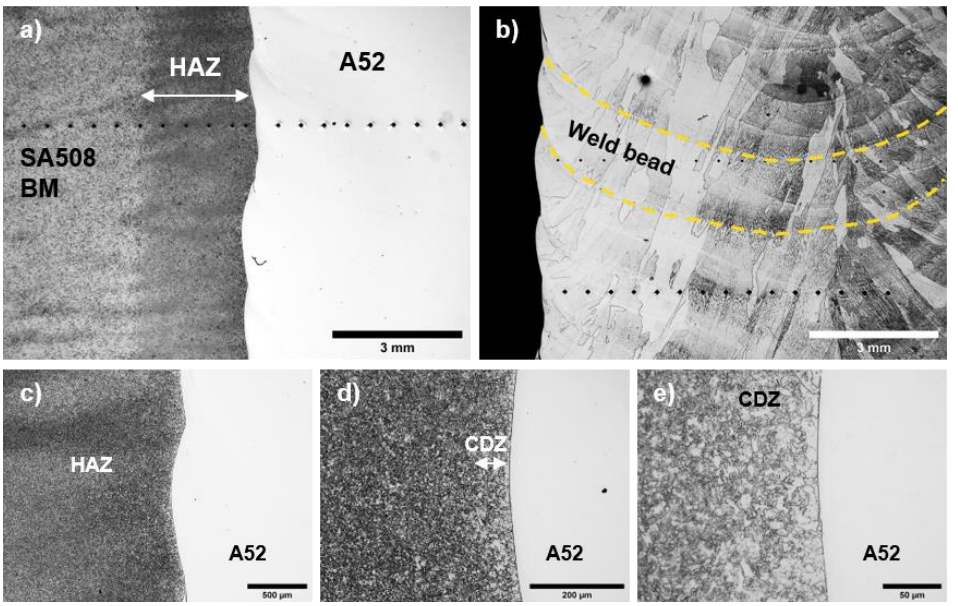

Figure 3: Metallographic microstructure of the NG DMW, where (a) LAS-side is etched, (b) A52 is etched showing weld beads, (c-e) shows the HAZ and CDZ with increasing magnifications. The dark dots seen in the pictures are hardness indents.

The FB of the NG mock-up was further characterized using SEM and EBSD, shown in Figure 4. Two types of FBs were analysed, *i.e.*, the narrow straight typical FB without any distinctive transition zone (Figure 4(a-d)), and the PMZ and swirl (Figure 4(e-h)). There is evident grain coarsening with a distance up to few tens of µm from the narrow straight typical FB. With a swirl along the FB, the coarsening is slightly milder. In the phase map, the mixing of BCC and FCC phases is shown, with some uniform BCC LAS present in the swirl as well. The PMZ area has some level of residual strain as shown in the KAM-map, which are less evident in the fully BCC part. A large swirl may decrease the resistance to local FB debonding and crack propagation.

As shown in Figure 5, the general microstructure and precipitations of the FB CPZ (0.5–1.5 µm from FB), CDZ (40–50 µm from FB) and HAZ (up to 2 mm from FB) of SA508/Alloy 52 were investigated using the TEM foils with SEM. At the FB in the LAS side, fine CPZ about a few hundred nanometre wide was formed (more discussion in Chapter 3.2.2). It is noted the fine carbides in the CDZ (more discussion in Chapter 3.2.3) are mostly located in small grains whereas large grains are almost carbide-free. In the HAZ (more discussion in Chapter 3.2.4), the grain size is further decreased with increased distance to the FB and carbides distribution tends to be more homogeneous. Carbides are formed both at grain boundaries and within grains in the HAZ. A moderate difference in the microstructure in the CDZ and HAZ was observed in the AR and TA materials. The width of CDZ is slightly narrower for the TA material than the AR material and the grain size shows a larger variation in the CDZ of the AR material.

The microhardness profiles of HV1 and HV0.3 across the FB in the NG AR and NG TA samples are shown in Figure 6. The microhardness peaks are close to the FB in the LAS side in both materials. The HV1 and HV0.3 profiles are rather similar. It is evident that the NG TA material has a higher microhardness peak than the NG AR material and the position of the peak hardness is closer to the FB in the NG TA material.

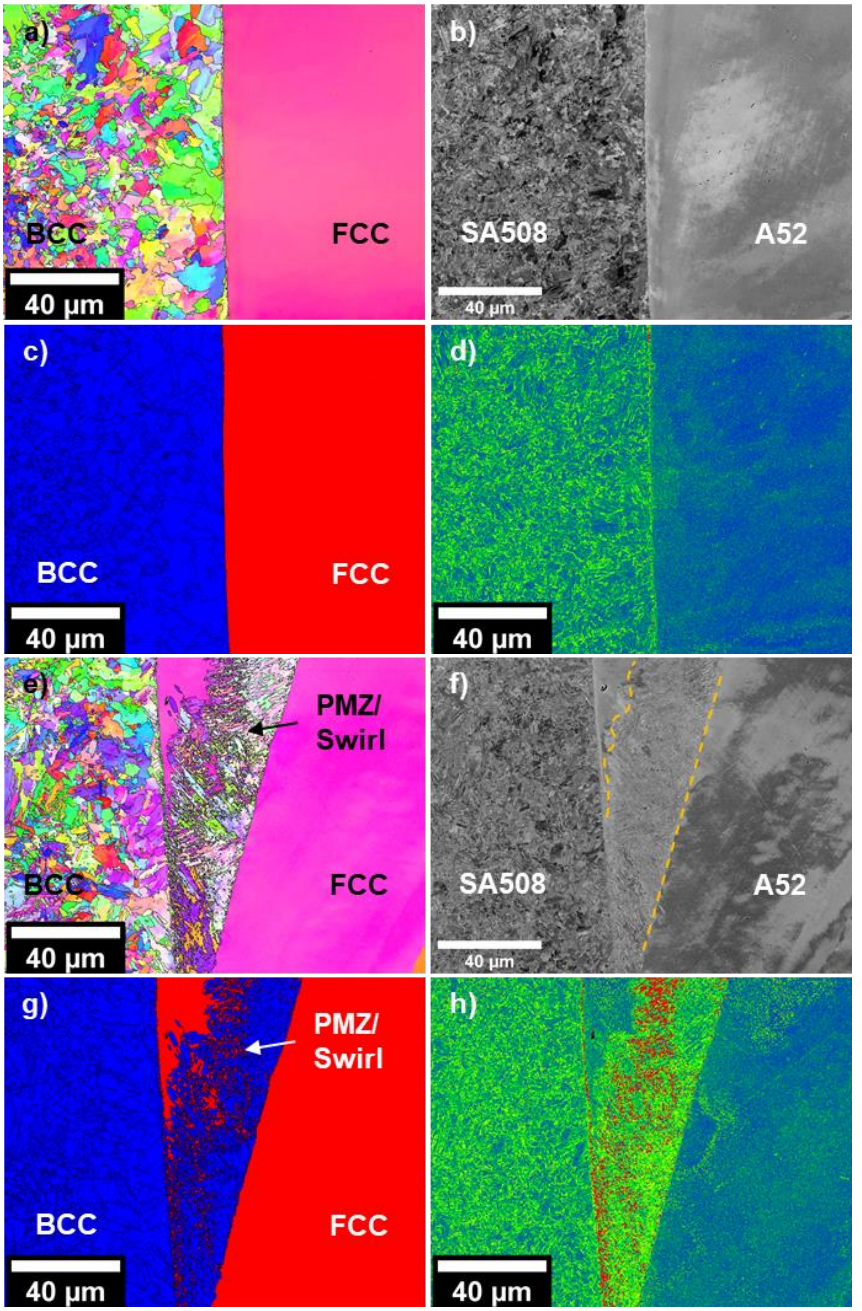

Figure 4: EBSD maps and BSD images for the (a-d) narrow straight FB and (e-h) the PMZ and swirl microstructure of the NG mock-up. The EBSD IPF, BSD, phase map, and KAM-map are shown.

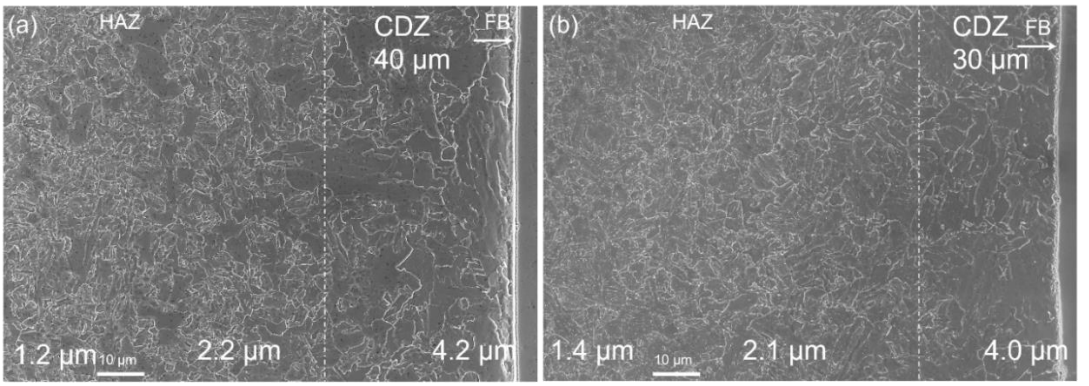

Figure 5: SEM images (using secondary electrons (SEs)) show the grain size distribution and CDZ width in the LAS. (a) NG AR and (b) NG TA.

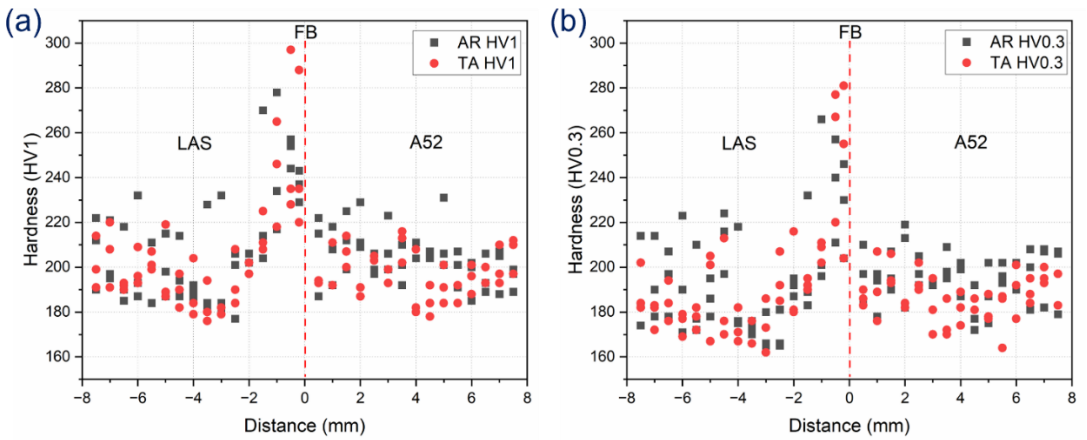

Figure 6: Microhardness profiles of HV1 and HV0.3 across the FB in NG AR and NG TA samples.

3.2.2 CPZ microstructure and carbide analysis

The microstructure and carbide formation at the FB CPZ (0.5–1.5 μm from the FB) were investigated with SEM and TEM. An intensive carbide accumulation area is found in both AR and TA materials due to the high content of strong carbide-forming element of Cr at the FB as shown in Figure 7. Though the width of the CPZ varies locally along the FB, there is a clear difference in CPZ width between AR and TA materials. As shown in Figure 7, the CPZ of AR and TA materials is up to 500 nm and more than 1500 nm, respectively. The number of carbides is much lower and the size of the carbides is also smaller in AR material than in TA material. The elemental maps in Figure 7 reveal that the carbides are (Fe, Cr, Mn) carbides with

Cr content higher than Mn content. In addition, the NG TA material contains Mo-rich carbides and Cr-rich carbides, which are also found at grain boundaries of Alloy 52.

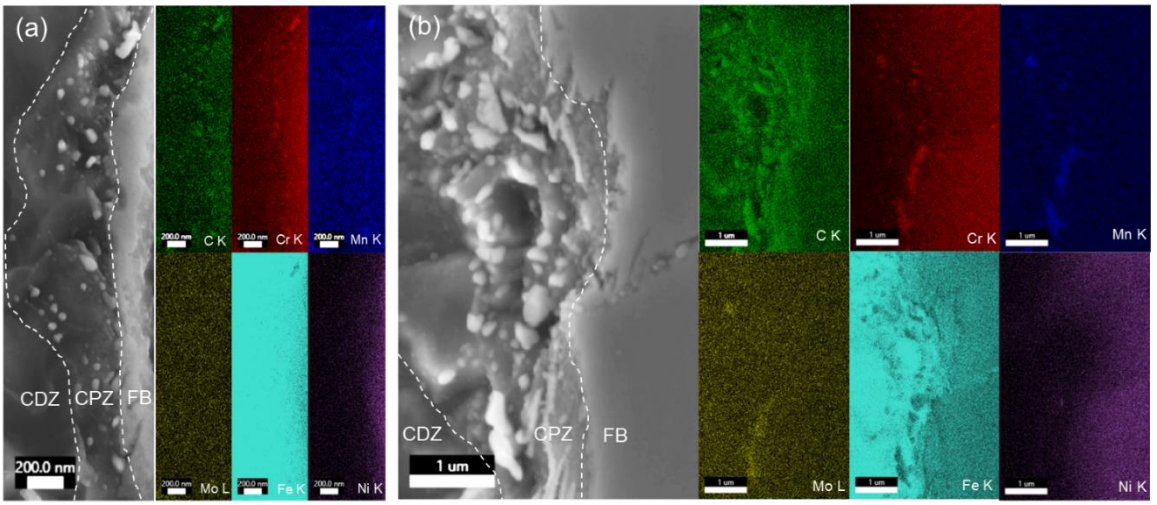

Figure 7: SEM/EDS elemental maps of carbides at the FB of the LAS. (a) NG AR and (b) NG TA.

TEM BF image and elemental maps in Figure 8 reveal the carbides at the FB between LAS and Alloy 52 in the NG AR material. The FB is determined in the image by selected area electron diffraction (SAED) patterns, which show LAS with BCC lattice at the left side and Alloy 52 with FCC lattice at the right side. Near the FB, BCC grains are columnar with a similar orientation. Nanometre-sized Cr nitrides (≤ 30 nm) with both rod shape and round shape were found in the columnar grains next to the FB at the LAS side. The Mo content in these nitrides is also slightly higher than in matrix. Enriched Ni and Mn islands are found inside the BCC phase at the FB. Moreover, the Ni and Mn elements were found to segregate at FBs and boundaries of islands as illustrated in the line profile of Figure 8(d). Except these island areas, the Ni and Cr contents continuously decrease with increasing distance from the FB. In this imaged area only one (Fe, Cr, Mn) carbide of about 40 nm size is found at the lower left corner with Cr content higher than Mn content. It is noted that a quite high dislocation density is observed in both the FCC and BCC phases near the FB. The SAED pattern in Figure 8c is from one (Fe, Cr, Mn) carbide, where weak reflections can be indexed with M3C type carbide along zone axis $[1\bar{1}1]$ and strong reflections from surrounding BCC grains that are close to <111> zone axis.

The FB CPZ microstructure revealed by TEM is in good agreement with the SEM observations in Figure 7. The nanometre-sized Cr nitride accumulated area extends about 100 nm and locally up to 300 nm from the FB. Carbides, rich in Fe, Cr and Mn, dominate in the region about 200–500 nm from the FB together with additional

nanometre-sized nitrides and carbides. Therefore, the CPZ is about 400–500 nm wide between the FB and the CDZ in the NG AR material.

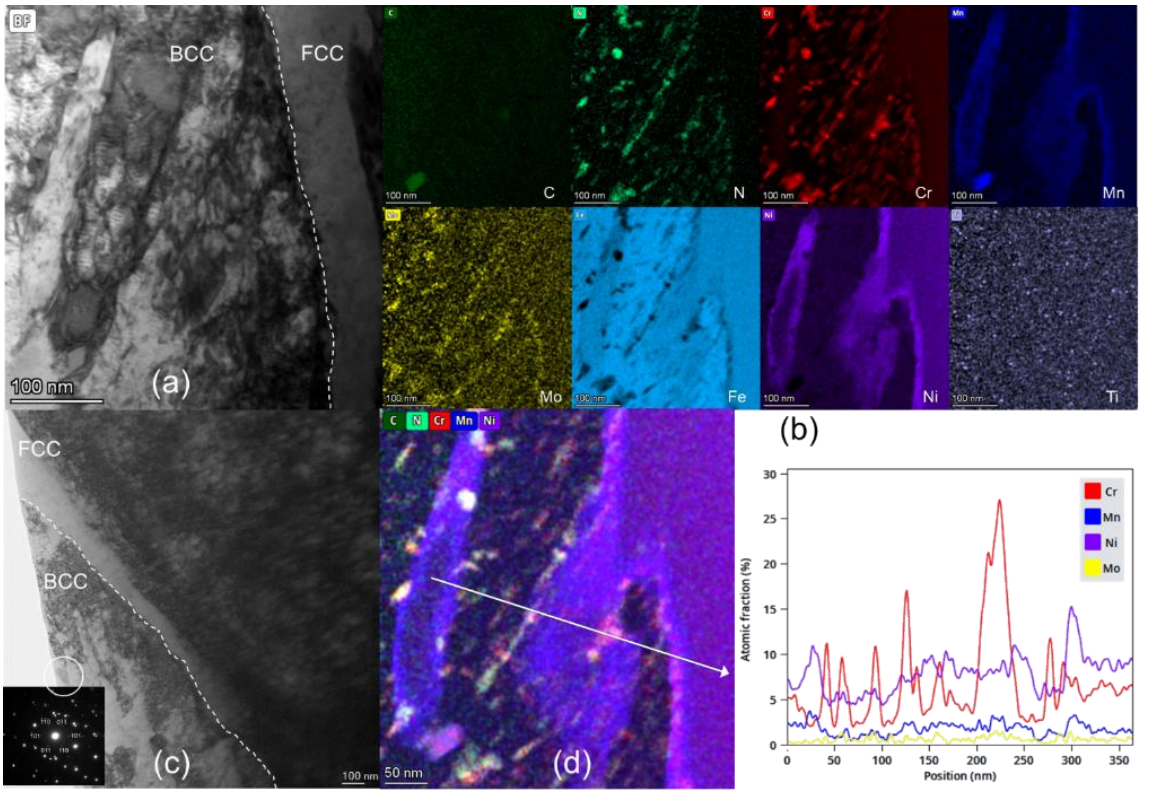

Figure 8: Carbides at the FB in the NG AR material. (a) STEM BF image and (b) the corresponding elemental maps; (c) TEM BF image and SAED pattern of one large carbide of M_3C type along zone axis $[1\bar{1}1]$; (d) Combined carbides and nitrides maps and extracted line profile reveal elemental variation over the FB and nano particles.

The Cr content in the (Fe, Cr, Mn) carbides continues to decrease as the Cr concentration decreases in the matrix with increasing distance from the FB. The microstructure and the carbides at the interface of CPZ and CDZ are shown in Figure 9(b). Except a few nano-nitrides, carbides are almost invisible in the neighbour CDZ grains. The majority of these carbides are relatively large with a size range of 50–100 nm. A SAED pattern with a large selected-area aperture confirms that these carbides are M_3C type of θ phase (*i.e.*, cementite). The Cr concentration is higher than the Mn in almost all carbides next to the FB as seen in Figure 8, whereas the carbides next to the CDZ have a slightly higher Mn content than Cr, see Figure 9. The Cr/Mn ratio of the carbides at the interface between CPZ and

CDZ is normally very close to the Cr/Mn ratio in the surrounding matrix. However, it has been observed that when the Cr/Mn ratio is lower than 1.5 in the matrix, carbides with Cr/Mn ratio below 1 can be formed. This can be seen from the extracted line profile that crosses through a Cr nitride, a high Cr/Mn ratio (>1) carbide and a low Cr/Mn ratio (<1) carbide. Tiny nano-particles about a few nm containing mainly Ti are also visible in this area. The number of Mo-rich carbides along the interface between CPZ and CDZ is notably higher than at the FB.

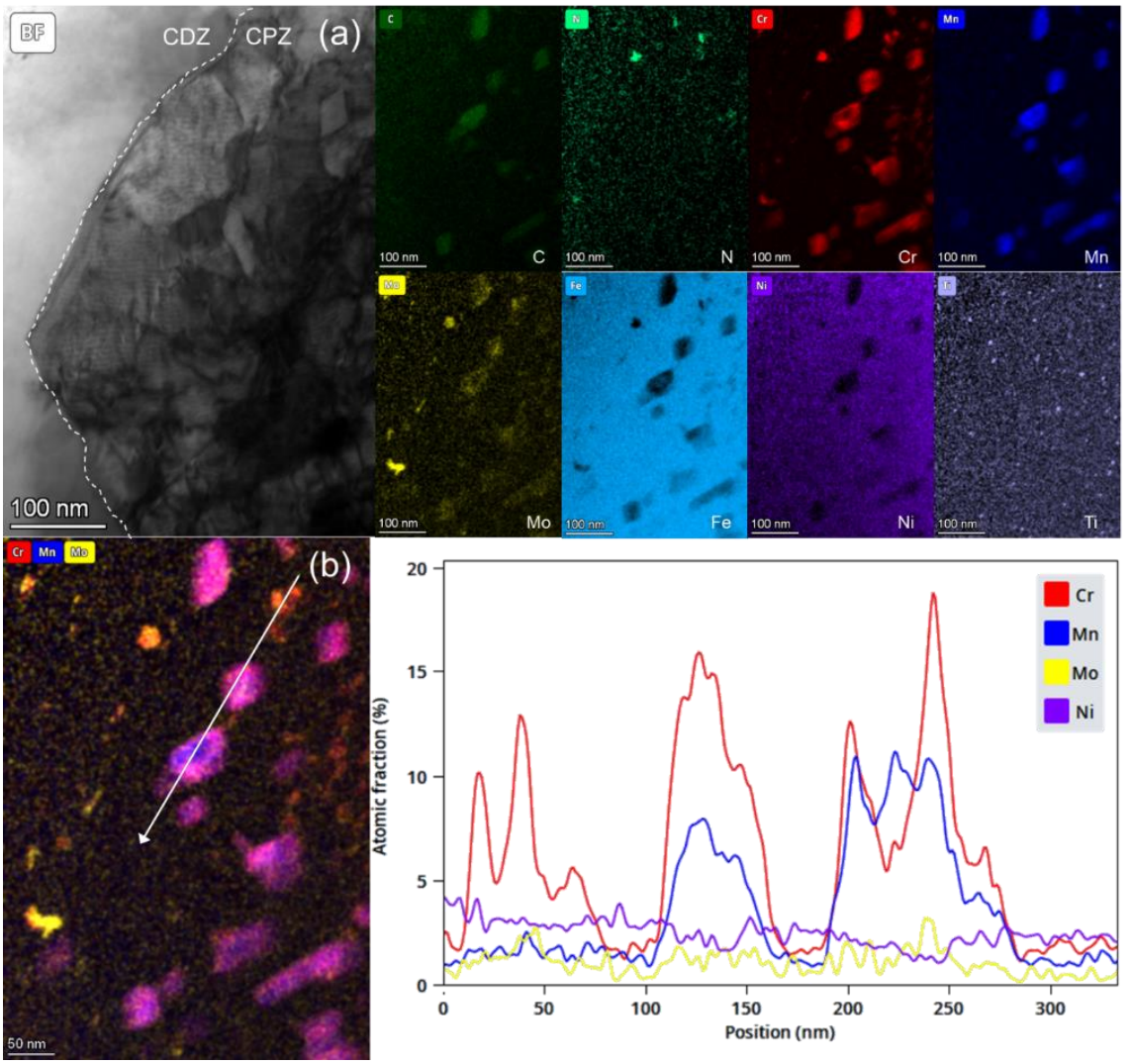

Figure 9: Carbides at the interface of CPZ and CDZ in the NG AR material. (a) STEM BF image and corresponding elemental EDS map; (b) Combined Cr, Mn and Mo maps and extracted elemental profile from the line marked in the colour map.

Nano-particles are also found at the FB in the NG TA material, as shown in Figure 10. In contrast to the NG AR material, these nano-particles are carbides instead of nitrides. As shown in the N elemental map in Figure 10(b), only noisy background counts were detected. Moreover, these carbides belong to Cr-rich and Mn-rich carbides, respectively. The combined maps and line profiles reveal that the compositions are different in these two kinds of carbides. The Mn-rich carbides contain a little Ni whereas the Cr-rich carbides contain a small amount of Mo. Ni and Mn are clearly segregated at the FB. The SAED pattern along [113] zone axis of the BCC phase shows two additional spots located at 1/3 and 2/3 of the BCC reflection $\bar{1}21$. The DF image from 1/3 $\bar{1}21$ confirms that the two extra spots are from nano-carbides. It can be indexed as M_3C θ carbides according to Bargaryatskii's orientation relationship [66] between θ and α, *i.e.* $[001]_\theta \parallel [011]_\alpha$ and $(010)_\theta \parallel (2\bar{1}1)_\alpha$. According to this orientation relationship, for BCC [113] zone axis, the M_3C is close to [102] zone axis with a 3.4° deviation, resulting in only one systematic row along 010* direction under this diffraction condition. In other words, in this particular orientation, $[102]_\theta$ is about 3.4° away from $[113]_\alpha$ and $(060)_\theta \parallel (\bar{1}21)_\alpha$. Similar to the NG AR material, Ti-rich nano-particles with about a few nm size are visible in both BCC and FCC phases. The density of nanometre-sized carbides decreases gradually with increasing distance from the FB. The area containing accumulated nanometre-sized carbides extends more than 1 µm from the FB in the NG TA material, which is much longer than in the NG AR material.

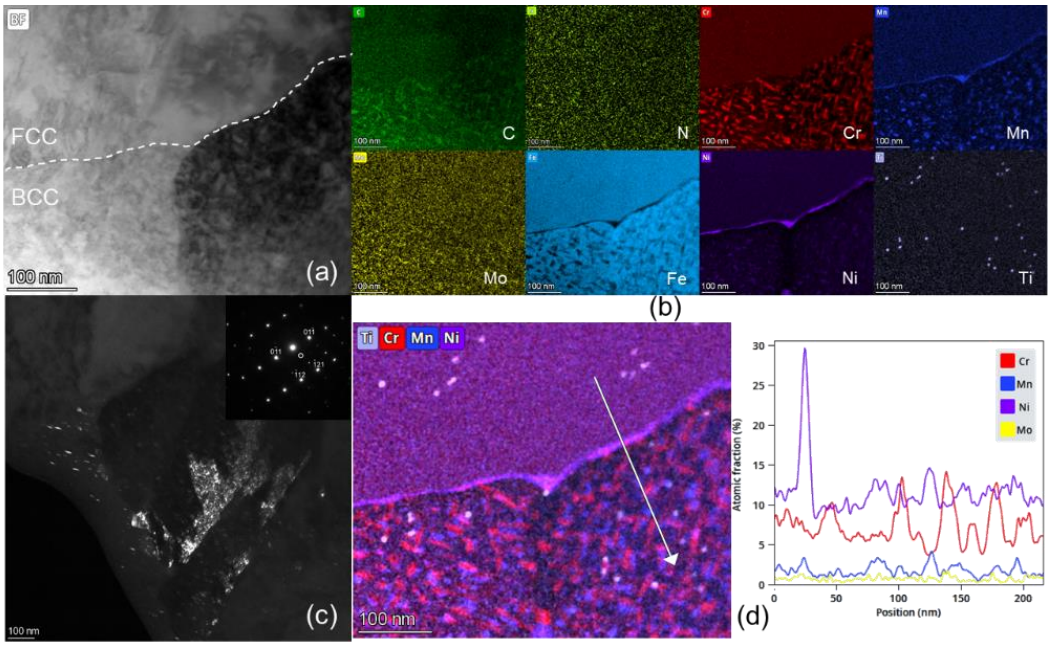

Figure 10: Nano-carbides at the FB in the NG TA material. (a) STEM-BF image and (b) the corresponding elemental map; (c) TEM DF with nano-carbides' reflection from SAED pattern along zone axis [113]; (d) The colour-mixed elemental map and extracted profile with line position indicated in the map.

The CPZ normally extends to around 1.5 µm from the FB. However, when the tempered martensite type of FB was formed instead of a narrow FB (as in most cases), the CPZ can be as wide as about 11 µm, as revealed by Figure 11. At the interface of CPZ and CDZ (next to the tempered martensite type of FB), the number of carbides significantly decreased and almost disappear in the neighbour CDZ grains, as shown in Figure 12. Tempered martensite laths with high dislocation density are aligned approximately parallel to the interface in Figure 12. The tempered martensite laths are full of carbides with Cr content higher than Mn. The dominated carbides in CPZ are (Fe, Cr, Mn) carbides of M_3C type. However, at the interface of CPZ and CDZ, the Mn content in the carbides becomes higher than the Cr content and the Cr/Mn ratio in matrix is about 1.5. The nitrides are not found at the interface of CPZ and CDZ. However, the N map illustrates that the nanometre-sized nitrides formed together with carbides at lath boundaries in CPZ. Ni-rich particles are also observed in carbides especially at lath boundaries. It is noted that Mo carbides start to form at the interface between CPZ and CDZ.

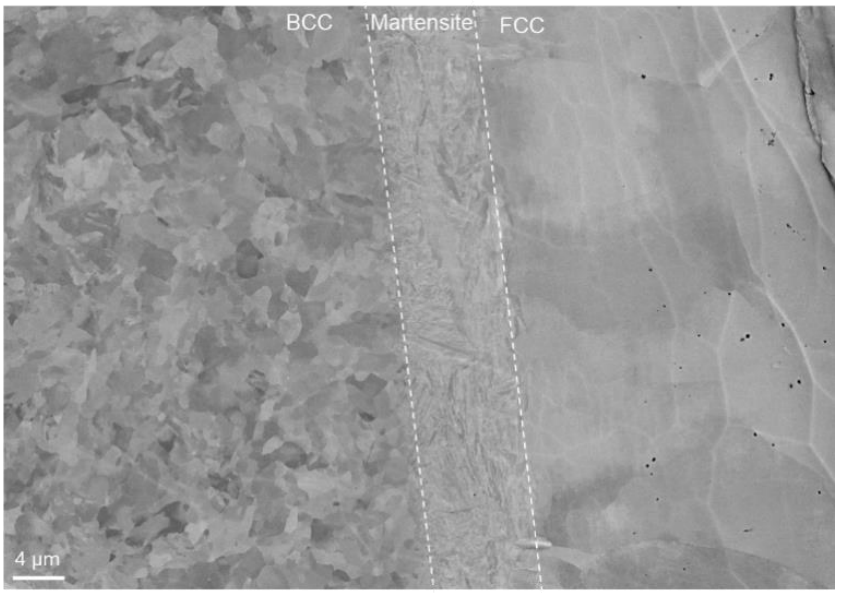

Figure 11: The NG TA material contains a martensite area between FCC (right) phase and BCC phase with a width about 11 µm.

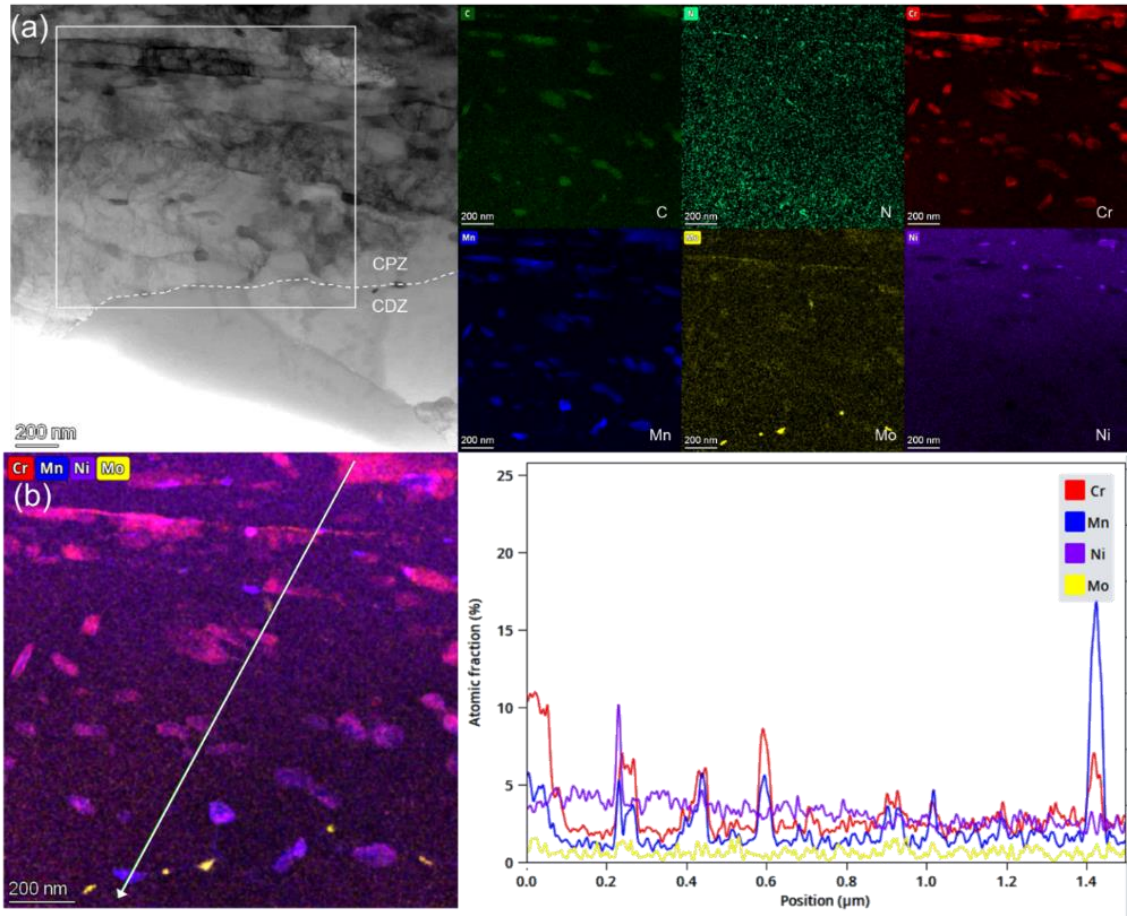

Figure 12 : Carbides at the interface of CPZ and CDZ in NG TA material. (a) STEM BF image and corresponding elemental map of framed area in BF image. (b) Combined Cr, Mn, Ni and Mo maps and extracted profile for the line indicated in colour-mixed image.

3.2.3 CDZ microstructure and carbide analysis

Figure 5 and Figure 7 show that in the CDZ no apparent carbides are visible in SEM images. Due to the limited resolution of SEM, it only indicates that no carbides with size larger than 100 nm are present. TEM examination of the CDZ area reveals that there are carbides in the CDZ but with much lower density and smaller size compared with carbides near the FB. In contrast to the difference in width of CDZ, the carbide distribution in the CDZ in NG AR and NG TA materials is quite similar, as shown in Figure 13 and Figure 14, respectively. In Figure 13(b) and Figure 14(b), the observed carbides are mostly Mo carbides with few (Fe, Mn, Cr) carbides

located at grain boundaries. It is worth noting that (Fe, Cr, Mn) carbides dominate in the CPZ where the Cr content is higher than Mn. However, for the (Fe, Mn, Cr) carbides in CDZ, the Mn content is much higher than Cr. The line profile of the carbides shows that the Cr content in carbides is just slightly higher than in matrix. The size of (Fe, Mn, Cr) carbides in CDZ are normally ≤50 nm and the size of Mo carbides is mostly only a few nanometres.

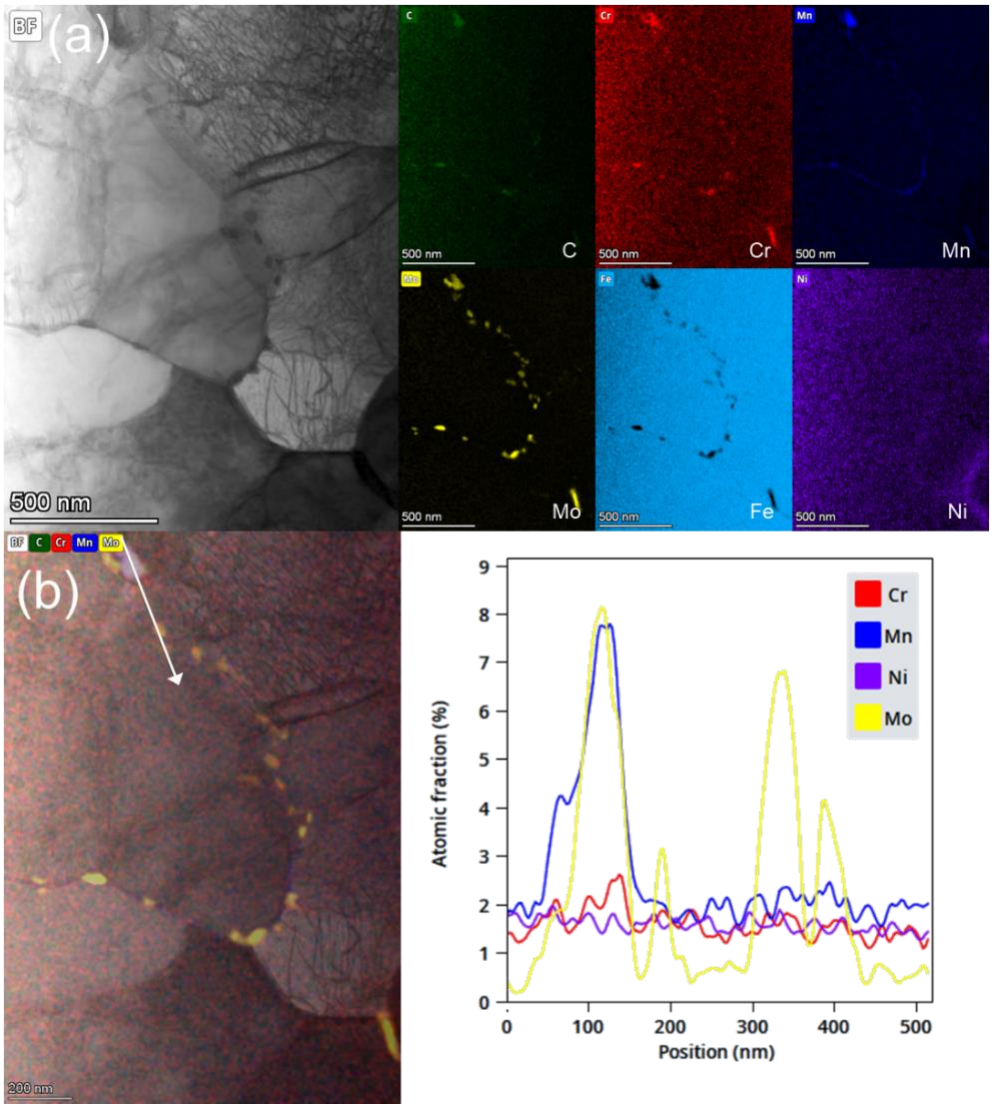

Figure 13: Carbides in CDZ in NG AR material. (a) STEM BF image and corresponding elemental maps; (b) Mixed of BF image and C, Cr, Mn, and Mo elemental maps and the extracted profile from line marked in the mixed image.

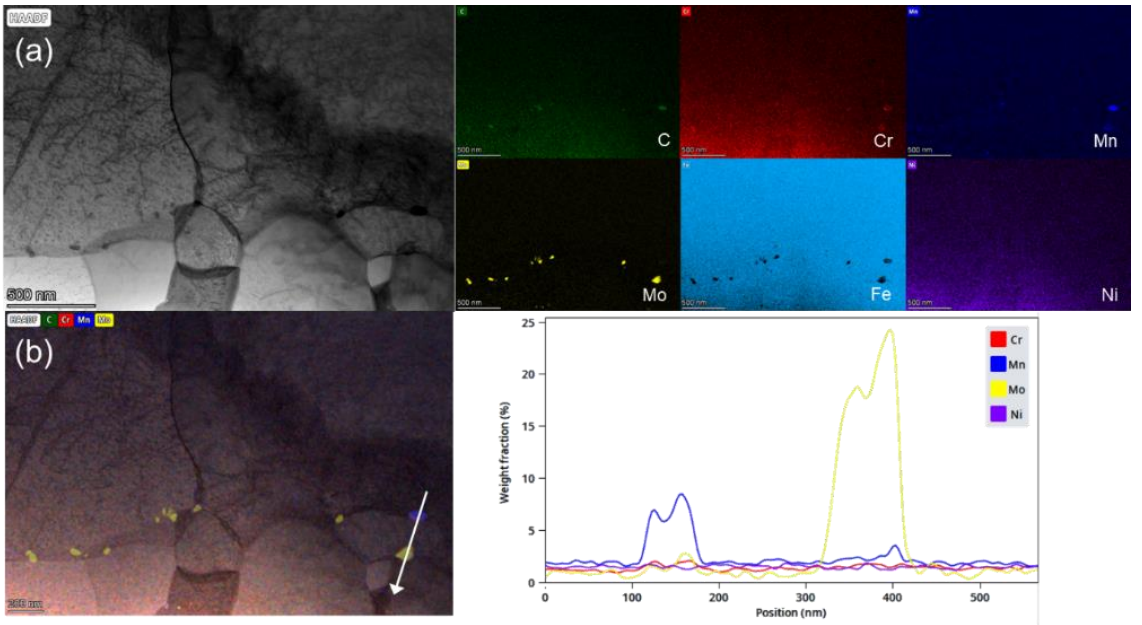

Figure 14: Carbides in the CDZ of the NG TA material. (a) STEM BF image and corresponding elemental maps; (b) Mix of BF image and C, Cr, Mn, and Mo elemental maps and the line profile from the arrow line in the mixed image.

3.2.4 HAZ microstructure and carbide analysis

From CDZ to HAZ, the carbide population increases dramatically. The microstructure and carbide distribution in the HAZ of the NG AR and the NG TA materials are illustrated in Figure 15. SEM images show two kinds of grains, grains with excess carbides and grains lacking apparent carbides. High-resolution TEM reveals that these grains lacking apparent carbides may contain nano-sized carbides. It is worth to note that the fraction of grains devoid of visible carbides in the HAZ is higher in the NG TA material than in the NG AR material. The STEM image of Figure 15(d) shows a few long fibre-like carbides aligning in same direction, with the longest one up to 2 µm. It seems like that these long carbides were formed during thermal aging.

The TEM-EDS elemental maps in Figure 16 illustrate the morphology and distribution of carbides in the HAZ of the NG AR material, where excess carbides can be found both at grain boundaries and within grains. There are two size groups of carbides, *i.e.*, relatively small carbides and relatively large carbides in the HAZ. The dominant and large-size carbides range from tens to hundreds of nanometres. They have a round or ellipsoidal shape and are found both at grain boundaries and within grains. The elemental maps and the extracted line profile in Figure 16 reveal that the large carbides are (Fe, Mn, Cr) carbides with the content of Mn being much higher than the Cr content. Only occasionally, carbides with Cr content higher than

Mn are observed (few carbides containing high-Cr core particles). The relatively small carbides are Mo-rich carbides. The majority of the Mo carbides are located at grain boundaries and their size is about a few tens of nm. Figure 16 reveals additionally Al-Si nano-sized particles with a few nm to a few tens nm in size. The SAED in Figure 16(b) consists of two phases, the major reflections from BCC along [102] zone axis and the weak spots from Mo_2C along [100] zone axis. A few Mo_2C particles are illustrated in the DF image with Mo_2C $00\overline{2}$ reflection.

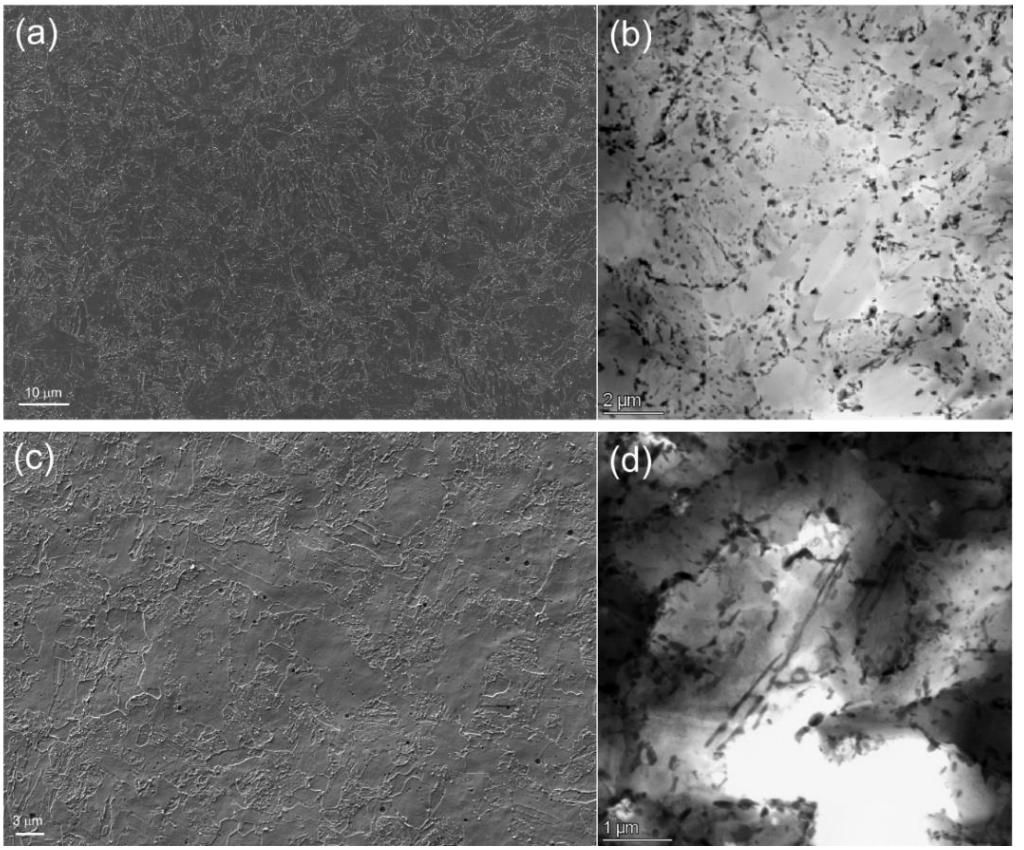

Figure 15: Microstructure and carbide distribution in the HAZ of (a-b) NG AR and (c-d) TA material. (a,c) SEM SE images and (b,d) STEM BF images.

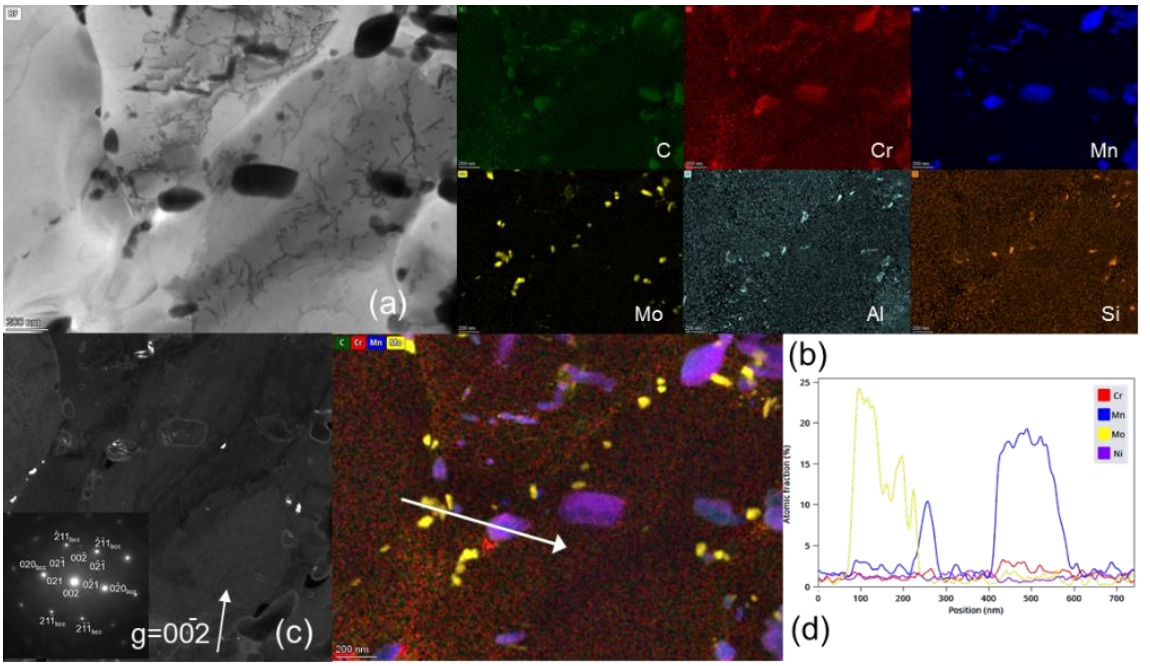

Figure 16: Carbides in HAZ of NG AR material. (a-b) STEM-BF image and selected elemental maps; (c) TEM DF image from Mo_2C's reflection $00\bar{2}$ with the inset SAED pattern indexed with BCC zone axis [102] and Mo_2C zone axis [100]; (d) Mix of selected elemental maps and extracted line profile.

To investigate the crystal structure of (Fe, Mn, Cr) carbides in the NG AR material, one large and isolated particle was tilted along the zone axis $[1\bar{1}0]$, which confirmed M_3C crystal structure in Figure 17. The DF image from the reflection of $\bar{1}\bar{1}1$ reveals a low angle boundary in the particle. The lattice parameters deviated slightly from the lattice of stoichiometric Fe_3C.

The chemical composition of long fibre-like carbides with length up to 2 µm in the HAZ of the NG TA material is presented in TEM EDS mapping in Figure 18. They are (Fe, Mn, Cr) carbides with Cr content slightly higher than in the matrix. The extracted line profile shows that the width of these carbides is between 50 and 100 nm. Most of the Mo carbides are a few tens of nm in size but a few of them are needle-like and extend over 100 nm. Such long Mo carbides are not observed in the NG AR material.

SAED patterns from two separated carbides in the HAZ of the NG TA sample examined with different zone axes are presented in Figure 19(a,b). Both zone axis patterns can be indexed with M3C lattice and the lattice parameters agrees perfectly with stoichiometric Fe_3C. Figure 19(c) illustrates a high-resolution fringe image of one Mo carbide and its fast Fourier transform (FFT), which can be indexed with Mo_2C crystal of orthorhombic lattice along [110] zone axis.

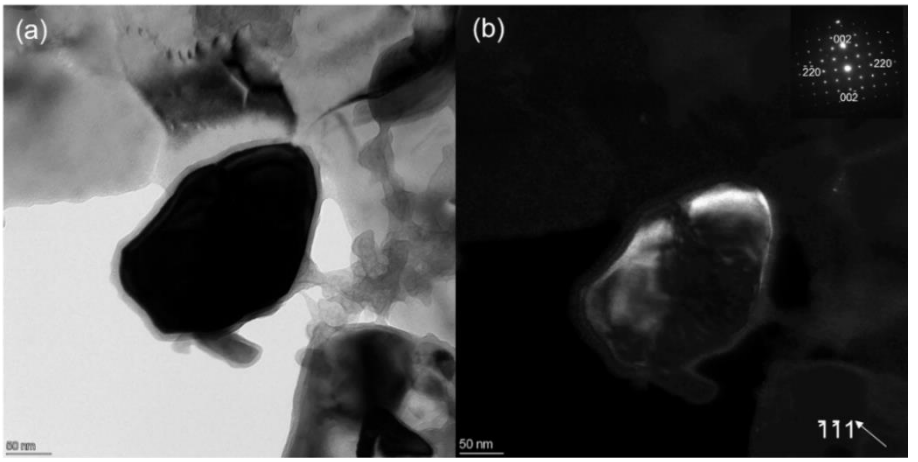

Figure 17: TEM BF image (a) and DF image (b) along [1$\bar{1}$0] zone axis in the HAZ of the NG AR sample with the inset being SAED pattern.

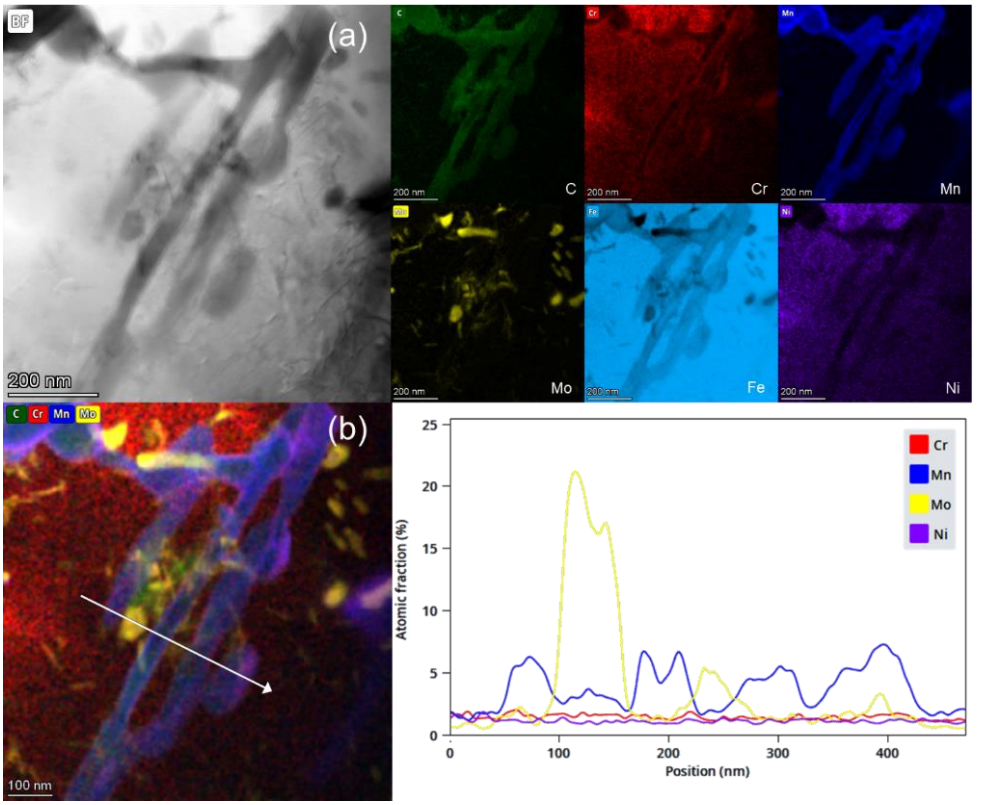

Figure 18: Carbides in the HAZ of the NG TA material. (a) STEM-BF image of carbide and corresponding selected elemental maps; (b) combined elemental map and extracted line profile from line position indicated in the image.

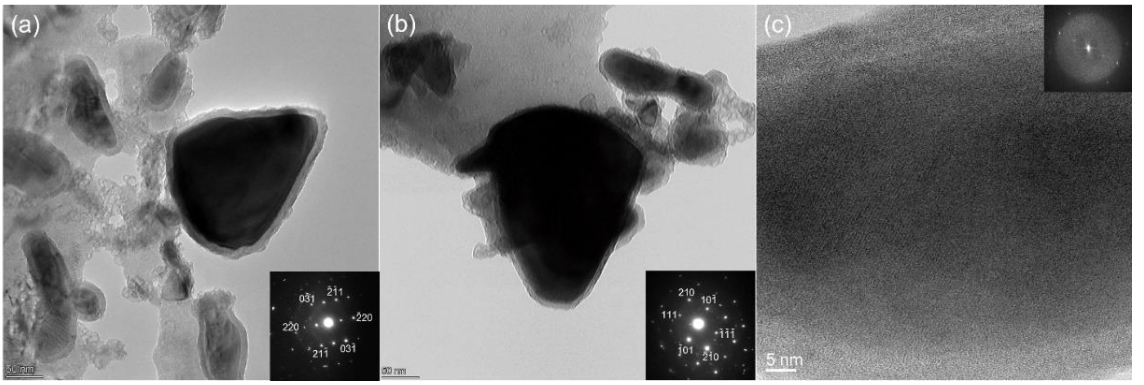

Figure 19: TEM image of Fe carbides and Mo carbides in the HAZ of the NG TA sample. (a) TEM BF image of Fe carbide along [113] zone axis; (b) TEM BF image of Fe carbides along [$1\bar{2}1$]; (c) HRTEM of a Mo carbide with the inset of its FFT which fits to zone axis [110].

3.2.5 WAXS of carbides in HAZ

The Rietveld refinement results of WAXS patterns are presented in Figure 20. The X-ray diffraction pattern confirms the two types of carbides observed in TEM, *i.e.,* M_3C and Mo_2C. The AR and TA patterns are quite similar in general and contains approximately 2% carbides. However, the TA pattern shows slightly higher volume fraction of carbides than the AR pattern. After thermal aging the ratio of M_3C carbides increased in the NG TA material compared to the NG AR material. In TEM observation of the TA material, there is a higher amount of Mo_2C carbides than in the AR, material but WAXS refinement has shown slightly higher Mo_2C fraction in the AR material. The controversy results are mainly because the nano-sized Mo_2C has weak broaden peaks and its fraction is at the detection limit of WAXS.

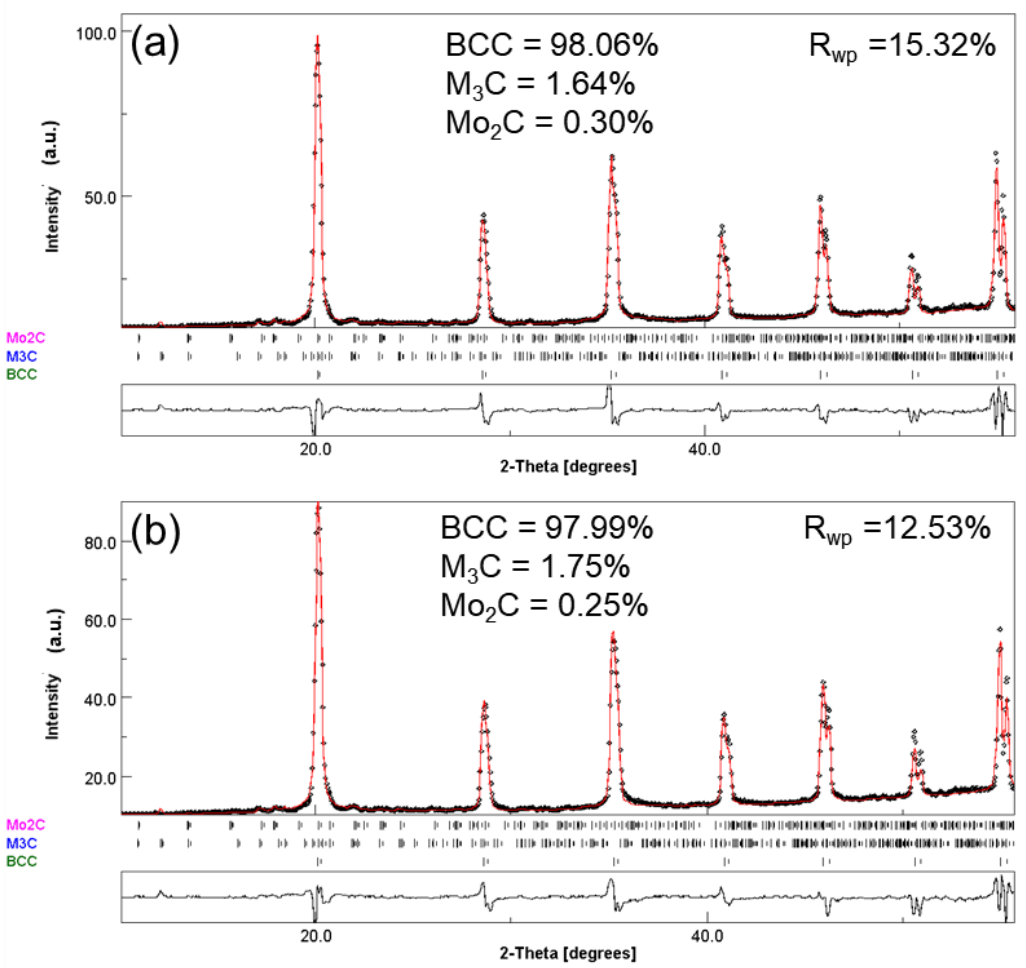

Figure 20: WAXS patterns of (a) NG AR material and (b) NG TA material.

3.2.6 APT analysis

Effect of thermal aging on the potential P segregation in the LAS HAZ was studied with APT. Comparing the P content on grain boundaries using APT is a challenging task, as the APT data is very local. Analysing a specific grain boundary is not enough, as different types of grain boundaries often contain different amounts of segregation [67]. Thus, a full characterisation of the type of grain boundary (including EBSD and transmission Kikuchi diffraction) would be needed, and a number of grain boundaries need to be analysed in order to get a statistically significant result. This approach is thus very time consuming and work intense. In this paper, another path was chosen. This was to compare the average amount of

the element concentration in the interior of the HAZ grains from multiple APT samples. If the segregation after thermal ageing is strong enough, the bulk P content in the interior of the grains would be lower in the NG TA material than in the NG AR material.

The APT analyses of the HAZ bulk of AR and TA materials contained no grain boundaries. The average bulk compositions measured from multiple APT analyses can be seen in Table 5. The P contents are low, 50±20 appm and 40±20 appm in the AR and TA materials, respectively. With these compositions, there is no evidence of a significant P segregation to grain boundaries from thermal ageing.

Table 5. Compositions of the interior of the grains in HAZ of the NG AR and TA materials from APT. The error given is the standard deviation between the APT runs used, indicating small local differences in the composition, resolved by APT.

	TVO AR at.%	TVO TA at.%
Fe	Bal.	Bal.
Mn	1.08±0.24	1.11±0.44
Ni	0.79±0.04	0.76±0.02
Si	0.42±0.02	0.42±0.01
Mo	0.22±0.04	0.19±0.10
Cr	0.23±0.08	0.22±0.04
Cu	0.035±0.003	0.034±0.005
N	0.03±0.04	0.05±0.01
Co	0.02±0.01	0.01±0.01
C	0.16±0.18	0.04±0.04
Al	0.005±0.003	0.020±0.019
P	0.005±0.002	0.004±0.002
V	0.002±0.001	0.002±0.002

In Figure 21, representative reconstructions of AR and TA materials are shown. In these analyses, occasional dislocation lines are present. These can be observed by APT due to the enrichment of Mo, Mn and C. Statistically, there is a small tendency for P to segregate to these dislocation lines. However, no difference in P segregation to dislocation lines between the NG AR and TA materials could be proven by the APT measurements.

In the NG AR material, part of a carbide was analysed by APT. The carbide contains mainly Fe (59 at.%) and Mn (14 at.%) as metallic elements. Mo and Cr were also enriched in the carbide (both by less than 2 at.% each). The C content was measured to be 24 at.% but might be slightly underestimated due to cascades

of C atoms evaporating simultaneously during APT analysis and detector deadtime [68]. In connection to this carbide, a low-angle boundary enriched in C and P is observed. This shows that there is probably a certain level of P segregation on boundaries before long-term thermal ageing. The bulk P content is around 90 at.ppm (50 wt.ppm), so the APT measurements suggest that about half of the P is segregated already before aging.

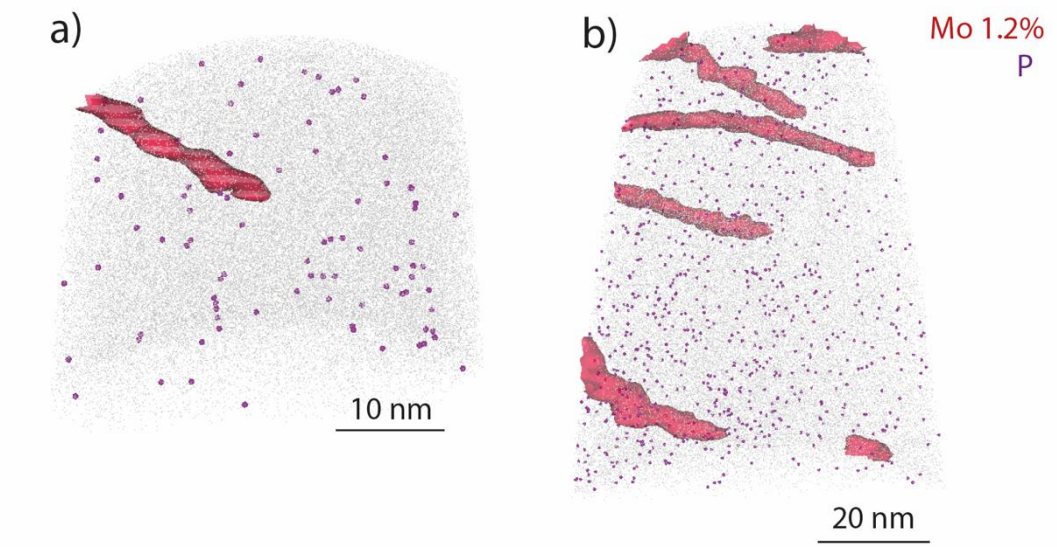

Figure 21. APT reconstructions of (a) NG AR and (b) NG TA materials. Purple dots correspond to P atoms, and red surfaces to 1.2% Mo (iso-concentration surfaces), delineating Mo enrichment at dislocations. Grey shows the extent of the analyses.

3.3 Microstructural characterization of Ringhals mock-up

The Ringhals mock-up is a SA508/Alloy 52 DMW mock-up consisting of Alloy 52 buttering on both sides. This mock-up was studied in as-received condition (*i.e.* PWHT). The microstructure, crystal structure, elemental diffusion and macro-, micro- and nano-hardness of the SA508/nickel-base Alloy 52 buttering FB interface were investigated [69].

3.3.1 Macro-, micro- and nano-hardness measurements

A representative DMW cross-sectional specimen was prepared with EDM and polished to 0.25 µm finish for the macro- and micro-hardness measurements. After the hardness measurement, the specimen was etched to reveal the microstructure and indent locations in the DMW (Figure 22). The Vickers macro- and micro-hardness measurements with loads of 10 kg (HV10), 1 kg (HV1) and 0.3 kg (HV0.3) across the FB were performed, using Struers DuraScan-80 hardness measurement device. The indentation spacing of HV10 was 0.75 mm in the HAZ and region close to the FB, and 2 mm in the other regions. The indentation spacing of HV1 and HV0.3 was kept at 0.5 mm. As shown in Figure 22, the HV10 was measured with four lines indicated as L1, L2, L3 and L4. The L1 is the nearest to the outer surface and the L2 the nearest to the inner surface with the cladding. The L3 is in the middle of the wall thickness and the L4 below the cladding HAZ characterizing the near inner surface hardness across the SA508/Alloy 52 FB. The HV1 and HV0.3 were measured across the FB in the middle of the wall thickness adjacent to the HV10 L3 measurement line.

The macrostructure of the full DMW is shown in Figure 22, where the LAS, cladding, butterings and V-groove welds are indicated. The hardness measurements reveal different microstructural features across the FB from weld to HAZ, the LAS matrix and stainless-steel cladding. The macro-hardness measurements (HV10) are plotted in Figure 23(a) with four lines L1-L4, as indicated in Figure 22(a). The nearest hardness line to the inner surface is the L2, revealing the hardness profile across the FB of SS cladding/Alloy 52, with only a mild increase of hardness adjacent to the FB. The macro-hardness across the FB of SA508/Alloy 52 buttering is measured by L1, L3 and L4, of which the hardness peak locates in the HAZ adjacent to the FB on the SA508 side with hardness of ~280 HV10. Beyond ~2.5 mm from the FB in the SA508 side, the macro-hardness is relatively uniform at an average of ~210 HV10. On the weld side, the macro-hardness values drop until 1–2 mm from the FB. The macro-hardness in the buttering weld showed a similar HV10 level compared to the SA508 side but with a higher scatter resulting from the buttering weld beads microstructure. A significant difference is seen in the weld side between the lines L1 and L2-L4, as the hardness curve near the outer surface shows almost opposite trend of macro-hardness compared to the hardness in the mid-thickness or near the inner surface. The deviation in the hardness curves in the weld indicate internal strains in the V-groove root (L2) and buttering root (L1).

The micro-hardness profiles of HV1 and HV0.3 are plotted in Figure 23(b). The micro-hardness indents are located in the middle of the wall thickness across the FB as indicated in Figure 22(b). The curves reveal micro-hardness peaks (320 HV1/HV0.3) in the HAZ region at ~1 mm from the FB. Further from the FB, the micro-hardness is relatively stable (~220 HV1/HV0.3) for both SA508 and Alloy 52. According to the micro-hardness measurements, the SA508 HAZ has a width of approximately 2 mm.

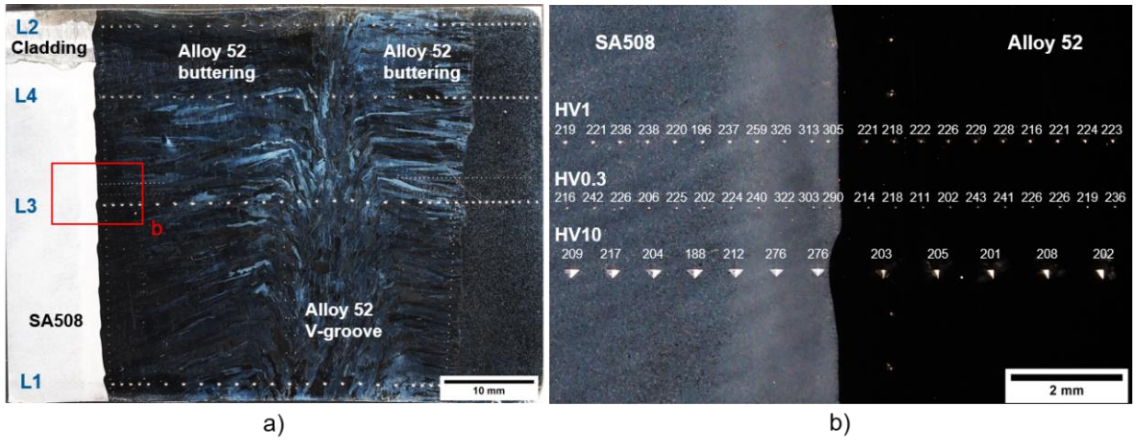

Figure 22: (a) Macrostructure of the etched DMW and HV10 macro-hardness measurement lines L1-L4. (b) The micro-hardness measurement lines HV1 and HV0.3 in the middle of the wall thickness of DMW (next to the HV10 L3 line).

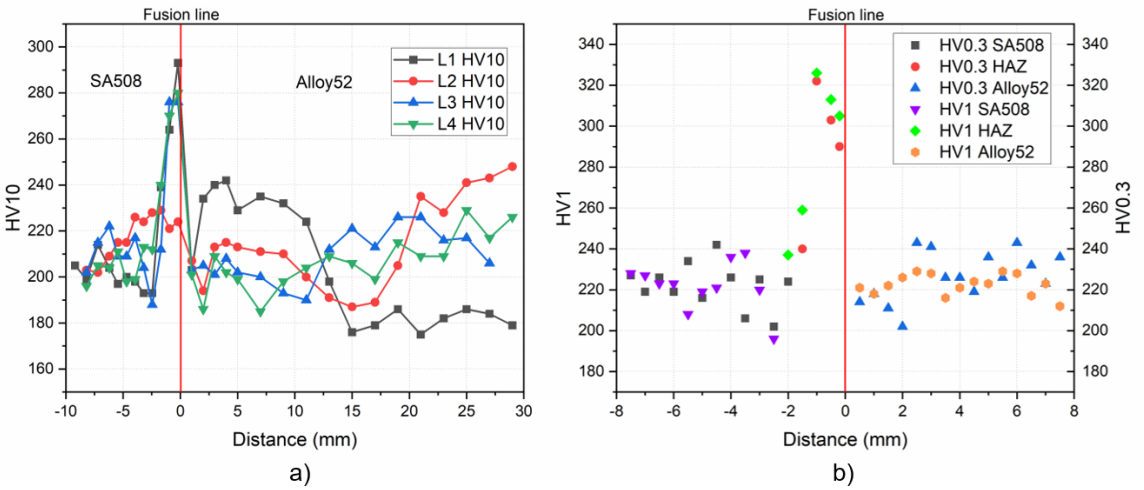

Figure 23: (a) Macro-hardness HV10 results across the FB from the measurement lines L1-L4. (b) Micro-hardness HV1 and HV0.3 results across the FB.

The microstructure across the FB of SA508/Alloy 52 buttering and its adjacent regions on both sides, *i.e.*, HAZ and weld was investigated with the etched metallographic specimen. Figure 24(a) shows the ghost lines as dark lines throughout the bainitic SA508 material. According to the macro- and micro-hardness measurements, the macro-segregation is mild as the ghost lines do not cause significant macroscale deviation in the hardness values. The visible width of the HAZ is ~2.3 mm, which is in line with the hardness measurement results. With a different etching solution, the weld microstructure with the weld beads in the buttering orientation is shown in Figure 24(b). The austenitic Ni-grains grow across weld beads in transverse direction with dendritic substructure. The grains are decorated with darker vertical micro-segregation areas at the intersection of the weld beads. The weld beads in two welding directions are indicated and the junction between the welds has mixed due to remelting. The A52 grains appear to grow in the direction of subsequent weld passes in both welds. In Figure 24(c-e), the FB and CDZ are indicated. Three different types of FBs were identified; narrow straight FB without a distinctive microstructure (Figure 24(c)), PMZ (Figure 24(d)), and tempered martensitic transition zone (Figure 24(e)). The tempered martensitic phase was confirmed by TEM. The FB type also seems to have an effect on the extent of the CDZ, as with narrow FB and PMZ the CDZ is slightly wider than with the tempered martensitic FB.

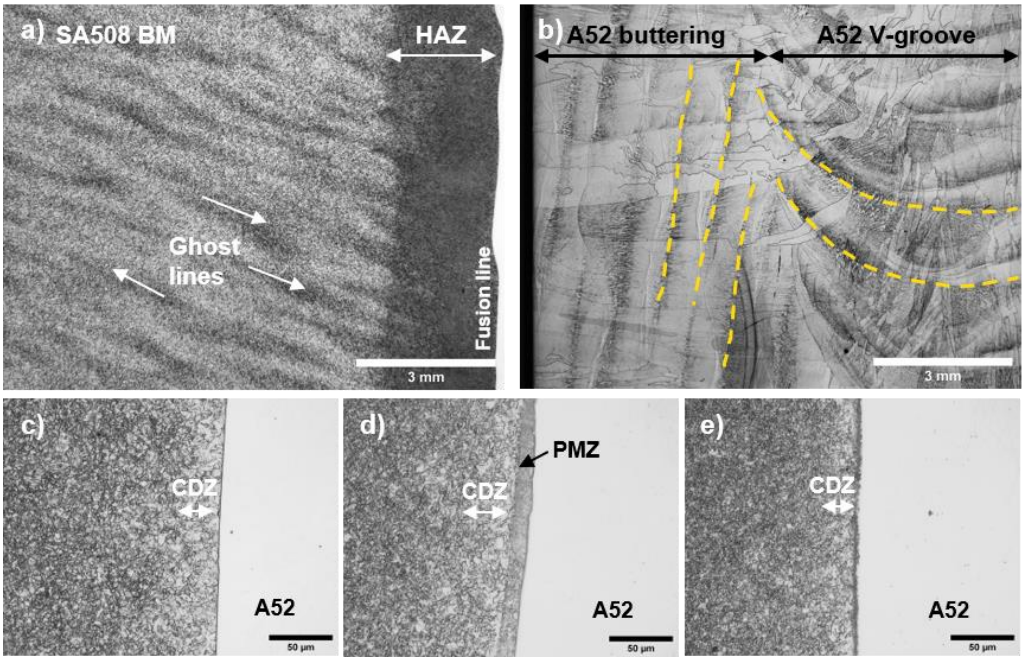

Figure 24: Metallographic microstructure of the mock-up DMW with buttering weld, where (a) LAS-side is etched, (b) A52 is etched showing weld beads in the buttering and V-groove. The CDZ and different types of microstructures found at the FB are (c) narrow FB, (d) PMZ, and (e) tempered martensite FB.

3.3.2 Fusion boundary characterization

The microstructure of the SA508/Alloy 52 buttering FB was investigated using LOM (with SA508 side being etched) and SEM-BSE. Three different types of FB microstructures were identified, *i.e.*, i) narrow FB, ii) tempered martensitic transition region and iii) wide PMZ, as shown in Figure 25.

In total ~18 mm of FB of the SEM specimen was assessed, where the majority of the FB is narrow without a distinctive visible microstructure (Figure 25(a-b)), defined here as type-A, occupying ~80–85% of the FB. The type-A boundary area is typically narrow (<1 µm wide), where the microstructure changes from BCC to FCC without a distinctive transition zone. Second most common boundary type observed is the feathery-like tempered martensitic transition microstructure with up to ~8 µm in width (Figure 25(c-d)), defined as type-B, occupying up to ~15% of the FB. In the optical imaging, the type-B FB appears as a dark region with fine lath-like acicular microstructure. Due to the lath-like microstructure at the FB, the weld side interface is not very distinct and exact. The third FB microstructure type is the wide PMZ (Figure 25(e-f)) with up to ~25 µm in width, being the least common and is found only at a few locations. It is defined as type-C, occupying only ~1–2% of the FB. The type-C FB region is light in colour under LOM and there is a distinct and well-defined boundary for the transition zone which is different to the type-B FB. Observed in Figure 25, the three types of FBs appear to associate with different levels of grain coarsening and CDZ widths in the LAS HAZ, indicating a difference in the local heat flow and elemental diffusion between the FB types. The CDZ and grain size evolution adjacent to the FB is shown in Figure 26. The carbon depletion appears as empty ferrite grains in the coarse-grained region with grain size still relatively small of ~4 µm. The CDZ width is approximately ~30 µm at the location of a type-A FB. Beyond the CDZ, the grain size decreases towards ~1 µm size and the carbide content increases.

Type-B and type-C FBs as specific features at the FBs represent local changes in properties and are suspected to be more critical for integrity of DMWs and thus are the focus of this investigation. The Type-B and type-C FB microstructures were further investigated using SEM-BSE imaging, EBSD, EDS, nanoindentation and XRD analysis.

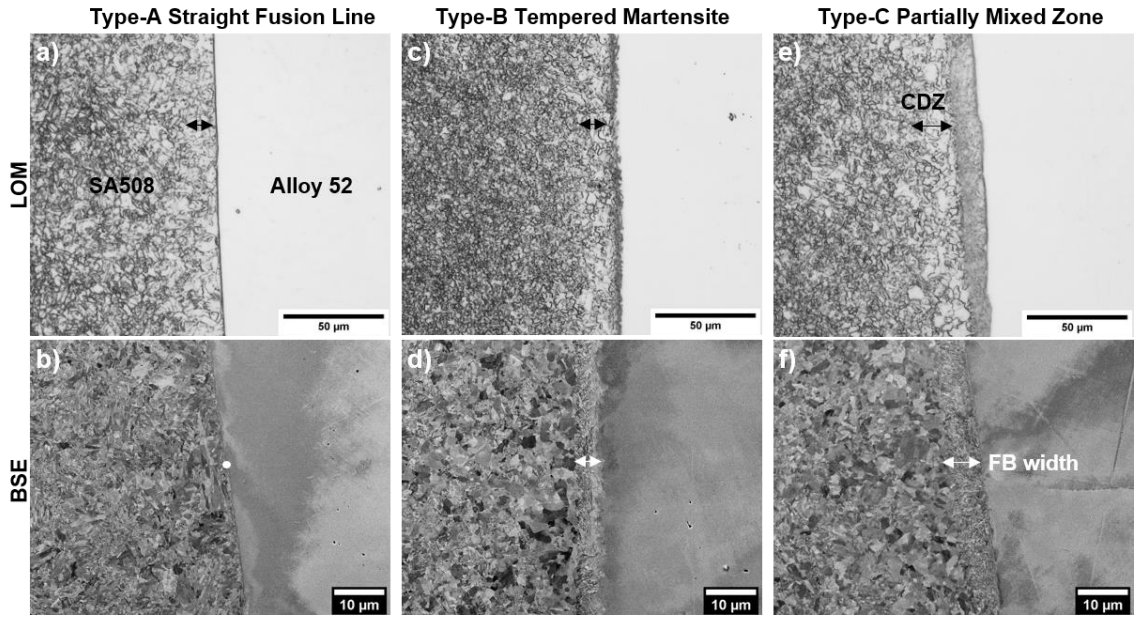

Figure 25: Three types of FB microstructures (a-b) type-A straight FB, (c-d) type-B tempered martensite and (e-f) type-C PMZ. CDZ and FB widths were marked in (a, c, e) optical microscopy images and (b, d, f) SEM-BSE images, respectively.

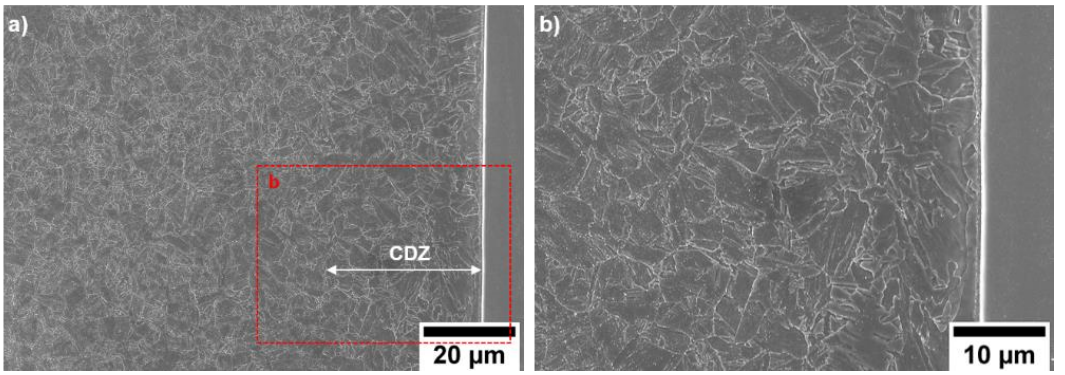

Figure 26: (a) HAZ and (b) CDZ at a type-A FB. The grain size is ~4µm adjacent to the FB with carbon depletion. From ~30 µm from the FB beyond the CDZ, the grain size decreases closer to ~1µm.

SEM-BSE, EBSD and EDS were applied to analyse the nano-indented regions on types B and C FB microstructures. The BSE images in Figure 27(a-c) and Figure 28(a-c) reveal the microstructures of the type-B and the type-C boundaries, respectively. The corresponding EBSD maps including IPF map and phase map with high-angle grain boundaries (15°–62.7°) and KAM analysis are shown in Figure

27(d-f) and Figure 28(d-f). The type-B boundary of 8 µm width is featured with lath-like acicular grain microstructure. The lath with length of 2–8 µm and diameter of 200–600 nm grows towards the weld buttering in heat flow direction presumably starting from the favourably oriented fine grains at the bainitic HAZ. The interface between type-B FB and the Alloy 52 buttering WM is characterized by a wavy feathery-like boundary. The type-B FB is dominant by the BCC phase in the phase map and the feathery-like structure is associated with tempered martensitic microstructure. The type-C PMZ FB in Figure 28 has a straight FB to the Alloy 52 buttering WM but with a ~25-µm-wide distinct region of mixed phases of BCC and FCC in the transition region.

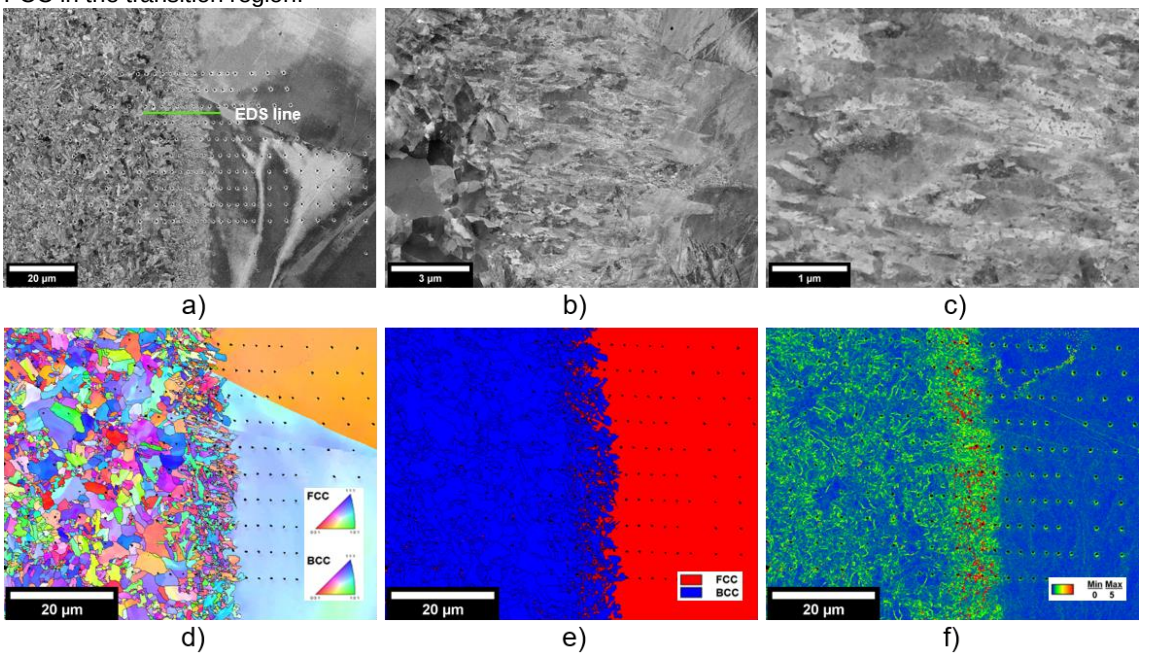

Figure 27: FB investigation on type-B tempered martensite. (a-c) SEM-BSE, (d) IPF, (e) phase map and (f) KAM mapping. EBSD mapping step size is 0.10 µm.

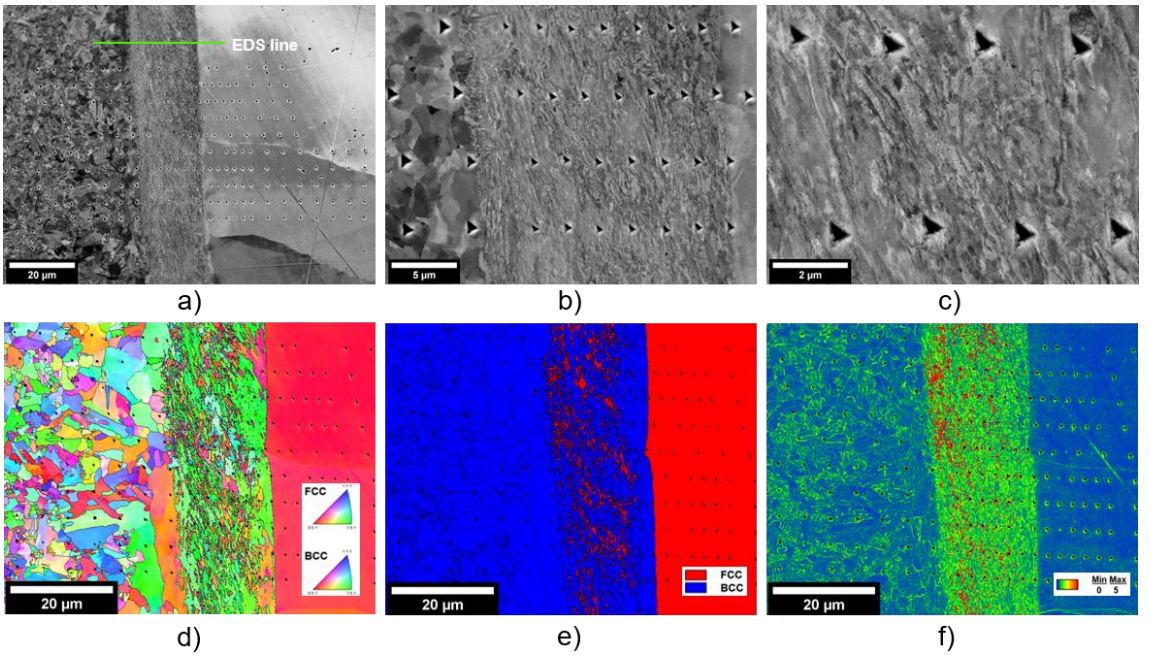

Figure 28: FB investigation on type-C PMZ. (a-c) SEM-BSE, (d) IPF, (e) phase map and (f) KAM mapping. EBSD mapping step size is 0.03 µm.

Semi-quantitative chemical composition analysis with EDS line scan was performed across the type-B and the type-C FBs. The location of the line scans are marked in the Figure 27(a) and Figure 28(a) for the type-B and the type-C FBs, respectively. The EDS results are shown in Figure 29, where the major alloy elements of iron (Fe), Ni, Cr and manganese (Mn) are plotted. Increasing Fe content and decreasing Ni and Cr contents were found closer to the FB, forming a dilution zone from the buttering WM side to the FB. The change in the chemical composition across the type-B tempered martensite FB is almost linear for the concentrations of Fe and Ni with a gradual change in the profile, which are the main constituents of SA508 and Alloy 52, respectively. In contrast, there is a drastic change of alloying elements concentrations from SA508 to PMZ and from PMZ to Alloy 52 with sharp changes in the profile across the type-C FB. The chemical composition of alloying elements is nearly constant within the type-C PMZ with ~75 wt% of Fe, ~15 wt% of Ni and ~5 wt% of Cr.

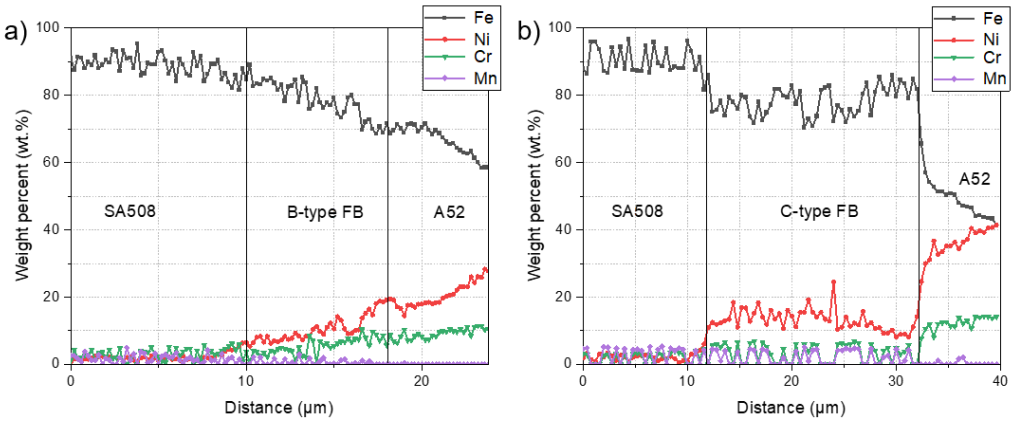

Figure 29: EDS line scans across the FBs of (a) type-B tempered martensite and (b) type-C PMZ.

Nanoindentation mappings were performed to reveal the influence of FB types B and C on the nano-hardness mismatch across the local DMW interfaces, as shown in Figure 30. The mapping in Figure 6(a) and (c) reveals visually the change in the properties across the two different FBs. The nanoindentation data shows that there is an evident peak in the nano-hardness at the type-B FB area. The hardness level in the LAS side adjacent to the FB does not reveal significant softening due to carbon depletion. In the type-C, only a mild nano-hardness peak was measured for the PMZ FB which appears higher due to the contrast to the lower hardness level of the LAS side region adjacent to the FB. This ~30 μm region with low nano-hardness in the LAS is the CDZ and the overall hardness level for the type-C appears lower with less scatter in Figure 30(d) compared to the type-B FB in Figure 30(b). Contradictorily, ~10 μm low bound nano-hardness region on the Alloy 52 buttering side was observed in the type-B FB in Figure 30(b) but not in the type-C FB in Figure 30(d).

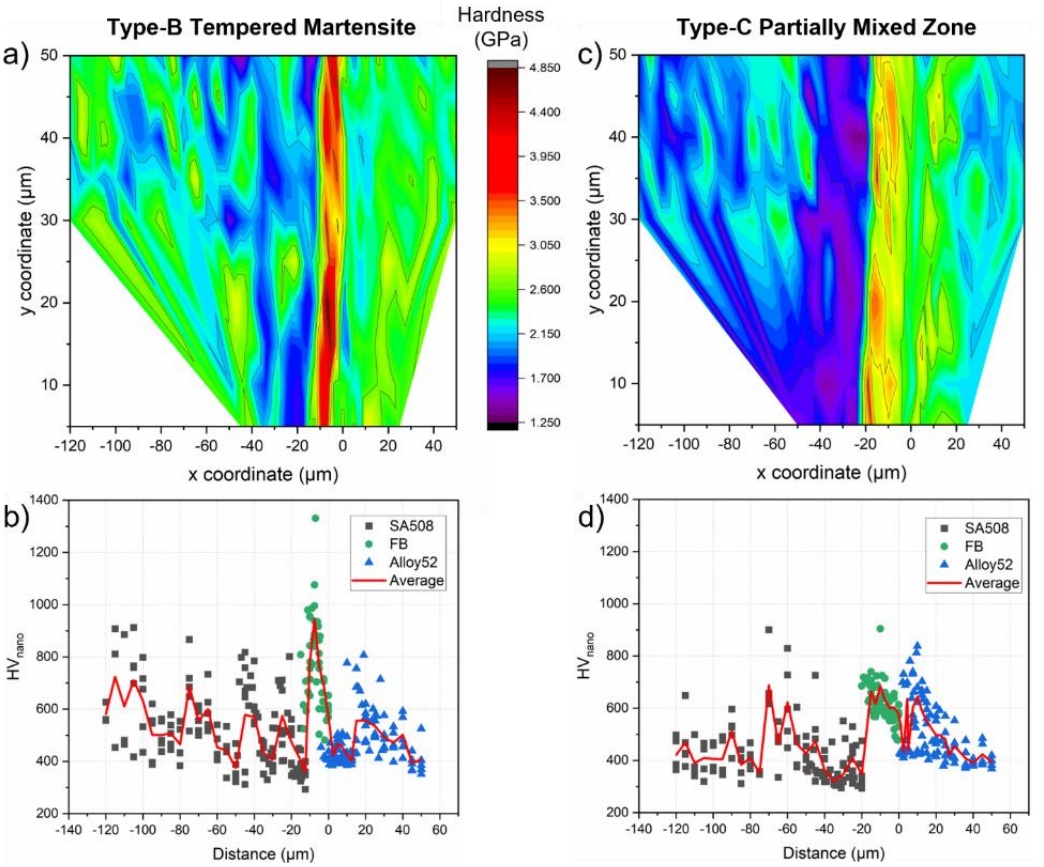

Figure 30: Nanoindentation results for the (a-b) type-B tempered martensite and (c-d) type-C PMZ FBs. The type-B tempered martensite FB exhibits a nano-hardness peak in the FB.

3.3.3 Carbide analysis

A qualitative carbide investigation was first performed at different distances for the type-B and type-C interfaces in the LAS HAZ and in the Alloy 52 weld, using SEM-BSD imaging. The analysis close to the type-B FB in Figure 31(a) shows tempered martensitic microstructure with relatively high density of intragranular carbides. At a distance of ~35 µm from the FB in the LAS side (Figure 31(b)), the density of carbides is significantly decreased in the CDZ and in the HAZ at further distance over the CDZ the amount of C increases where the carbides are both intra- and intergranular. On the weld side, as seen in Figure 31(c), with a distance of ~40 µm from the FB, only a few carbides are present in the grain boundary. However, with a distance of 100 µm from the FB (Figure 31(d)), relatively large cluster of intergranular carbides are observed at a weld grain boundary junction.

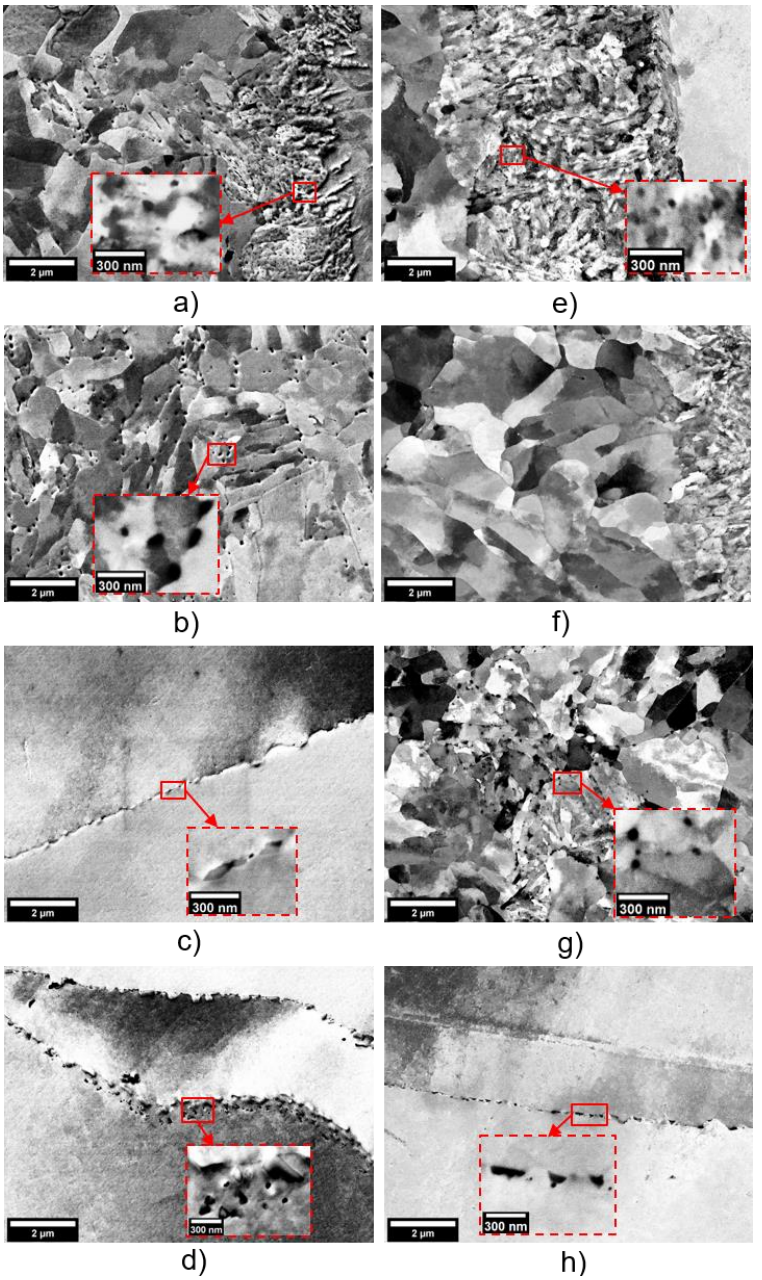

Figure 31: Carbide evolution across the (a-d) type-B and (e-h) type-C FBs. Analysis from locations in the LAS HAZ with distances of (a) 6 µm (close to FB) and (b) 36 µm (in CDZ) from the type-B FB, and (e) at the PMZ FB, (f) at 8 µm (in CDZ), and (g) at 48 µm (in HAZ) from the type-C FB. Analysis from locations in the Alloy 52 weld with distances of (c) 40 µm and (d) 100 µm from the type-B FB and (h) at 13 µm from the type-C FB.

At a type-C PMZ FB in Figure 31(e), the density and size (~50 nm) of carbides observed are relatively similar to those of the tempered martensitic FB. The CDZ shown in Figure 31(f) is wider than that of type-B FB. The CDZ transition to HAZ of a type-C interface is seen in Figure 31(g) at a distance of ~48 µm from the FB. The distribution of carbides is more clustered with regions of depletion, whereas in the Figure 31(b) CDZ transition of a type-B interface the distribution of carbides is more even but at lower density. On the weld side, at a 13 µm distance from the PMZ FB, intergranular carbides of ~300 nm long lamellas shown in Figure 31(h) are revealed. In a type-I boundary resulting from the epitaxial growth of the grains in the FB region adjacent to the FB, the carbide density is higher near the FB compared to a typical weld grain boundary.

The carbides formation at the different zones in LAS side of SA508/Alloy 52 FB were further investigated in detail with SEM, TEM and X-ray techniques. An intensive carbide accumulation area is found next to FB due to the high content of strong carbide-forming element of Cr as shown in Figure 32. The width of carbides precipitation area for buttering AR sample is up to 230 nm. The elemental maps in Figure 32 reveal that the carbides are Fe-Cr carbides in the buttering AR mock-up. There is an abrupt change of Ni content over FB in a buttering AR sample.

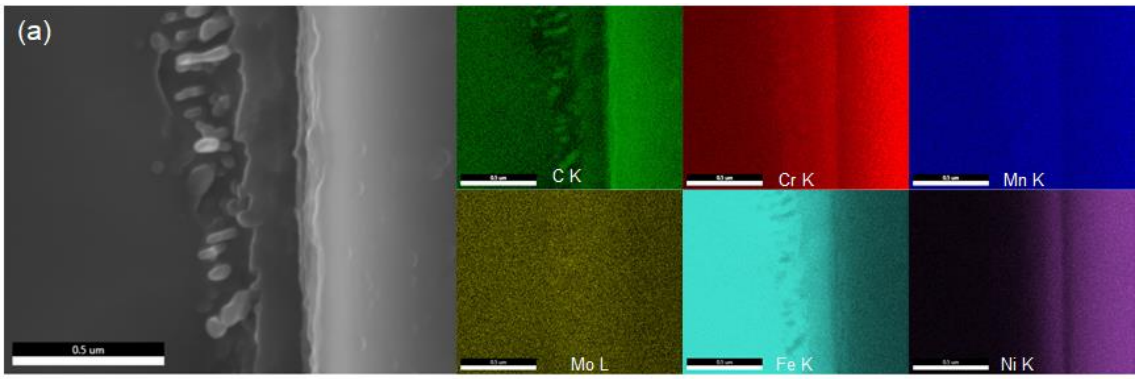

Figure 32: SEM elemental maps of carbides at FB in the Ringhals AR sample.

From CDZ to HAZ, carbides population increases dramatically. The carbides distribution and grain structure are presented in Figure 33 for the buttering AR mock-up. The majority of grains are with excess carbides but there are grains lacking visible carbides with the resolution limitation of SEM as in Figure 33(b). The volume fraction of grains lacking visible carbides is small. With high-resolution TEM, it reveals that these grains contain nano sized carbides.

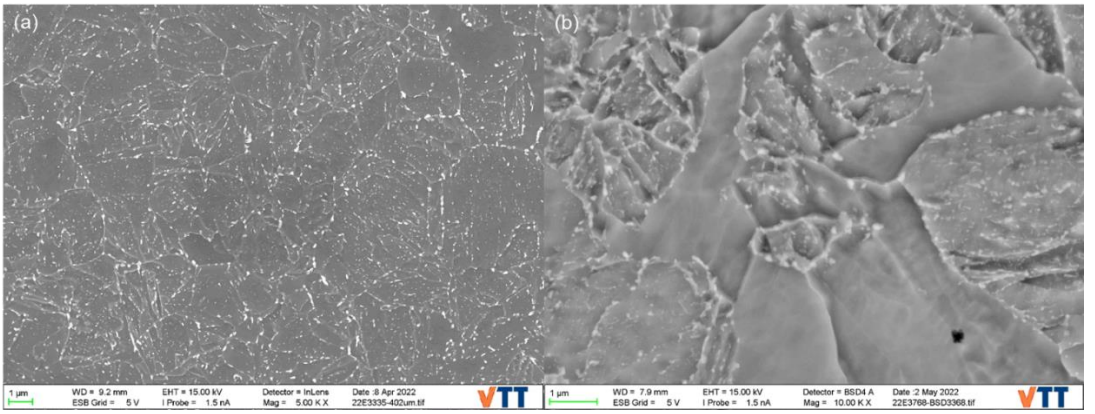

Figure 33: Microstructure of the HAZ in the buttering AR sample. (a) SEM SE image of grain structure and carbides distribution. (b) SEM BSE image shows grains with excess carbides and grains devoid of visible carbides.

Two types of carbides were revealed in the LAS BCC phase, showed in STEM images and elemental maps in Figure 34. The dominant carbides are Fe- and Mn-rich with a small amount of Cr, having round shape and a size ranging from a few nm to over 100 nm. They were found both at grain boundaries and within grains. Another type of carbide found is Fe- and Mo-rich carbides, most of which are small in size from a few nm to a few tens of nm. Similar to the (Fe, Mn, Cr) carbides, they can be both inter- and intragranular. In the (Fe, Mn, Cr) carbides the Cr content is much lower than the Mn content, but in the Mo-riched carbide, the content of Mn and Cr are almost the same. The normalized at% profile of C, Cr, Mn and Mo is illustrated in Figure 34 for comparison of the relative contents in these two types of carbides.

There are two size groups of carbides, *i.e.*, relatively small carbides and relatively large carbides in the HAZs of the mock-up. The dominant and large carbides range from tens to hundreds of nanometres in size. They have round shape and are found both at grain boundaries and within grains. The elemental map and line profiles reveal that the large carbides are (Fe, Mn, Cr) carbides with the content of Mn relatively higher than the Cr content. Occasionally, Fe carbides with a Cr content higher than Mn are observed, such as shown in Figure 35 in the buttering AR mock-up. The majority of Fe carbides has a higher Mn content than Cr, but a few of them contain high-Cr core particles. The average size of the Mo carbides is much smaller than that of the Fe carbides. Their size difference is well demonstrated from extracted line profile which across a few Fe and Mo carbides in Figure 35(b).

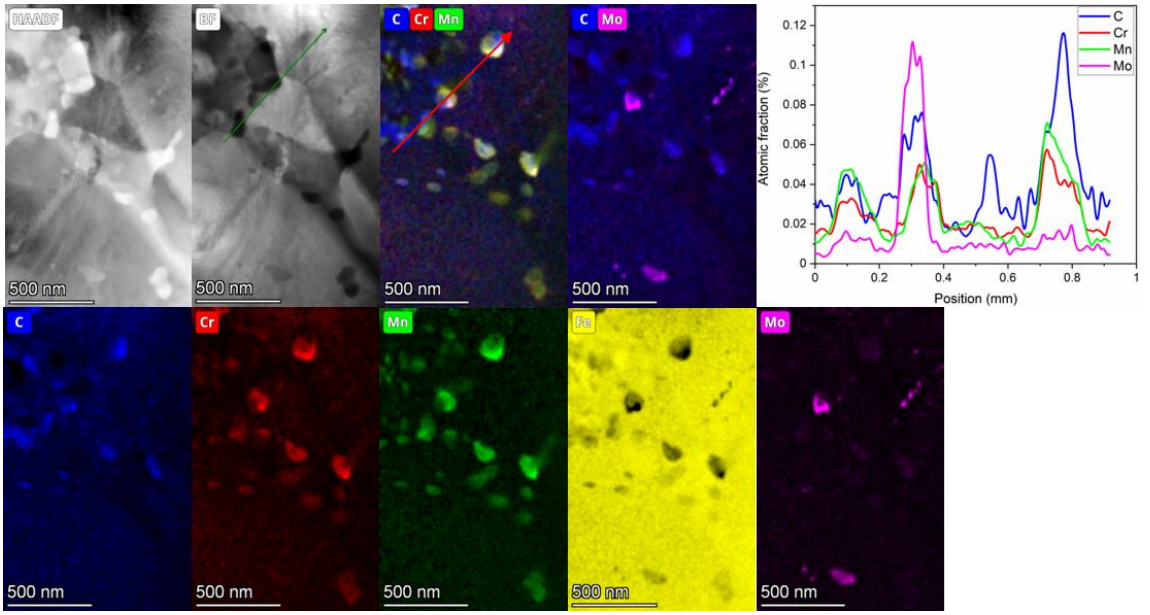

Figure 34: STEM images (HAADF and BF) and elemental maps of carbides in SA508 at ~83 µm distance from the FB. The peaks represent the elemental evolution along the arrow marked in C-Cr-Mn map.

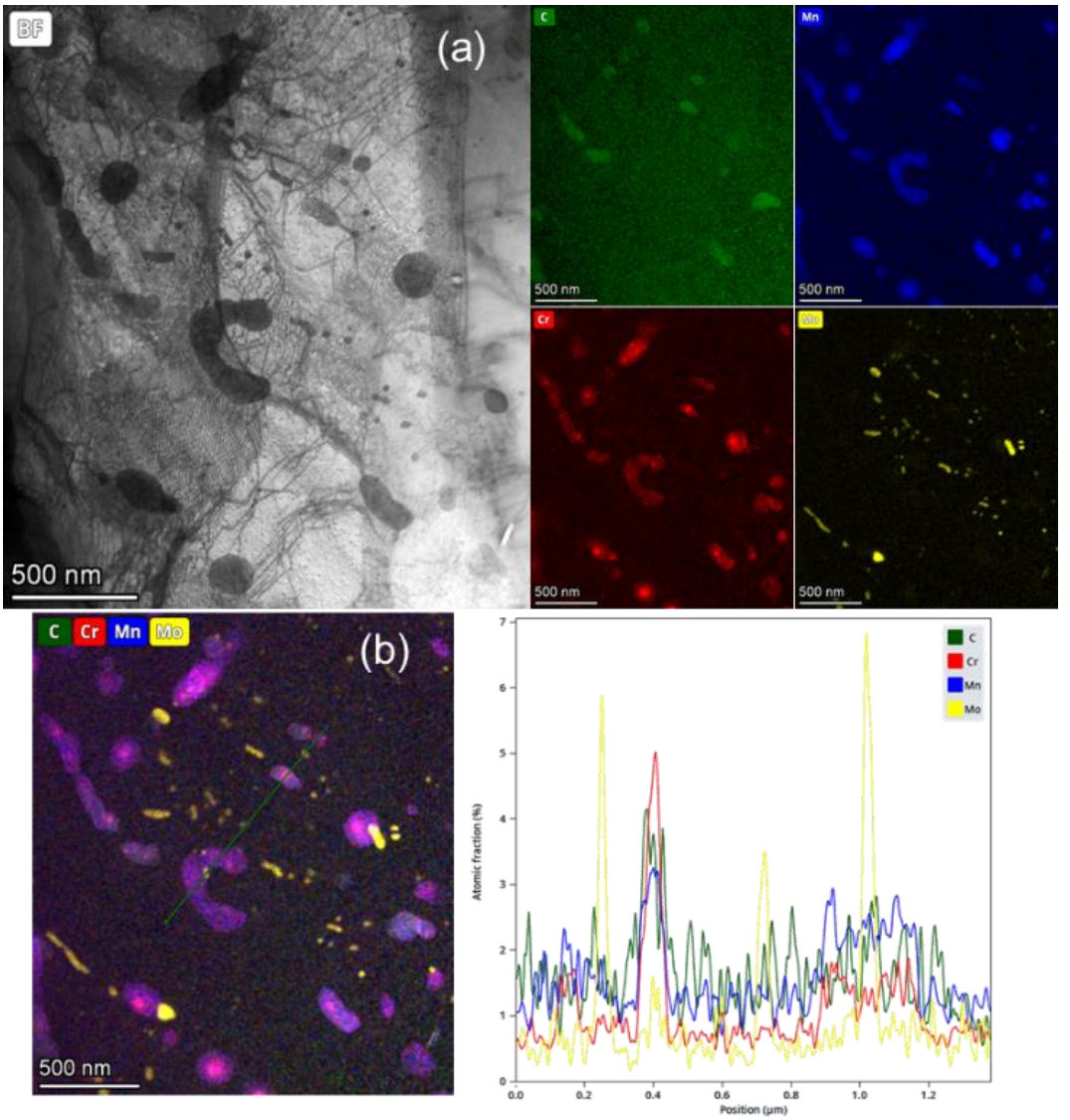

Figure 35: Carbides in HAZ of buttering AR mock-up. (a) STEM-BF image of carbide and corresponding selected elemental maps; (b) colour mix of selected elemental map and extracted line profile from line position indicated in the image.

Figure 36 demonstrates the complex microstructure in the HAZ of the buttering mock-up, where large ferrite grains mixed with bainite packets and relatively large sized carbides can be seen. With a large selected area aperture, a ring pattern is obtained which consist of both patterns from BCC phase and carbides, presented in Figure 36(b). The integrated 1D diffraction pattern from the ring pattern can be

indexed with BCC (the major reflections) and M_3C (peaks marked with red arrows). However, the lattice parameter of M_3C is slightly deviated from a stoichiometric M_3C phase.

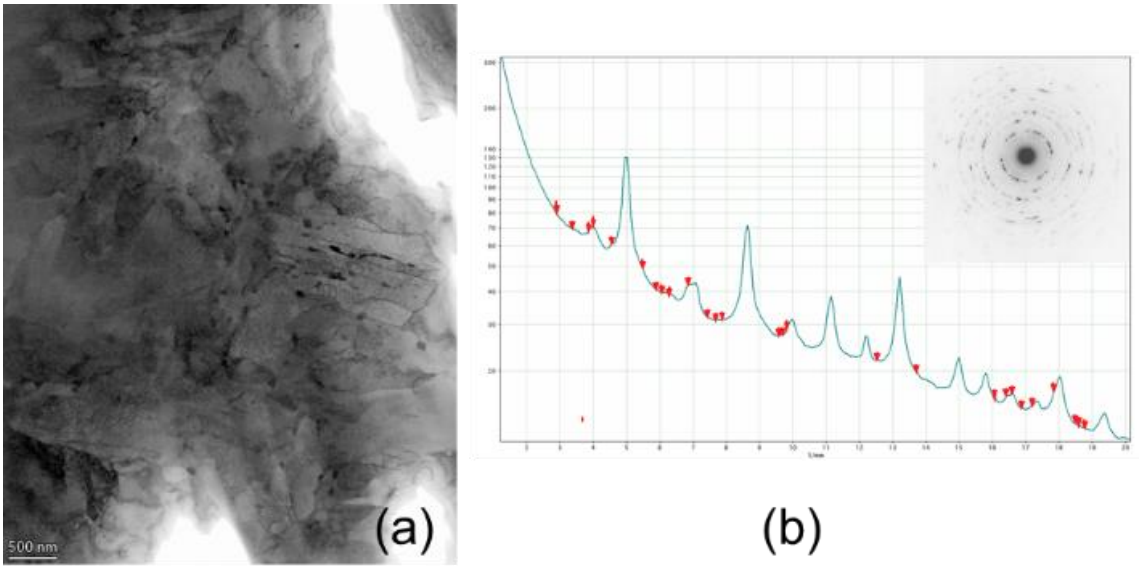

Figure 36: Buttering AR mock-up HAZ microstructure and SAED pattern. (a) STEM-BF image illustrates the ferrite grains, bainite grains and large sized carbides distribution. (b) SAED ring pattern obtained with large selected area aperture and the extracted line pattern to show M_3C peaks (marked with red arrow) and BCC reflections (peaks without mark).

The Rietveld refinement result of WAXS pattern in the HAZ of the Ringhals mock-up sample is presented in Figure 37. The pattern is quite similar to that of the TVO mock-up samples and all samples contain about 2% carbides. The buttering AR mock-up contains slightly higher ratio of M_3C carbides in the microstructure, which is in agreement with that the NG AR mock-up has more grains lacking carbides in the HAZ.

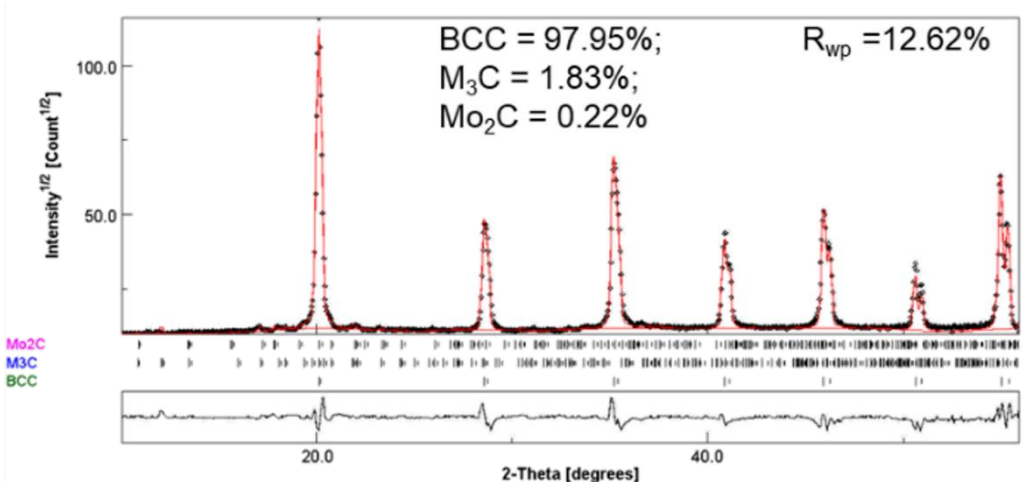

Figure 37: WAXS patterns in HAZ of Ringhals AR sample.

3.3.4 XRD measurements for tempered martensite FB

The tempered martensite FB and the surrounding area shown in Figure 27 were studied using high-resolution XRD with fine beam size of 200–250 µm, aiming to confirm the presence of tempered martensitic phase and its crystalline structure, *i.e.*, whether it is BCC or body-centre tetragonal (BCT) which is the typical martensitic crystal structure. Measuring from fully BCC area (LAS) to fully FCC area (WM), the FB was located by reaching 50% BCC of the strongest peak intensity. The first RSM at the FB in Figure 38(a) showed two strong BCC rings, 110 and 200, and one strong FCC 111 peak and one minor FCC 111 peak. The peaks correspond to the microstructure in Figure 27(d) with randomly orientated small bainitic LAS grains and two large FCC grains. Two other maps shown in Figure 38(b-c) were collected on the FCC side to maximize the diffraction from tempered martensite with two locations just next to each other along the FB. With such, the diffraction from the LAS matrix can be minimized, as only a very weak BCC 110 ring is visible. The ring patterns in all three maps fit to the cubic structure and both 110 and 200 rings do not show any sign of splitting, *i.e.*, a tetragonal crystal structure is not detected. It is worth to note that the BCC 110 plane spacing is continuously increasing with distance to the FB, which indicates that near the FB, the BCC phase is under residual compressive stress possibly due to martensite transformation.

The integrated peaks from Figure 38(a) are shown in Figure 39(b) for FCC 111 and BCC 110. After the comparison of the half widths at full maximum of these two peaks, it is evident that BCC 110 is much more broadened than FCC 111 peak, which indicates the BCC 110 belongs to tempered martensite phase with high density of lattice defects. The grain size of the tempered martensite phase is ~1 µm, as can be seen in Figure 39(a) and should not cause detectable broadening. The

Kikuchi pattern from one large tempered martensite grain from the type-B FB is shown in Figure 39(c) and a perfect Kikuchi pattern from the LAS matrix far from the FB is shown in Figure 39(d) as a comparison. The Kikuchi pattern for the tempered martensitic grain is blurred and diffused compared to the defined sharp lines of the Kikuchi pattern of the LAS matrix, indicating the presence internal distortion and lattice defects.

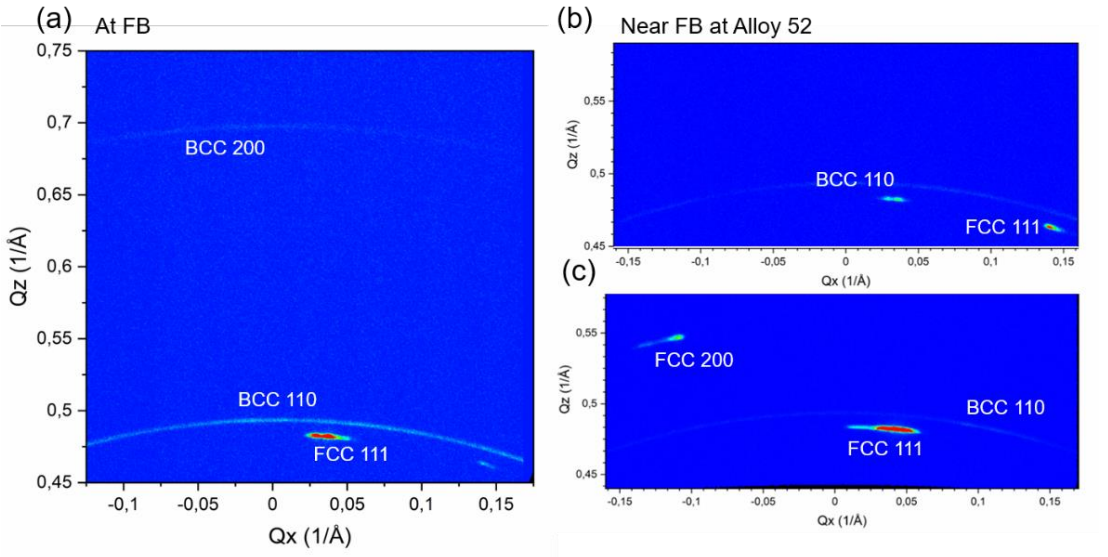

Figure 38: Reciprocal space mapping on type-B FB at the tempered martensite area. (a) At the FB; (b) at the Alloy 52 side about 120 µm to the FB; (c) at the Alloy 52 side about 120 µm to the FB and 500 µm above the measured place in (b).

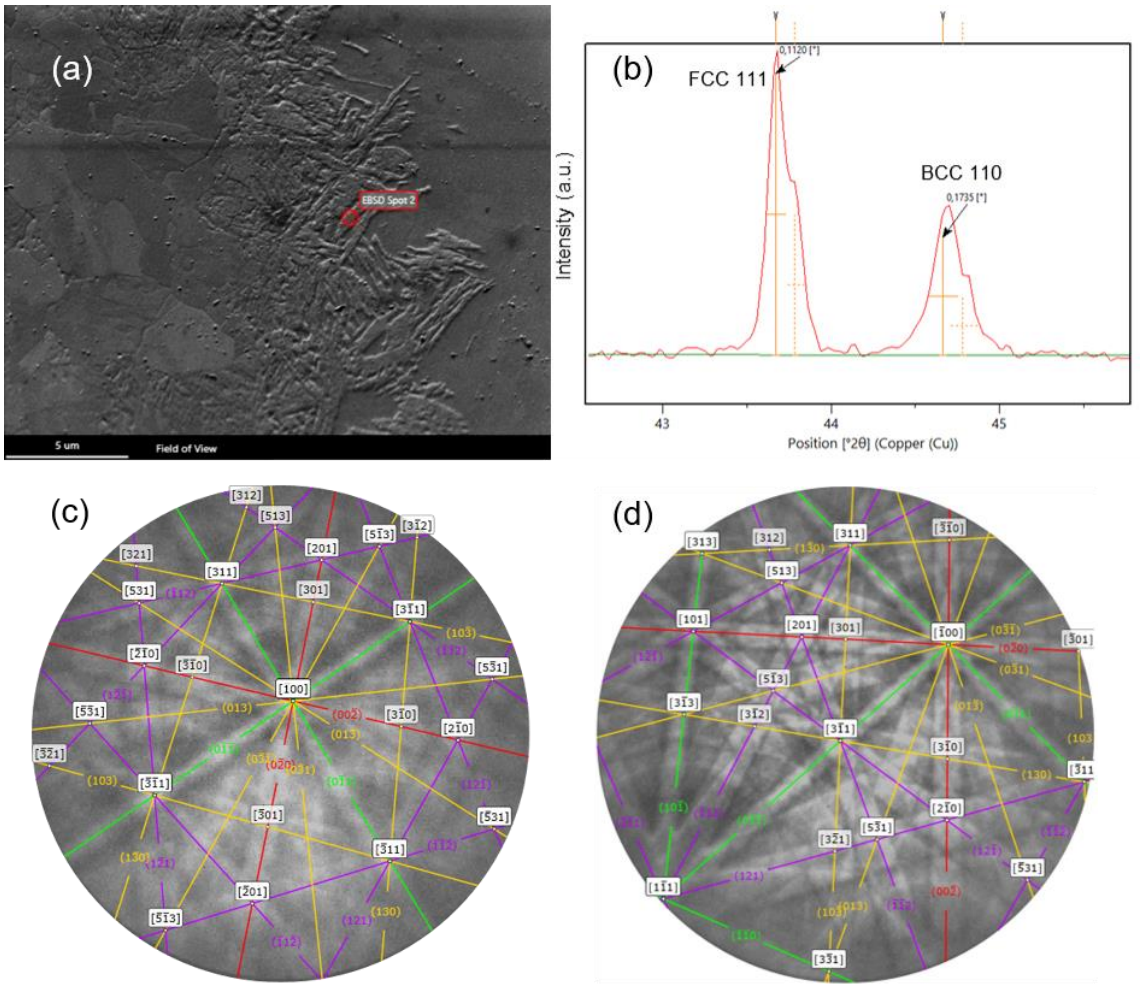

Figure 39: (a) SE image of type-B FB with tempered martensite. (b) Integrated XRD peaks from Figure 10(a). (c) Kikuchi pattern from spot marked in (a). (d) Kikuchi pattern of the BCC LAS matrix far from the FB.

4 Fracture mechanical testing

From a fracture mechanical perspective, the interface between the LAS and the Alloy 52 WM and the near-interface zones (NIZs) in the HAZ are challenging to assess due to local and global strength mismatch, varying local material properties, the wavy-features of the FB and residual stresses. There is a lack of standard/norms on how such structures should be assessed/tested

The fracture mechanical test specimens and methods used are discussed in Chapter 4.1. The mechanical test results for the TVO and Ringhals mock-ups are shown in Chapter 4.2 and Chapter 4.3, respectively. The TVO DMW was investigated in aged condition (15 000 h at 400 °C) and Ringhals DMW in reference condition.

4.1 Specimens and methods

4.1.1 Test matrix and specimens

The mechanical test matrix consists of 5*10 (thickness = 5 mm, width = 10 mm, length = 50 mm) SE(B) specimens (Figure 40) for characterisation of the T_0 transition temperature. The SE(B) specimens were side grooved prior to testing. 1×2 mm^2 miniature tensile specimens (Figure 41) are used for characterisation of the strength in the FB region. Further, 10 mm thick and 20 mm wide SE(B) specimens are used for characterisation of J-R curves, and standard size 10×10 mm^2 Charpy-V specimens (thickness = 10 mm, width = 10 mm, length = 55 mm) (Figure 42) for characterisation of the DBT curve.

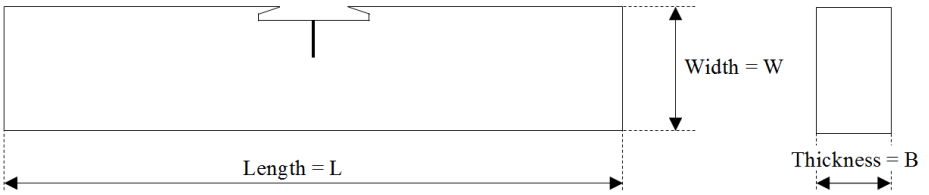

Figure 40. SE(B) specimen used for T_0 determination. W = 10 mm, B = 5 mm, L = 50 mm.

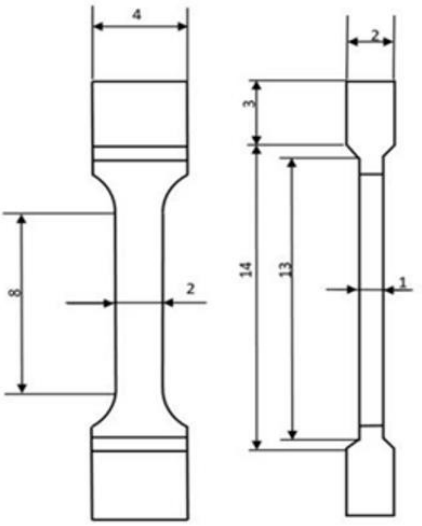

Figure 41. Miniature flat bar tensile specimen.

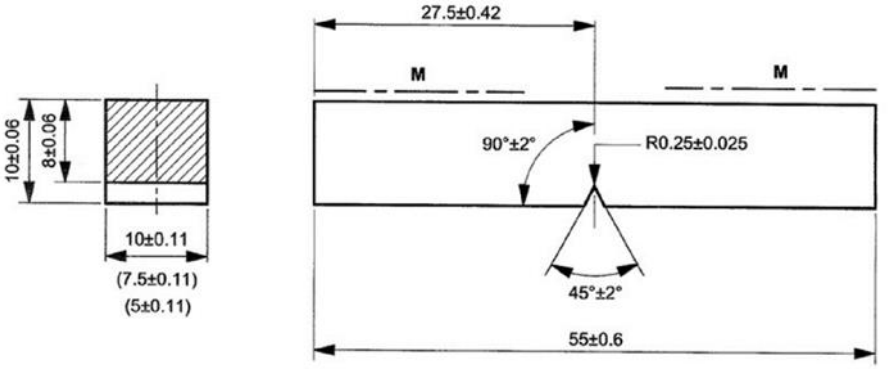

Figure 42. Charpy-V specimen.

Table 6 shows the test matrix consisting of two parts. The upper part gives the investigated fracture mechanism and the corresponding specimen, measurement type, test temperature and specimen orientation. The lower part gives the material condition and the amount of test specimens used for characterisation of the respective fracture mechanism.

The crack orientation for the SE(B) specimens for Master curve testing and the CVN specimens is in the T-L direction (transverse - longitudinal), with the same direction as a through-wall crack. The cracks of the SE(B) specimens for J-R testing are located at the FB (+/- 0.1 mm) and near the FB in the WM and BM and are placed in T-S (transverse – short) orientation. The cracks of the SE(B) specimens for Master curve testing and the notch of the Charpy-V specimens are nominally located in the HAZ of the LAS, 100–300 µm from the FB.

The tensile specimens are extracted in the transverse and longitudinal direction. The gauge length of the transversal specimens contains both WM, HAZ and ferritic base material. The specimens are extracted so that the FB is at the centre of the specimen.

Table 6: Test matrix (* = Crack distance from FB)

Fracture mechanism		**Tensile strength**	**Brittle**	**Ductile**	**Transition region**
Measurement type		ISO 6892-1	Master curve T_0 (ASTM 1921)	J-R curve J_{Ic} (ASTM 1820)	Impact toughness (EN ISO 148-1)
Specimen		1*2*8 mm^3 flat specimens	5*10 mm^2 SE(B)	10*20 mm^2 SE(B)	10*10 mm^2 CVN
Temperature		300 °C	T_0	300 °C	Close to T_{41J}
Orientation		Transverse and longitudinal	T-L	T-S	T-L
Depth in weld		any	any	any	any
Mock-up	**d_{FB} ***	**pc.**	**pc.**	**pc.**	**pc.**
TVO	+0.1 mm	-	15	-	14
Ringhals	+0.0 mm	5	15	4	-
Ringhals	+0.3 mm	3	15	4	-
Ringhals	-0.5 mm	3	-	4	-

4.1.2 Extraction of the specimens

4.1.2.1 TVO samples

Figure 43 shows a part of the TVO mock-up from which the TVO specimen were cut with EDM. The figure also includes the corresponding direction orientations. Figure 44 illustrates the orientation and extraction position of the specimens.

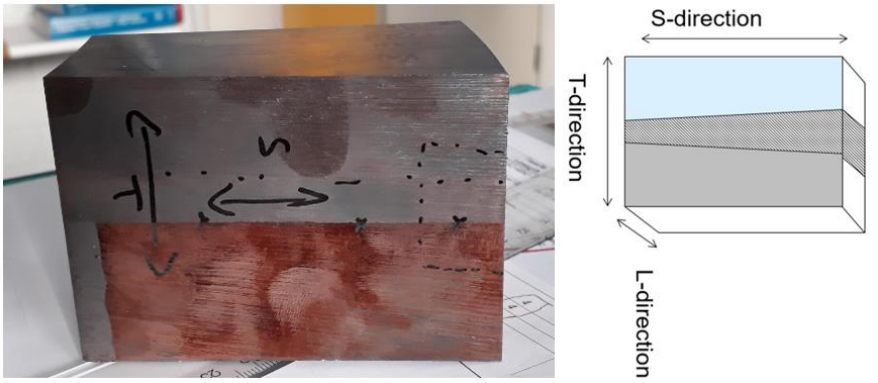

Figure 43: TVO mock-up (left) with sample orientation directions.

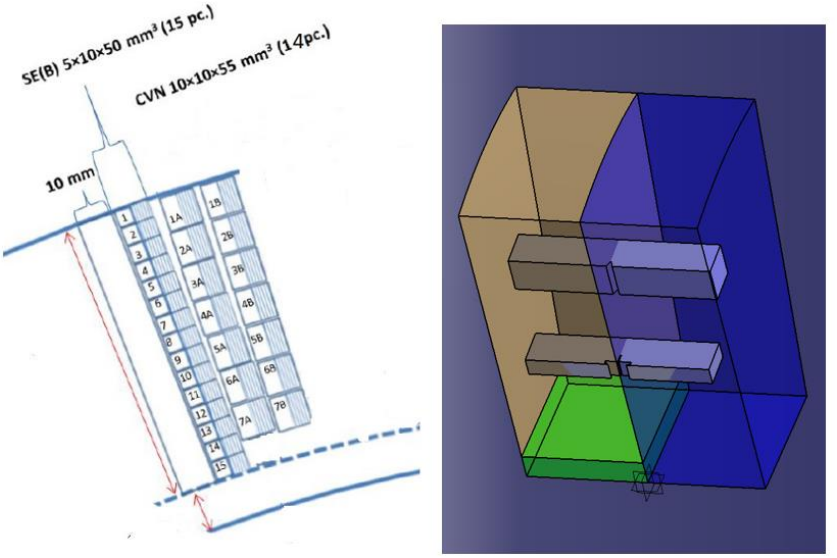

Figure 44: Specimen orientation and extraction positions from TVO mock-up.

4.1.2.2 Ringhals samples

Figure 45 shows several thinner slices of the Ringhals buttering mock-up from which the Ringhals specimens were cut with EDM. The slices were labelled P1, P2, P3 and P4. The direction orientations are illustrated by Figure 46. The specimens were named in the way that the piece where the specimens were extracted can be tracked and the location relative to the FB was given.

Figure 45: Ringhals mock-up (pieces 1-4 from right to left).

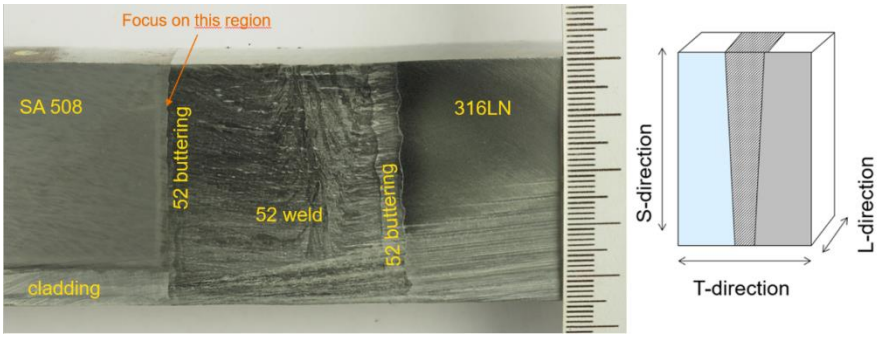

Figure 46: Ringhals mock-up with sample extraction orientation directions.

The orientation and location of the mini-tensile specimen of the Ringhals mock-up is illustrated by Figure 47 and Figure 48. Five specimens are oriented transversally - their gage length lays in T-direction and their gage section centre in the WM -0.1 mm from the FB. Six tensile specimens are oriented in longitudinal direction, three of which are positioned with their side (width = 4 mm) at the FB and in the HAZ. The side of the other three samples (width also = 4 mm) has a distance of +0.3 mm to the FB. All the mini-tensile specimen are cut from slice 3, P3.

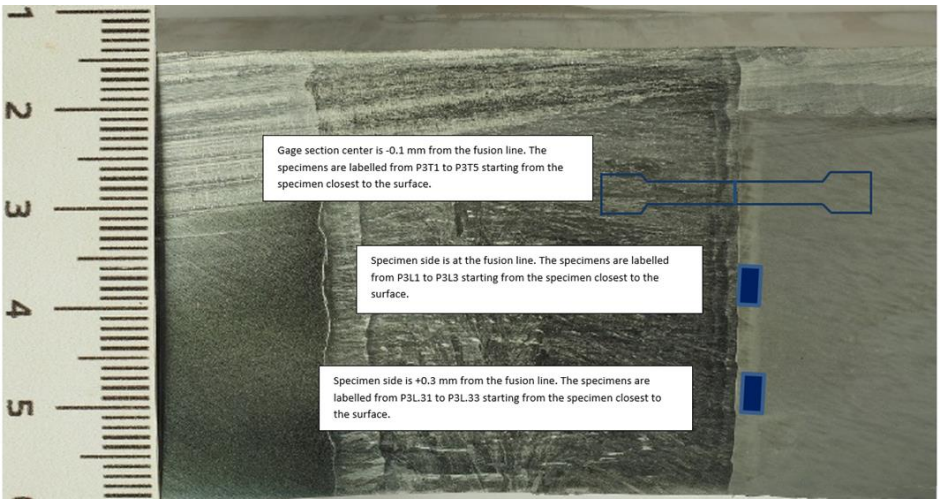

Figure 47: Mini-tensile specimen extraction locations in Ringhals mock-up.

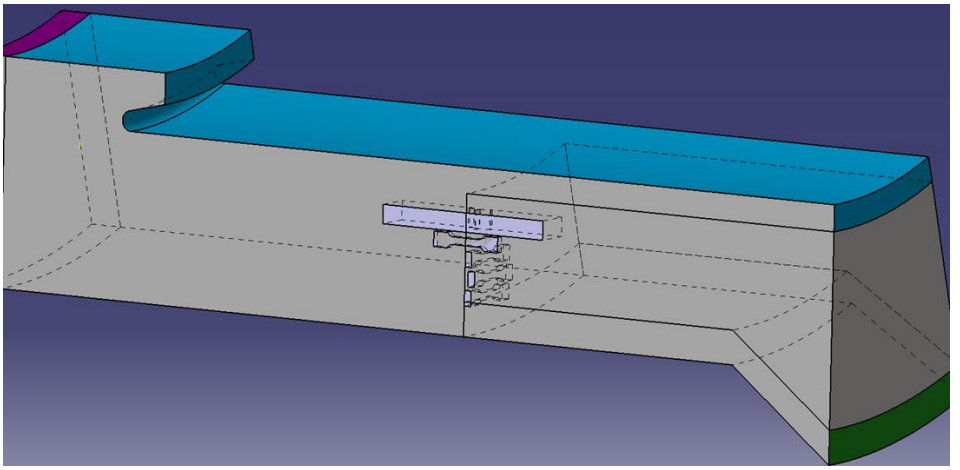

Figure 48: Mini-tensile specimens extraction location in Ringhals mock-up - larger context (P3).

Fifteen of the thirty smaller 5*10 mm^2 SE(B) specimens are positioned in the HAZ with their crack directly on the FB. These are cut from P1. The other fifteen are positioned with their cracks +0.3 mm away from the FB and in the HAZ. These are to be cut from P1, P2 and P3. Figure 49 shows a closer view of the SE(B) specimens' extraction position while Figure 50 and Figure 51 show their positions in the mock-up.

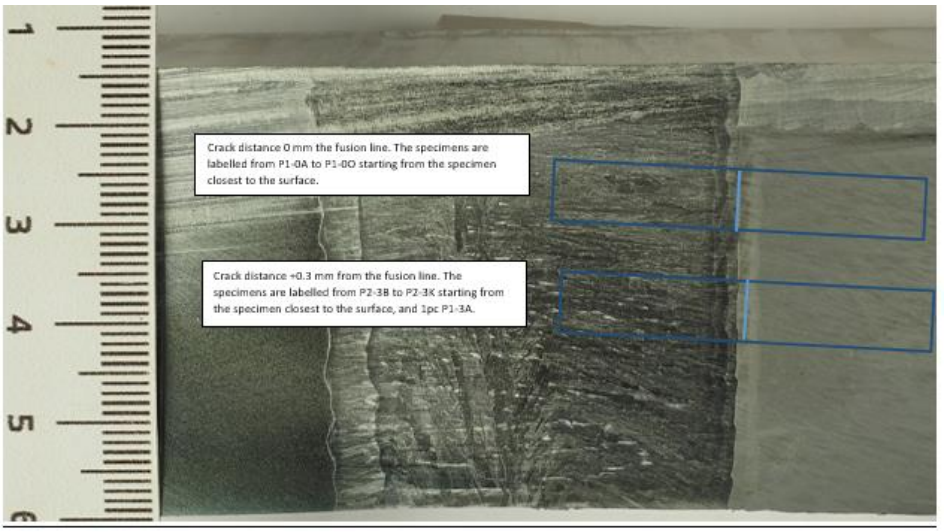

Figure 49: 5*10 SE(B) specimens extraction location – close-up.

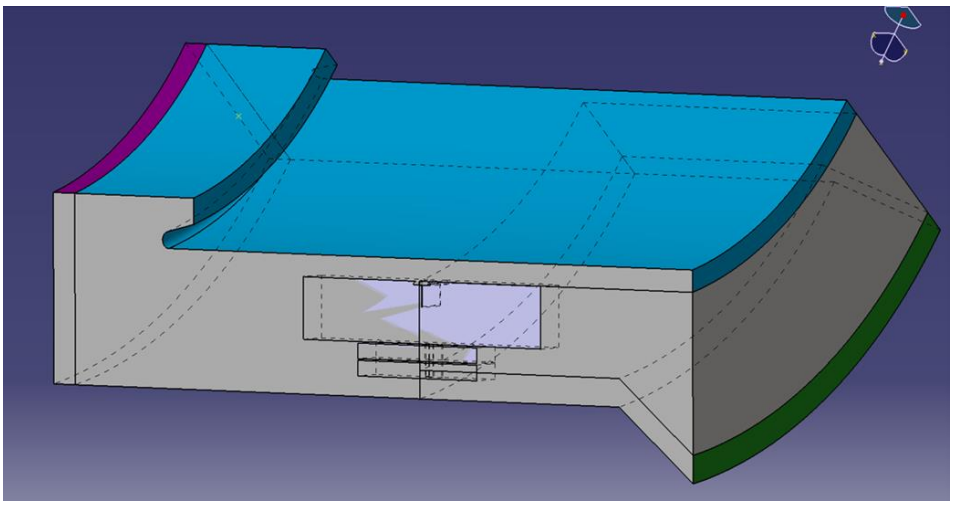

Figure 50: 5*10 SE(B) specimens extraction location – larger context (P1).

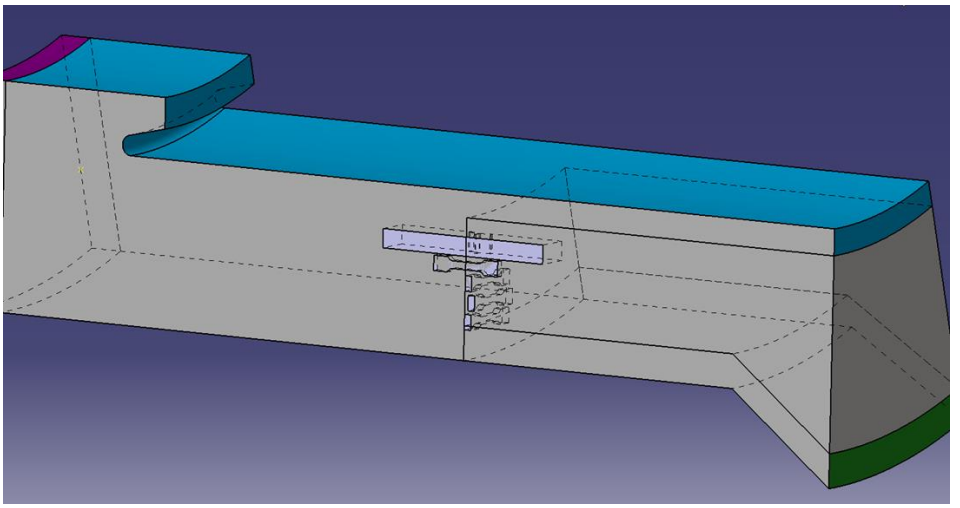

Figure 51: 5*10 SE(B) specimens extraction location – larger context (P3).

The orientation and location of the bigger 10*20 mm^2 SE(B) specimen are illustrated by Figure 52 and Figure 53. Two (2) specimens each were cut from P1 with their crack on the FB, +0.1, +0,5 and +1 mm from the FB in the HAZ. Another set of two specimens per location were cut from P2 with their cracks being in the WM at -0.5 and -1 mm from the FB.

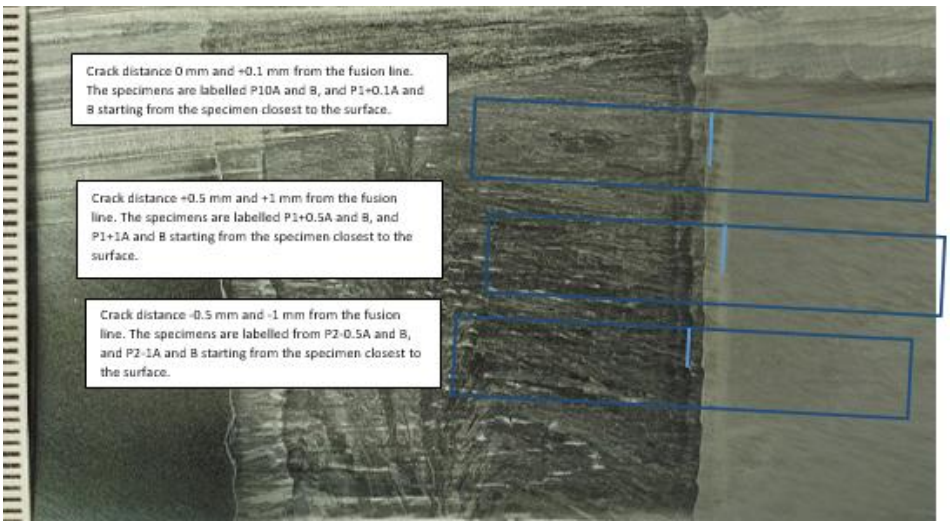

Figure 52: Orientation of 10*20 SE(B) specimens on DMW material.

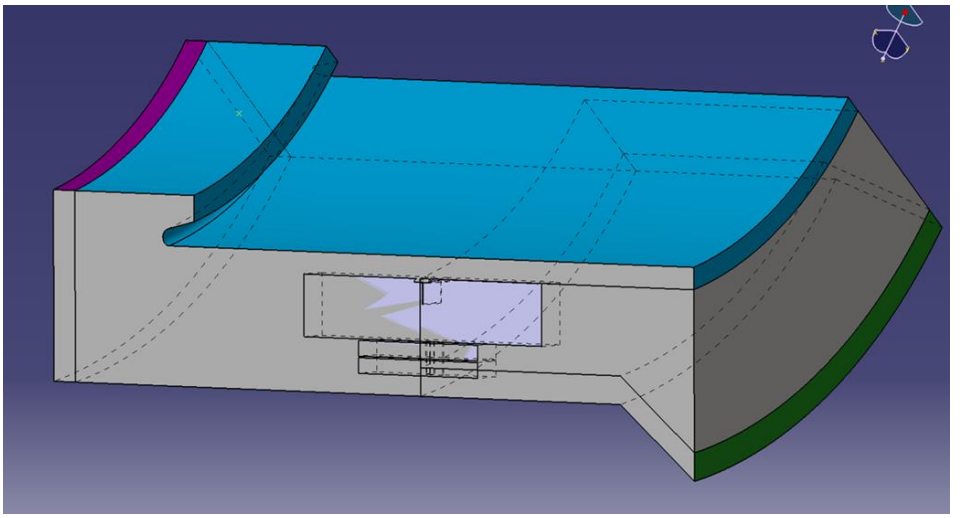

Figure 53: 10*20 SE(B) specimens extraction location (piece 1).

4.1.3 Tensile testing

The tensile testing was done according to the ISO 6892-1 standard. The tensile testing machine was a screw-driven Instron Model 1185, controlled by Inersjö Systems EDC580DOLI controller unit. The tests were operated with Inersjö CyclicEdc software. All testing was done under crosshead displacement control using displacement speed of 0.12 mm/min for determination of the yield strength and 3.2 mm/min thereafter. The speeds were calculated from the target strain rates of 0.015 mm/mm/min and 0.4 mm/mm/min, respectively, for gage length of 8 mm. The displacement speed was changed manually after exceeding the yield strength of the material.

The strain measurement was performed by image post-processing using stereo digital image correlation (DIC) technique by LaVision. The imaging and analysis software was LaVision StrainMaster DIC version 1.6.0. Two five-megapixel (2464x2056 pixels) Imager M-Lite 5M 12 bit CMOS cameras equipped with two Tokina 100 mm macro lenses were used for the imaging. The lighting was arranged with two LaVision LED light bars placed vertically between the two cameras placed on a stand. The system was run by StrainMaster controller unit connected to a PC. Analog input of the force data from the load cell was recorded by the controller unit to synchronize the images with the tensile test. The stand-off-distance of the cameras was approximately 400 mm and the stereo angle approximately 60°. The field-of-view in the specimen longitudinal direction was about 25.3 mm and thus the pixel size was about 0.01 mm. The aperture size of the Tokina 100 mm f2.8 lenses was f16 to improve the depth-of-view for the calibration as the plate filled the whole imaging area. The largest aperture size (f2.8) was used for focusing as the depth-off-view is minimized with larger aperture. Images were recorded at rate of 1 Hz with

exposure time of 20 ms. The exposure time was set so that the image exposure was about 10.5 bits.

Based on the images taken during testing, the DIC software calculates the movements of the speckle patterns. The post-processing software relies on an image-correlation algorithm. The algorithm searches for the maximum correlation in the reference image and deformed image by calculating the average gray-scale intensity over a subset. Based on the pattern movements the displacement of adjacent subsets can be calculated.

The specimen surfaces were prepared for DIC by spray painting a matte white basecoat with a primer spray paint and adding the speckles with a matte black spray paint. The feature size of the formed speckle pattern (size of the black speckles) was made roughly correct by letting the paint droplets hover onto the specimen surface by spraying in horizontal direction on a vertical specimen surface, and by adjusting the spraying distance. An example of a patterned specimen is shown in Figure 54 at the beginning of the test and prior to final fracture.

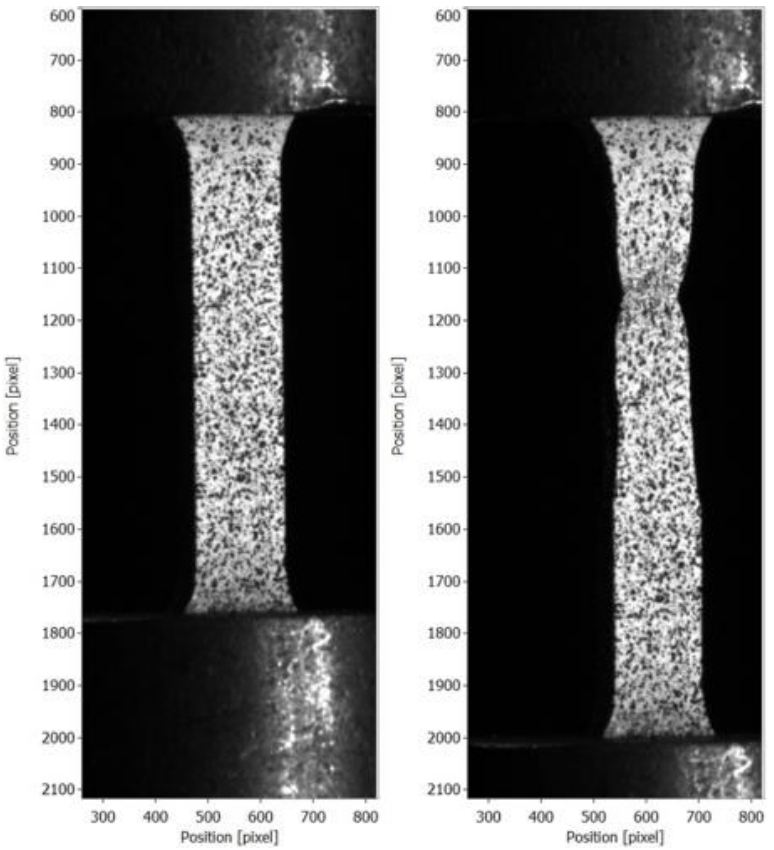

Figure 54. DIC pattern of specimen on tensile sample P3T3 (a) at the beginning of the test, and (b) prior to final fracture.

The subset size in the DIC process in the StrainMaster software was 21 pixels and the step size was 7 pixels. All images were used in the calculation and the analyses were performed relative to the first reference image in the series using the "accurate" interpolation option in the software. The strains over the gauge length were then calculated by placing an 8 mm long virtual extensometer on the measurement area. Additionally, 0.8 x 0.8 mm^2 virtual strain gauges were placed in three locations on the specimen surface to assess local strains of the weld specimens. The .csv files, containing the strains measured and the force input recorded by the DIC controller unit, were then uploaded into MATLAB for plotting. The measured thicknesses and widths of each specimen, shown in Table 7, were used in the calculation of stress.

Table 7. Tensile specimen cross-sectional dimensions.

	Cutting direction	W (mm)	T (mm)
P3L33	longitudinal	1.99	1.01
P3L3	longitudinal	2.01	1.02
P3T1	transverse	2.00	1.01
P3T2	transverse	2.00	1.01
P3T3	transverse	2.01	1.01
P3T4	transverse	2.01	1.01
P3T5	transverse	2.01	1.01

The post processing of the images and calculation of strains was performed with the LaVision software. The strains were calculated in the whole gauge section, one on ferritic base material, one on HAZ, and one on the WM, as shown in Figure 55. The size of the strain gauge in the ferritic base material was 0.8×0.8 cm^2, the size of the strain gauge in the HAZ was 0.8×0.4 cm^2, and the size of the strain gage in the WM was 1.3×1.3 cm^2. The HAZ gauge is the smallest since the variation in strength is largest in the HAZ. The HAZ strain gauge was placed 0.5 mm from the FB. The WM strain gauge is the largest, since the strain can vary locally in the WM.

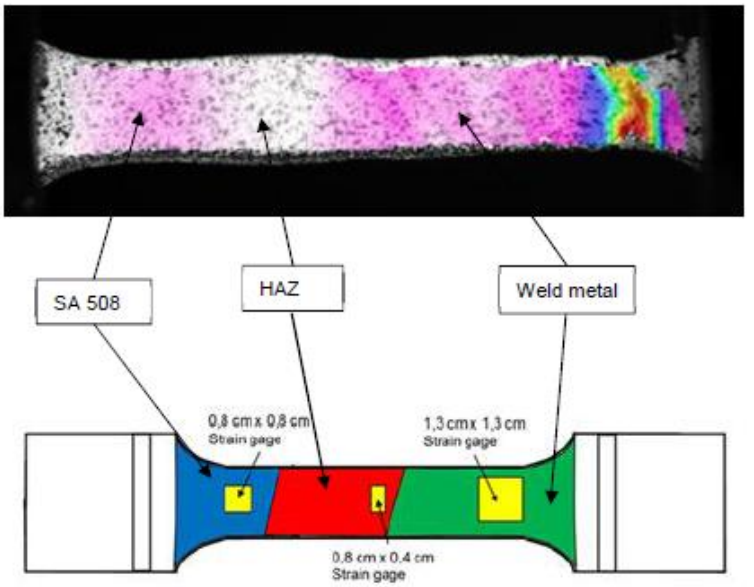

Figure 55. Virtual strain gages were placed on the specimen to obtain the stress-strain curves for the HAZ, SA 508, and Alloy 52.

From the obtained engineering strains of the different regions, the true stress and LN strain was calculated based on Equations (1) and (4).

$$\varepsilon_{eng} = \frac{\Delta l}{l_0} \tag{1}$$

$$\sigma_{eng} = \frac{F}{A_0} \tag{2}$$

$$\varepsilon_{True} = \ln(1 + \varepsilon_{eng}) \tag{3}$$

$$\sigma_{True} = \sigma_{eng} \cdot (1 + \varepsilon_{eng}) \tag{4}$$

Equations (3) and (4) are only valid until the onset of necking, because the equations are based on constant volume and homogeneous distribution of strain along the gauge length. This simplification is adequate for the analysis done here, since only the yield strengths of the different regions are analysed.

4.1.4 J-R testing according to ASTM E1820

The 10×20 SE(B) specimens extracted from the Ringhals DMW mock-up were prepared and analysed according to ASTM E1820. The specimens were fatigue pre-cracked using a resonant testing machine with load ratio R = 0.1 and the maximum stress intensity factor was less than 21 MPa√m. The target ratio between

the initial crack length and specimen width (a_0/W ratio) was 0.50. Before testing, the specimens were side-grooved, the depth being 10% of the thickness.

In the tearing resistance measurements of the pre-cracked SE(B) specimens unloading compliance method was applied. During the measurements the applied load and the crack mouth opening displacement (CMOD) were measured. The specimens were loaded in a 250 kN universal servo-hydraulic testing machine and CMOD was measured with a displacement gage, with a measurement range of 12 mm. The CMOD increment for consecutive unloading compliance measurements is 0.13 mm. The dwell time before the unloading was 20 s, and no hysteresis during the unloading sequence was observed. The loading rate was 1.3 kN/s.

After the testing, the specimens were broken in liquid nitrogen into two halves to measure the initial and final crack length. The initial and final crack length were measured using a measuring microscope. The initial and final crack lengths were determined according to the measurement technique from ASTM E1820. The measured crack length was used to validate the calculated crack size derived from the unloading compliance.

The J-R curves were calculated based on the load and CMOD, and compliance data according to Annex A1 of ASTM E1820–13. In compliance calculations, all points belonging to the linear load decrease and increase were used. The J-R curves were analysed according to Annex A8 and A9, with two exceptions. Firstly, the blunting line was determined by fitting a linear equation to the data in the blunting phase. Secondly, the J-R curves were shifted, so that the curves align with the blunting line going through the origin. After these modifications, the tearing resistance data between 0.15 and 1.5 mm offset lines was used to fit a power law relationship Equation (5):

$$J = J_{1mm} \times \Delta a^m \tag{5}$$

where J_{1mm} is the J-integral at 1 mm of crack extension, Δa is crack extension. In the J-R curve calculations the elastic modulus and Poisson's ratio were assumed to be 205 GPa and 0.3, respectively.

4.1.5 T_0 testing according to ASTM E1921

Fracture toughness testing was performed according to the ASTM E1921 "Standard Test Method for Determination of Reference Temperature, T_0, for Ferritic Steels in the Transition Range". Before testing, the specimens were fatigue pre-cracked to the initial crack length over specimen width ratio, a_0/W, of 0.5, using RUMUL resonant testing machine. In the end of the fatigue pre-cracking, the maximum value of applied stress intensity factor, K_{max}, was kept below 15 MPa√m. The fracture toughness tests were performed using MTS universal servo hydraulic testing machine equipped with a 10 kN load cell. The maximum force varied between 1.7–2.9 kN. The CMOD was measured using Epsilon 3541-003M-040M-LHT clip gage, with a measurement range of -1/+4 mm. The loading rate was kept in the quasi-static range, 0.3–1 MPa√m/s.

During testing, the load, CMOD and temperature were recorded. The CMOD-Load curve was used to calculate the fracture toughness, J_C or K_{Jc}, as described in the ASTM E1921.

After the measurements, the specimens were broken in liquid nitrogen into two halves to measure the crack lengths corresponding to the load instability moment and the possible ductile crack growth. There is no prior ductile crack growth before initiation of brittle fracture. The crack length and crack front straightness and the quality of the K_{Jc} data were checked before calculation of T_0.

Since the FB region is inhomogeneous, the SINTAP and random inhomogeneity Master Curve analyses [70] were performed. These advanced methods account for randomly distributed macroscopic inhomogeneities in the material.

4.1.6 Charpy-V testing

The notch location was checked for each Charpy-V specimen before testing. One side of each specimen was ground with 1200 grit paper. After that the specimens were polished with DiaPro Mol 3 diamond suspension and MD-Mol polishing surface. The grinding and polishing machine was Struers LaboPol-21. Etax Ba technical ethanol was used to wet the polishing surface at first and to clean the specimens after polishing. The specimens were etched with 10% Nital which includes 10% HNO_3 and 90% Etax Ba technical ethanol. Etching time was 5 s per specimen. Oxide layers were removed with hydrochloric acid which included 50% HCl, 50% H_2O and $C_6H_{12}N_4$. The specimens were rinsed in alcohol both after etching and oxide removal. The V-notches were photographed with Leica MZ12 stereo microscope and Leica DFC420 camera. Overview reprography images were taken with an Olympus E-30 camera.

The specimens were also inspected visually before testing. The following specimen dimensions were measured: transverse dimensions (b and w) and specimen length (l), ligament size, radius of curvature of the notch base (from photographs) and the angle of V-notch (from photographs). The transverse dimensions were used for scaling the photographs of the fracture surfaces when measuring the percentage of ductile fracture area. The ligament size was measured from the notch bottom to the back face with a dial gage. The notch base radius and angle of each specimen were measured optically. According to the measurements all dimensions are within the tolerances specified in EN ISO 148-3:2009 standard. No defects were observed in the specimens. Dimensions were measured with Mahr MarCal 16EW caliper, Heidenhain VRZ 404 and Leica MZ12 stereo microscope and Leica DFC420 camera.

Testing was done in accordance with ISO 148 and ISO 14556 standards. Impact toughness testing was performed using instrumented impact machine (Zwick RKP450) with automatic temperature control and feeding system. The employed test setup has a maximum impact capacity of 300 J. The gas-filled temperature control chamber is cooled by circulating liquid nitrogen. Tests were conducted at a temperature range from -180°C to 300°C. Temperature monitoring during conditioning was conducted at both the chamber level and specimen surface. Once

the aimed temperature has settled, the specimen is rapidly moved to the anvil and tested. The instrumentations yield a force-displacement curve from where you can determine the arrest (Fa), initiation (Fu) and maximum force (Fm).

4.1.6.1 Analysis of data

The absorbed energy (KV_2) is calculated from the initial and final pendulum angles measured by the angle encoder and from the pendulum parameters. The lateral expansion (LE) is measured in a stand, where the broken specimen halves are pressed against a common support surface on a position outside the lateral expansion area of the specimen. Care is taken that no specimen damage (collision marks etc.) is disturbing the measurement. The percentage of fracture appearance (FA) is measured from the photograph of the fracture surface. The specimen transverse dimensions (b and w) are used for scaling the fracture appearance measurements. The difference between the shear (ductile) and brittle type fracture cannot always be differentiated clearly by visual observation. In such cases the measured load-deflection curves may be used for guidance.

Impact toughness is characterised in terms of the mean KV_2 vs. temperature curves estimated from the test data. The curves, X = f(T), were determined by fitting the least squares function of the form:

$$X = 0.5 * [1 + \tanh\left(\frac{T-T_{50}}{C}\right)] \qquad (6)$$

where X_{US} is the upper shelf value for X (KV_2, LE or FA), T is temperature and T_{50} and C are fitting parameters.

The upper shelf value (Equation (6)) used in data analyses (X vs. T -curves) is normally fixed to the average of values showing fully ductile fracture appearance (FA=100%). For the test series analysed here the upper shelf energy (USE) is fixed based only on one or an evaluated upper shelf value. The lower shelf value is assumed to be zero. Load as function of time is measured by the instrumented striker and the load as function of deflection is calculated from this data.

The characteristic load points, *i.e.* the general yield load F_{gy}, the maximum load F_m, the onset of unstable crack propagation F_u and the crack arrest load F_a, are determined from the load-deflection curves. The load signal consists of a quasi-static load signal and a signal due to combined vibration of the striker and the specimen.

The transition criteria based on absorbed energy characterise both crack initiation and propagation, their relative proportion depends on temperature, *i.e.* the position in the transition range. In the instrumented Charpy test, the load vs. time response is recorded during the test, which produces information not only on the general yielding and initiation of brittle fracture but also on crack arrest after the brittle fracture initiation. The portion of the load vs. time (or deflection) record indicating brittle fracture initiation and arrest can easily be located in the graph from a rapid load drop occurring in the test before the final (ductile) fracture, Figure 56.

Utilising this information from tests made at various temperatures it is often possible to construct the mean crack arrest load vs. temperature curve for the material.

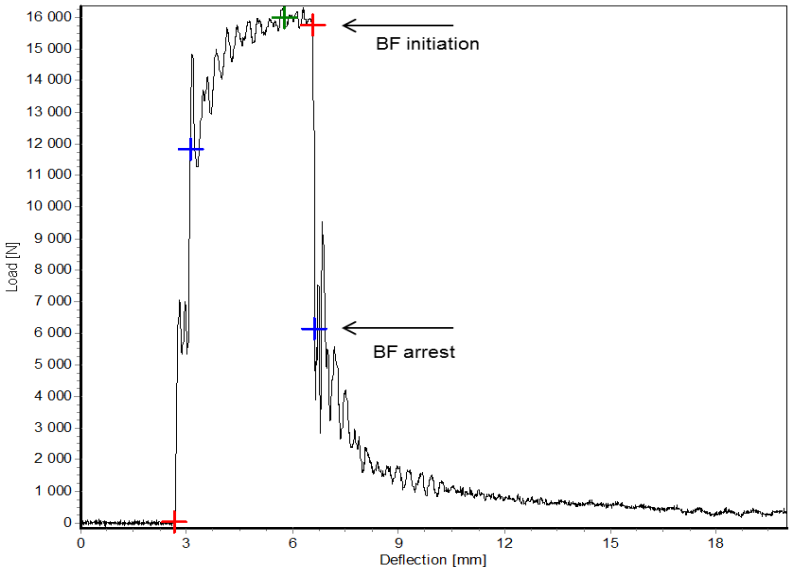

Figure 56. Example of a load-deflection graph showing loads of brittle initiation and arrest.

The instrumented impact test gives in addition to the impact energy the force-time signal. From the signal, the crack arrest force F_a was determined. The arrest force F_a was applied to assess the crack arrest transition temperature, T_{KIa}.

For comparing the crack initiation and arrest properties in terms of the fracture toughness transition temperature, T_0, the Charpy transition temperature based on a suitable criterion shall first be converted to the consistent value of T_0 using a correlation, which for the 28 J Charpy -transition temperature, T_{28J}, is as follows (ASTM E1921-13a):

$$T_0 = T_{28J} - 18℃ \quad (7)$$

where T_0 (°C) is the temperature corresponding to K_{Jc} (MPa√m) equal to 100 MPa√m.

The comparable crack arrest transition temperature T_{KIa} (100 MPa√m) can be estimated from a correlation found to exist between this temperature and that corresponding to the 4 kN crack arrest load determined by instrumented Charpy tests. The original data base, including irradiated and un-irradiated steels, shows the following correspondence:

$$T_{KIa} = T_{Fa4kN} + 11℃ \quad (8)$$

where T_{Fa4kN} is the temperature corresponding to the mean crack arrest load of 4 kN. Transition temperature T_{Fa4kN} is determined from the least squares fit by Equation (9).

$$F_a = 4\ kN * \exp\left(\frac{T - T_{Fa4kN}}{A}\right) \quad (9)$$

where F_a (kN) is crack arrest load, T is temperature and T_{Fa4kN} and A are fitting parameters.

If the specimen has deformed significantly between the load maximum and the onset of unstable crack extension, the load-deflection data may not be valid for crack arrest characterisation. Hence, relevant data points for this purpose were limited to those

$$\frac{F_u}{F_m} \geq 0.75 \quad (10)$$

where F_u is the load at the onset of unstable crack extension and F_m is the maximum load.

4.1.7 Metallography, crack path and fractography

The fracture surfaces of the tested J-R, T_0 and CVN specimens were optically imaged. Scanning electron microscopy (SEM) was used to determine the brittle fracture initiation sites of the T_0 specimens, and the fracture appearance of the impact toughness and fracture toughness specimens.

For confirmation of the crack and notch locations, and to investigate the crack path behaviour, some specimens were cut along the mid-plane or at the initiation site for brittle fracture. These cross-section samples were ground using SiC papers up to 2 000 grit, polished using diamond polishing paste up to 0.25 µm, and finally polished in a vibratory polisher using colloidal silica suspension. The surface was etched with 3% Nital to reveal the interface between the LAS and the Alloy 52 WM. The cross-sections were imaged using optical microscope and SEM.

4.2 Fracture mechanical tests of TVO mock-up

Related to thermal aging of TVO NG Alloy 52 mock-up, the DBTT shifts in the HAZ of the LAS are difficult to assess. The HAZ consists of fine microstructural regions with varying mechanical properties, grain size and possibly different tendencies for thermal embrittlement. In addition, the adjacency of the Ni-base WM can affect the sensitivity for thermal embrittlement.

The shift in DBTT can be either determined using impact toughness or fracture toughness-based testing. An impact toughness test measures the energy consumed to initiate, propagate and arrest a crack. Typically, a T_0 fracture toughness test in the DBTT region describes the stress intensity required for initiation of brittle fracture. When the impact testing is done with an instrumented device, it gives the possibility to separate the initiation and arrest portions of the result. In previous investigations on DMWs, the arrest properties have not been investigated.

Both fracture toughness testing according to ASTM E1921 and instrumented impact toughness testing (ISO 179 and ISO 148-1) are performed. The results show different shifts depending on the characterization methods. The mechanistic differences of the results are discussed. The cracks of the SE(B) specimens and the notches of the CVN specimens are nominally located in the HAZ of the LAS, 100 µm from the FB. The cracks are parallel to the FB. Table 8 shows the test matrix.

In this section, the new results obtained in FEMMA project for TVO DMW thermally aged for 15 000 h is presented. The results are presented together with the earlier results for reference condition and samples thermally aged for 5 000 h and 10 000 h [71].

Table 8. Test matrix for testing of fracture properties.

Test type	**Fracture toughness**	**Impact toughness**
Applied standard	ASTM E1921	EN ISO 148-1
Specimen type and dimensions	5x10 SE(B)	10x10 CVN
Orientation	T-L	T-L
Amount of specimens	10–15/condition	14–16/condition
Notch/crack location	LAS/WM FB, approximately 0-0.3 mm from the FB	
Investigated condition	Reference condition, thermally aged 5 000 h, 10 000 h and 15 000 h at 400 °C	

4.2.1 Fractography and crack/notch location

First the fractography and crack location investigations are presented to get a general understanding of the fracture behaviour for the investigated material. The crack path behaviour affects the fracture toughness and the impact toughness.

For most of the T_0 specimens, the fatigue pre-cracks are in the HAZ of the LAS. In few cases, the cracks are partially in the WM. Consequently, the fatigue pre-crack front is skewed and does not fulfil the crack front straightness requirement in these specimens. For most specimens, even if the cracks are farther from the FB in the HAZ, crack initiation occurs next to the FB, in the CDZ, 2–20 µm from the FB, and the final fracture occurs along the FB. Figure 57 shows an example of a crack deviating to the FB and progressing along the FB. Also, the wavy features of the underlying bead structure are visible on the fracture surface, Figure 58.

However, in four instances for the 15 000 h aged material, the brittle fracture initiation and crack progression occur in the HAZ 0.3 mm from the FB (see Figure 59). On the fracture surface of those specimens, the wavy features of the FB are not observable, and the fracture surface is smooth without crack path deviation.

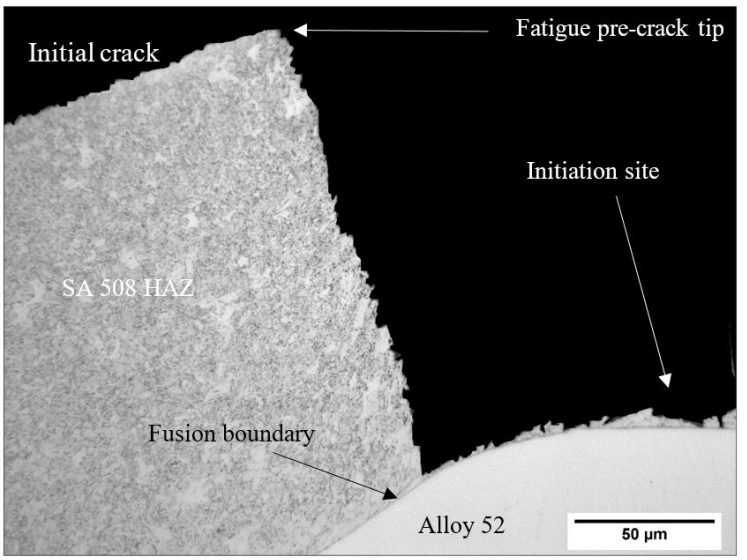

Figure 57. In most instances, brittle fracture initiation occurs in the CDZ next to the FB, even if the fatigue pre-crack is farther away from the FB. The distance between the fatigue pre-crack tip and the FB is 159 µm.

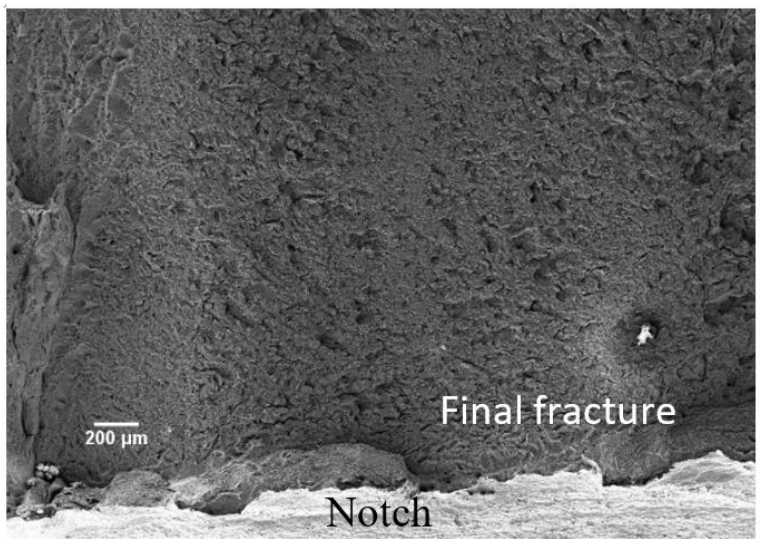

Figure 58. A SEM image of a typical fracture surface showing the wavy fracture surface appearance following the weld FB. Specimen: CVN specimen, tested in reference condition, E = 38 J, and T = –30 °C.

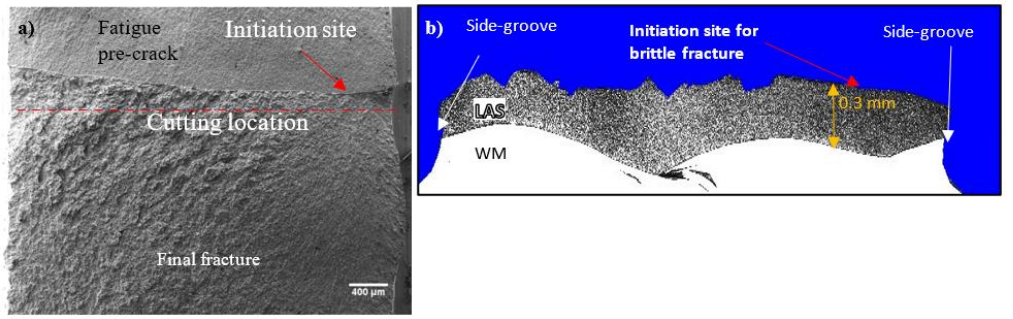

Figure 59. Specimen with lower fracture toughness. Crack propagation 0.3 mm from the FB in the LAS. Specimen: test temperature is –140 °C, $K_{Jc(25\ mm)}$ is 23 MPa√m and material condition is aged for 15 000 h at 400 °C.

For the CVN specimens fractured in the transition region, the fracture surface shows a wavy appearance following the shape of the FB, as illustrated in Figure 58. Figure 60 shows that the brittle fracture initiates and propagates in LAS close, about 0–50 µm, to the FB, even if the notch is initially farther from the FB. The crack path behaviour is similar as the fracture toughness specimens.

The scatter in the impact toughness results, presented in Chapter 4.2.3, is relatively high. The notches were visually confirmed to be located at or close to the FB. For some specimens due to notch location variations, the crack progresses slightly on the WM side before deviating to the FB. The resulting fracture surfaces

have small WM ligaments close to the notch root, see Figure 61. The crack path of specimens with higher impact energy is first located in the WM before brittle fracture initiation occurs on the LAS side.

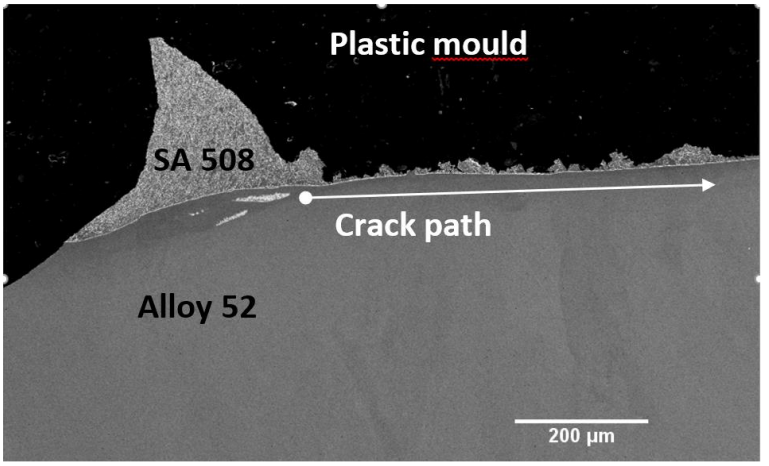

Figure 60. The cross-section for crack path assessment of a brittle CVN specimen. Specimen: reference condition, E = 38 J, T = –30 °C.

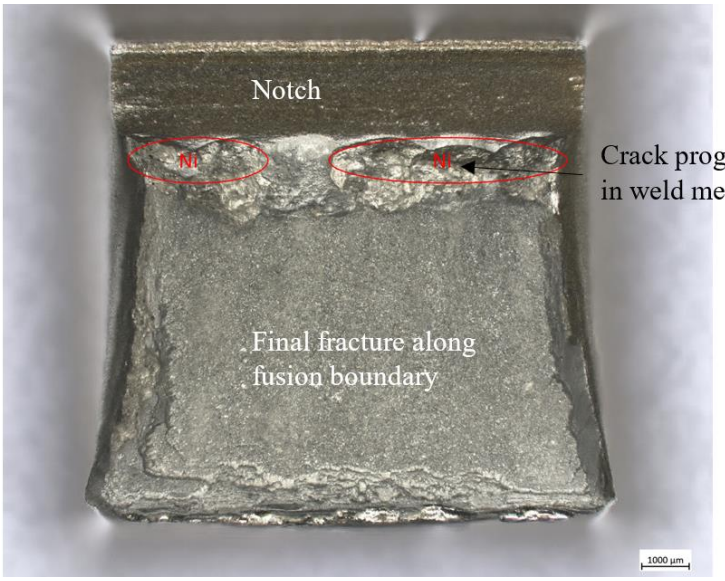

Figure 61. Partial crack growth in the WM of a CVN specimen before final brittle fracture along the FB. Specimen: testing temperature is 19 °C, impact energy is 109 J, and material condition is aged for 15 000 h at 400 °C.

4.2.2 T_0 fracture toughness

Figure 62 shows the T_0 results for the different conditions when the brittle crack initiates and progresses along the FB. In most of the analysed cases, the specimens fractured by the brittle fracture mechanism. Two specimens were excluded from the assessment since the crack is located in the WM and crack grew only with the ductile mechanism. Couple of results were excluded due to violation of the crack front straightness criteria. The other specimens fulfil the ASTM E1921 validity criteria.

The T_0 is –118 °C in AR reference condition, –111 °C for the TA 5 000 h, –129 °C for the TA 10 000 h and –134 °C for the TA 15 000 h aged material. Figure 62 and Figure 63 show the fracture toughness results for each condition separately and together, respectively.

The fatigue pre-cracks for the TA 10 000 h and 15 000 h aged specimens are located farther from the FB compared to the reference and TA 5 000 h aged condition, see Table 9. Figure 64 shows that the fracture toughness is higher when the crack tip is farther from the FB and thus, the results are not directly comparable. Based on the method presented in [72], the results for 5 000 h, 10 000 h and 15 000 h thermally aged conditions were corrected to estimate what the T_0 is, if the pre-cracks are located at 0.05 mm from FB, so that all results are comparable to the reference condition. Table 9 shows the values after applying the correction.

Table 9. Summary of the average crack locations relative to the FB and the transition temperatures for the different conditions.

Condition	**Fatigue pre-crack location** [mm]	**T_0 based on ASTM E1921**	**T_0 corrected for crack location**
Reference	0.05	–118	–118
5 000 h aged at 400 °C	0.07	–112	–105
10 000 h aged at 400 °C	0.12	–129	–111
15 000 h aged at 400 °C	0.2	–134	–109

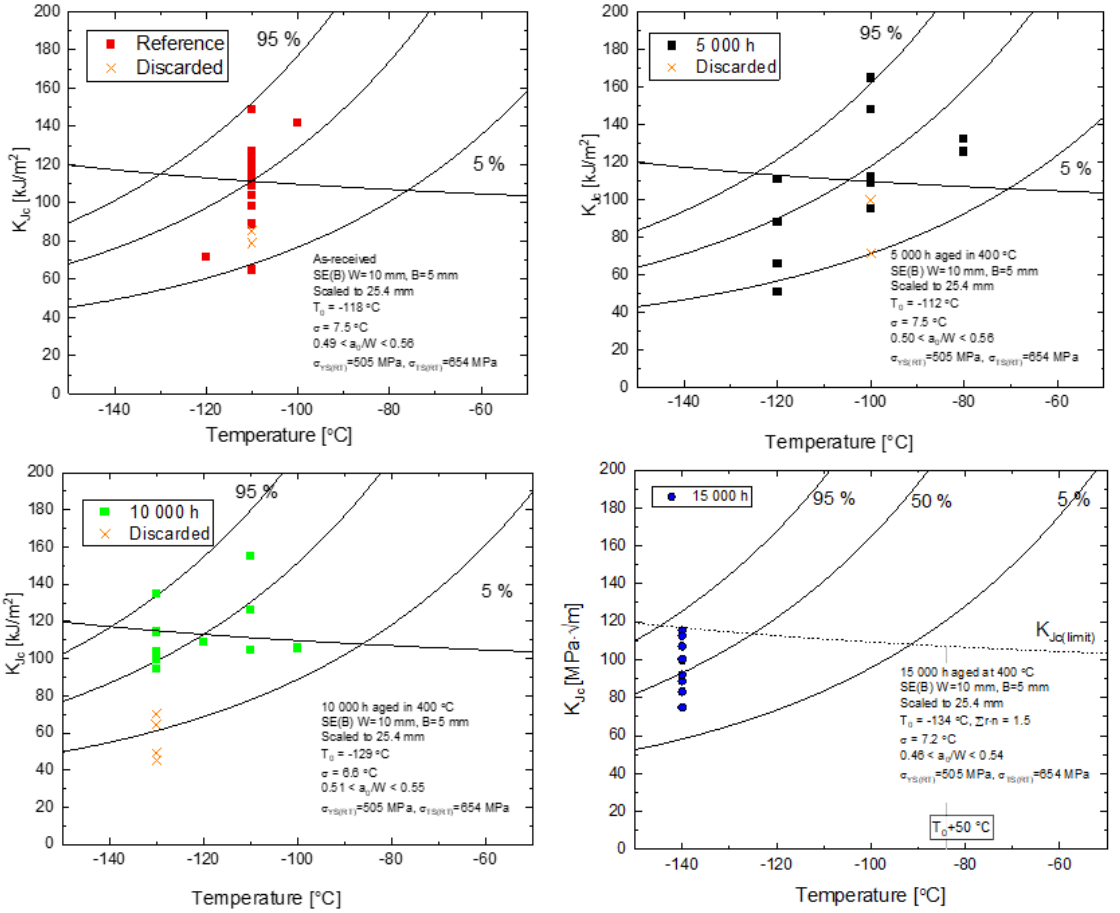

Figure 62. T_0 analyses for AR reference, 5 000 h, 10 000 h and 15 000 h aged conditions. Some data points are discarded due to failure of the crack front straightness criteria.

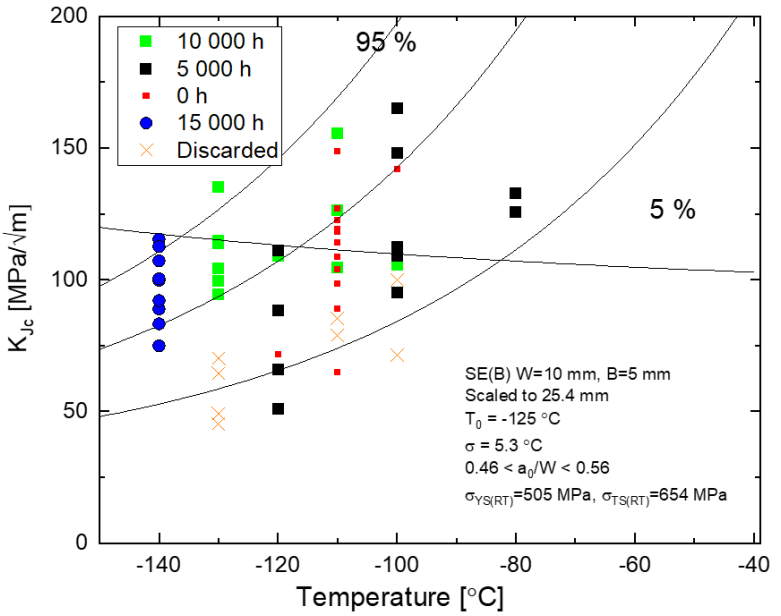

Figure 63. All T_0 results with the crack path deviating towards the FB.

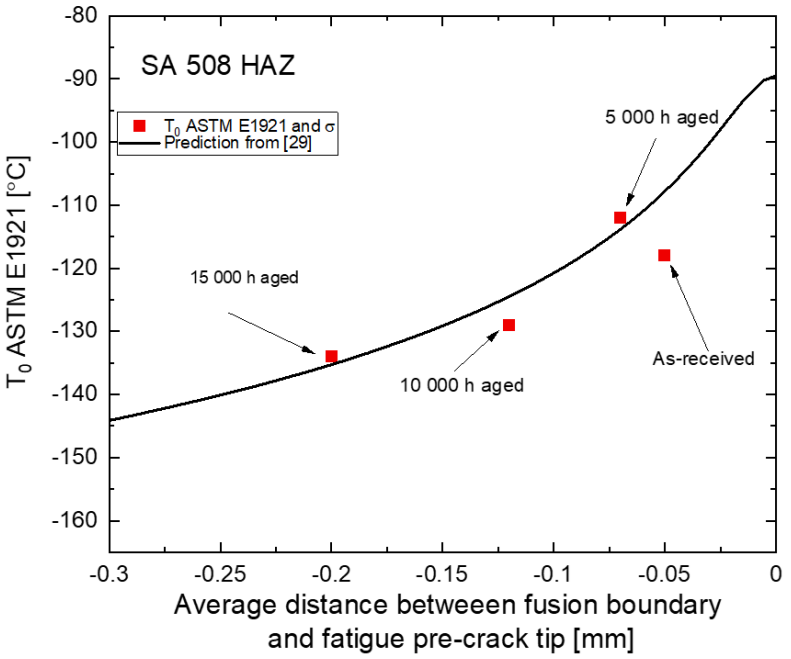

Figure 64. T_0 as a function of the distance between fatigue pre-crack tip and FB.

The fracture surfaces and crack paths of two discarded specimens with crack curvature profile above the allowable limit were investigated in more detail to better understand the crack path behaviour and see if some of the low toughness specimens tested in previous projects have similar crack path behaviour as observed for the 15 000 h TA specimens. In the selected cases, the material was aged for 10 000 h and the fracture toughness is closer to the Master Curve 5% lower bound of the data. Figure 65 and Figure 66 show that the crack fronts are relatively curved. The cross-sections show that the crack front is located partly close to the FB and partly farther from the FB in the HAZ. Initiation occurs at a location where the crack is closest to the FB.

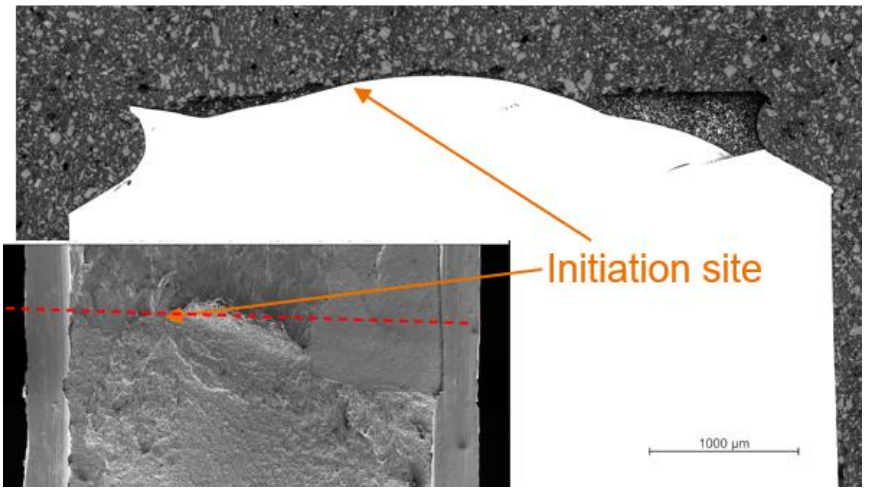

Figure 65. Fractography and cross-section. Sample condition TA 10 000 h.

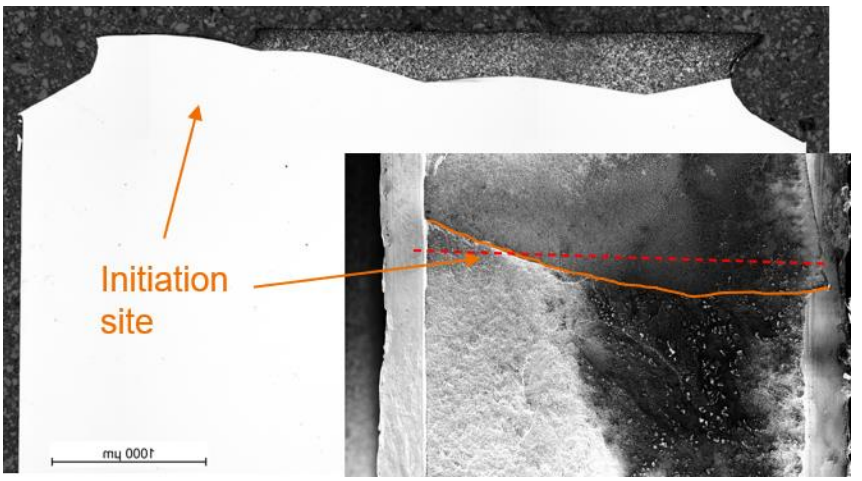

Figure 66. Fractography and cross-section. Sample condition TA 10 000 h.

For the other specimens, characterized in previous projects, the profiles of the crack paths have been determined using a profilometer. Already based on visual inspection a crack jump can been seen at the fracture surface. The cracks deviate to the FB and progresses along the FB. Figure 67 shows the fracture toughness (expressed as $T_{0(effective)}$) as a function of distance of the fatigue pre-crack tip to the FB. The fracture toughness increases with the distance to the FB. The largest deviations to the FB are 0.3 mm. For the 15 000 h TA specimens, no deviation was observed when the distance to the FB is 0.3 mm. The result indicates that there is a threshold after what the crack no longer deviates the FB. The deviation can be affected by the local microstructure at the FB.

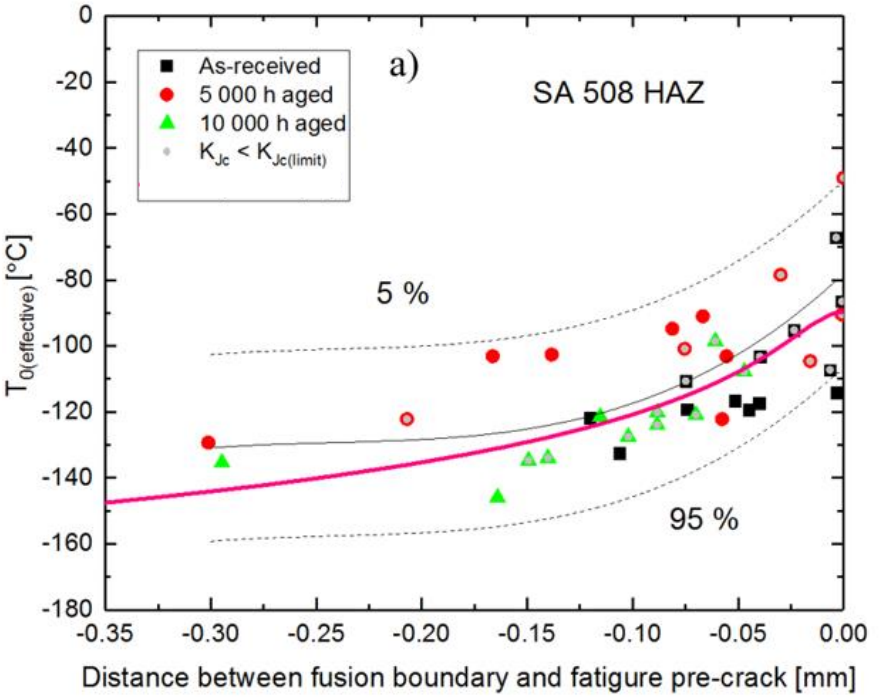

Figure 67. Dependence between fracture toughness and crack location in the HAZ.

4.2.3 Discussion on T_0 for 15 000 h aged condition

For four specimens aged for 15 000 h, the crack initiation and propagation occur only in the HAZ approximately 0.3 mm from the FB (see Figure 59). For these four samples, a smooth fracture surface close to the initiation site is typical, Figure 59, without abrupt crack path deviation. The fracture toughness is lower compared to the specimens with crack path deviation to the FB, see Figure 68 where all the 15 000 h TA results are analysed together and T_0 is then –129 °C. The average fracture toughness is 36 MPa√m at –140 °C, and the resulting invalid T_{0q} is 62 °C. A valid

T_0 estimation according to ASTM E1921 cannot be determined with only 4 observations. Since the crack path behaviour differs from the other specimens, the results are treated separately.

If the inhomogeneity assessment is applied to all of the 15 000 h TA data, the statistical lower bound curve estimate varies depending on the chosen method. The inhomogeneity MML assessment gives an average T_{0MML} = –108 °C and the standard deviation is σ_{T0M} = 44 °C. These values result in the MML estimate. The SINTAP method from ASTM E1921 results in a more optimistic estimate (Figure 69). $T_{05\%(MA)}$ estimate accounts for the uncertainty in the MML estimate and results in a margin corrected T_0 of –42 °C.

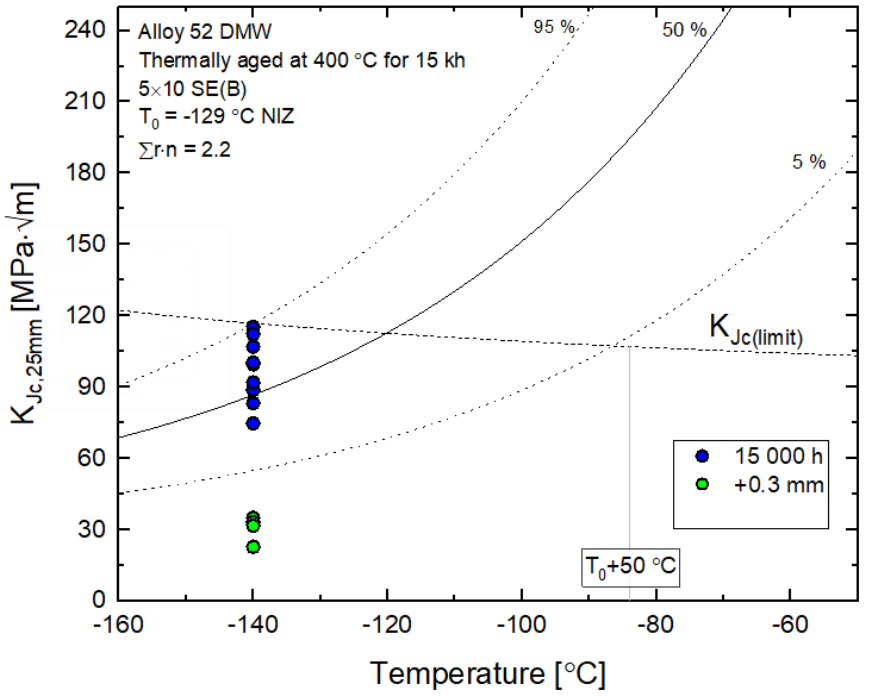

Figure 68. T_0 analysis of TVO mock-up samples with condition TA for 15 000 h.

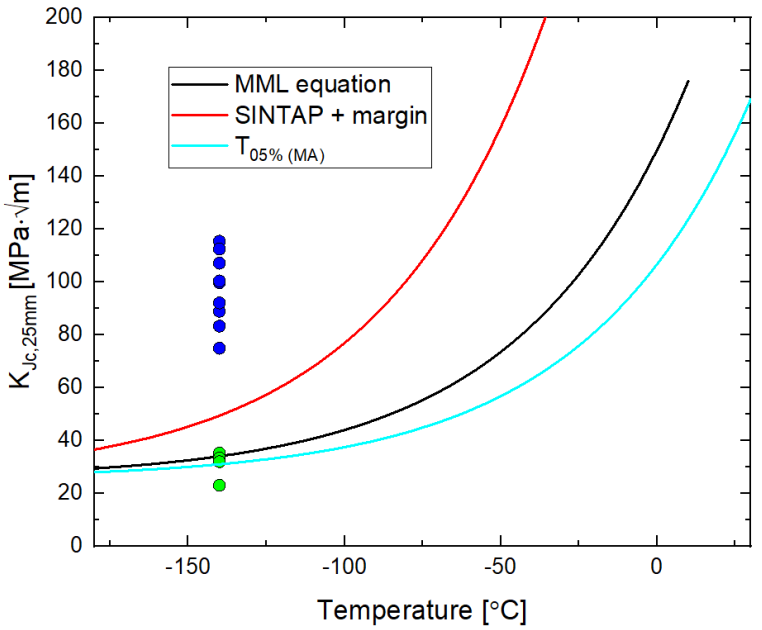

Figure 69. 5% lower bound estimate for the 15 000 h condition.

Evidently, the results show that as the distance to the FB increases a point is reached where the properties of the hard zone dominate the fracture behaviour and the crack does not deviate to the FB. Additional characterization is required to obtain a valid T_0 of the region 300 µm from the FB but is outside the scope of the ongoing project. If the focus is on the region approximately less than 200 µm from the FB, the fracture toughness after 15 000 h of aging at 400 °C is aligned with the earlier results, *i.e.* the thermal aging treatment does not affect significantly the transition temperature.

For the rest of the 15 000 h TA specimens with the crack closer to the FB, a characteristic abrupt deviation of the crack path from the HAZ towards the FB can be observed on the fracture surface, Figure 70. The cross-section image of one specimen, Figure 71, shows that the crack deviates to the FB after initiation and progresses along the FB. Also, the wavy features of the underlying bead structure are visible on the fracture surface. For the NG DMW, the T_0 is −134 °C for specimens with the initial crack close to the SA 508/Alloy 52 FB, and with the crack deviating towards and propagating along the FB.

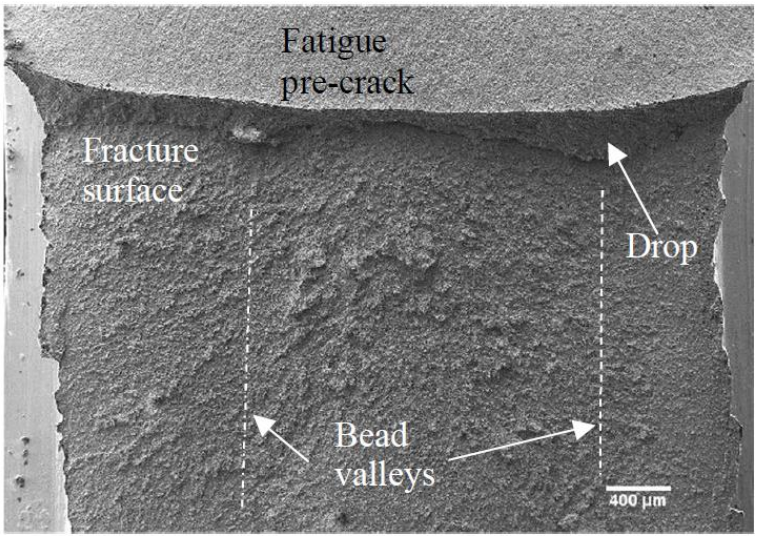

Figure 70. Fracture surface of a high fracture toughness specimen.

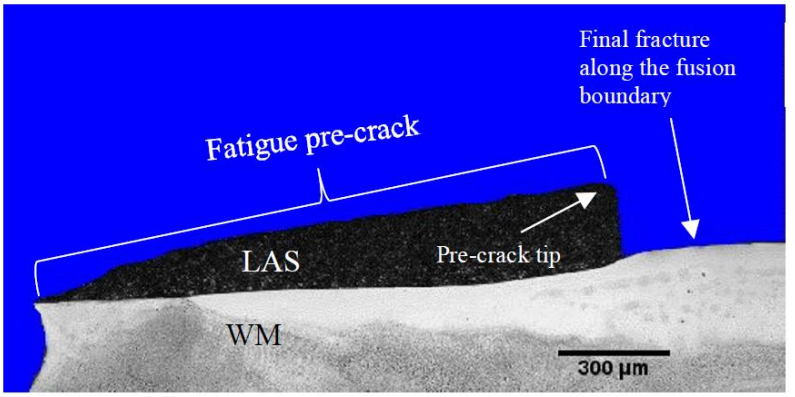

Figure 71. Cross-section of a high fracture toughness specimen in the crack growth direction.

4.2.4 Impact toughness

Figure 72 shows the impact energy-based transition curves for the AR reference, 5 000 h, 10 000 h and 15 000 h aged conditions. The transition curve shifts to the right as the material aging time increases. The scatter is relatively high for the AR reference and 15 000 h aged conditions, due to variations in notch location and partial crack growth in the WM, as explained in Chapter 4.2.1. Due to this reason, for the 15 000 h aged condition, the location of the transition curve for the HAZ cracks was estimated based on the lower boundary results. Table 10 summarizes

the T_{42J} and T_{28J} transition temperatures and upper-shelf energy (USE). In the transition curve fitting process, the USE was determined by calculating an average USE for the different conditions, since previous results indicate that thermal aging does not significantly affect the USE [36].

Figure 73 shows that the arrest force values decrease and that the arrest transition curve shifts towards the right with increasing aging time.

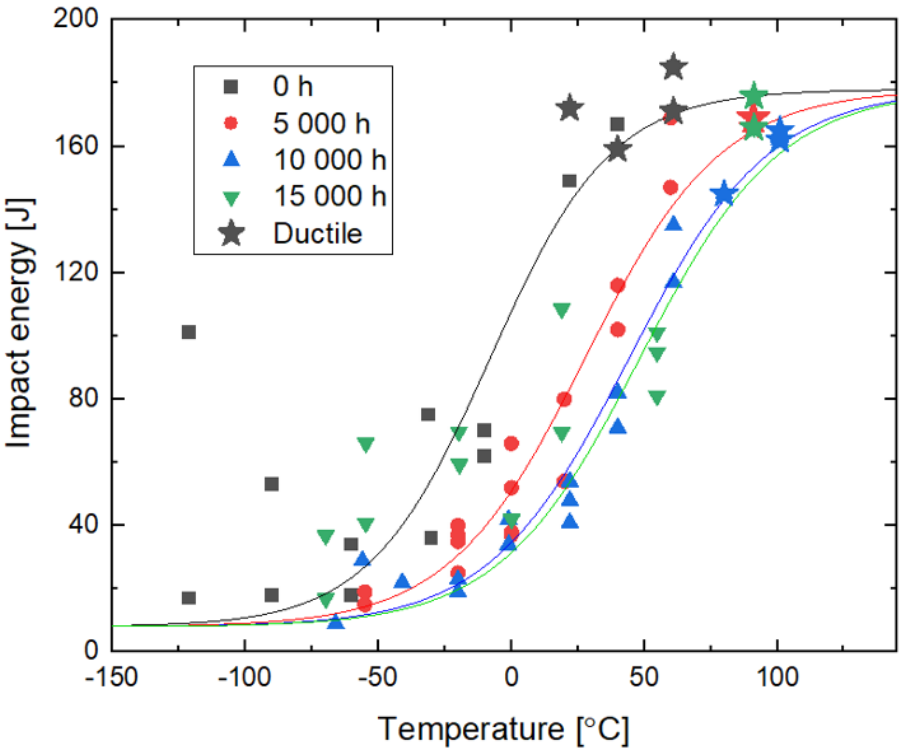

Figure 72. Transition curves of impact energies for the AR reference, 5 000 h, 10 000 h and 15 000 h aged conditions. The star symbols indicate 100% ductile fracture.

Table 10. Summary of transition temperatures and upper shelf values measured for the AR reference, 5000 h, 10000 h and 15 000 h aged conditions.

Material	T_{28J}	T_{41J}	USE	T_{Fa4kN}	T_{KIa}
	(°C)	(°C)	(J)	(°C)	(°C)
Reference	–54	–40	172	–27	–16
Ageing, 5 000 h	–24	–9	168	–15	–4
Ageing, 10 000 h	–9	7	164	0	11
Ageing, 15 000 h	–5	11	171	7.5	19

A power law equation, the transition curve, was fitted to the arrest force, F_a, data

$$F_a = 4 * exp\left(\frac{T - T_{Fa4}}{A}\right) \quad (11)$$

where T_{Fa4kN} is the arrest force at the temperature corresponding to 4 kN connected to a crack jump halfway through the component, T is the test temperature and A is a fitting parameter. The fitting parameter was selected to be the same for all conditions, A = 23. The results exceeding 8 kN were not included to the fitting since at high crack arrest forces, where the crack jump is small, the results may be affected by the initiation force. Also, specimens with significant crack growth were excluded by applying F_u/F_m (initiation force/maximum force) > 0.7 criteria, otherwise the measured crack arrest force can be lower than the true crack arrest force [73].

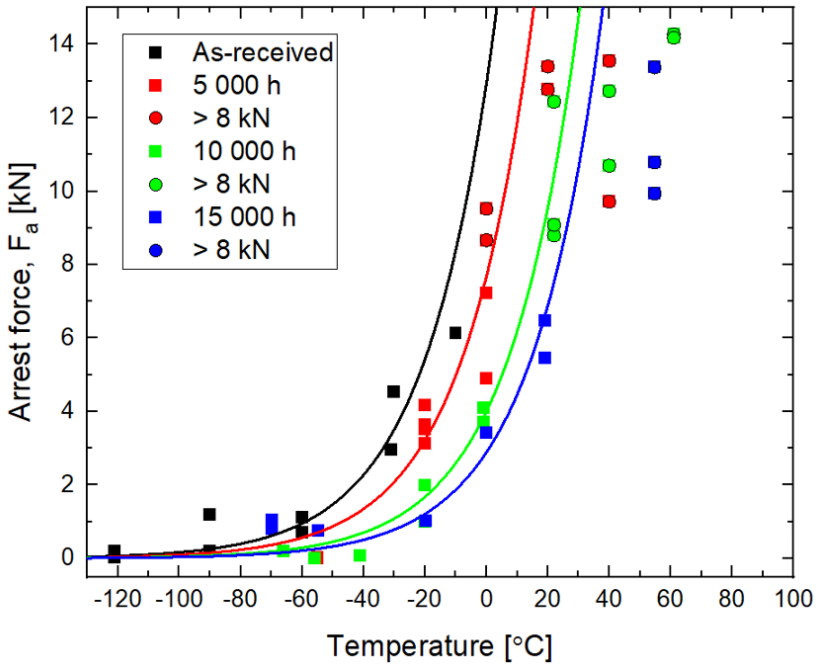

Figure 73. F_a-T curves for the different conditions.

4.3 Fracture mechanical tests of Ringhals mock-up

4.3.1 Tensile tests

The true stress-strain curves measured with the 8 mm virtual extensometer for all transversal mini-tensile and two longitudinal specimens performed at room temperature are shown in Figure 74. The tensile properties are listed in Table 11.

The specimens P3L3 and P3L33 have much higher yield strengths and tensile strengths as they were manufactured from the HAZ in the longitudinal direction. On the other hand, the elongations to fracture are lower when compared to the weld specimens, as expected. The strength of the weld specimens is mostly dictated by the softer Alloy 52 WM, as deformation of the SA508 side mostly stops after localization of deformation occurs in the WM that has much lower yield strength.

In general, the trend of the tensile curves is similar for all similar specimens with most of the difference coming from slightly different elongations to fracture. It should be noted that test data of specimen P3T1 was interrupted during testing due to an error in the DIC software.

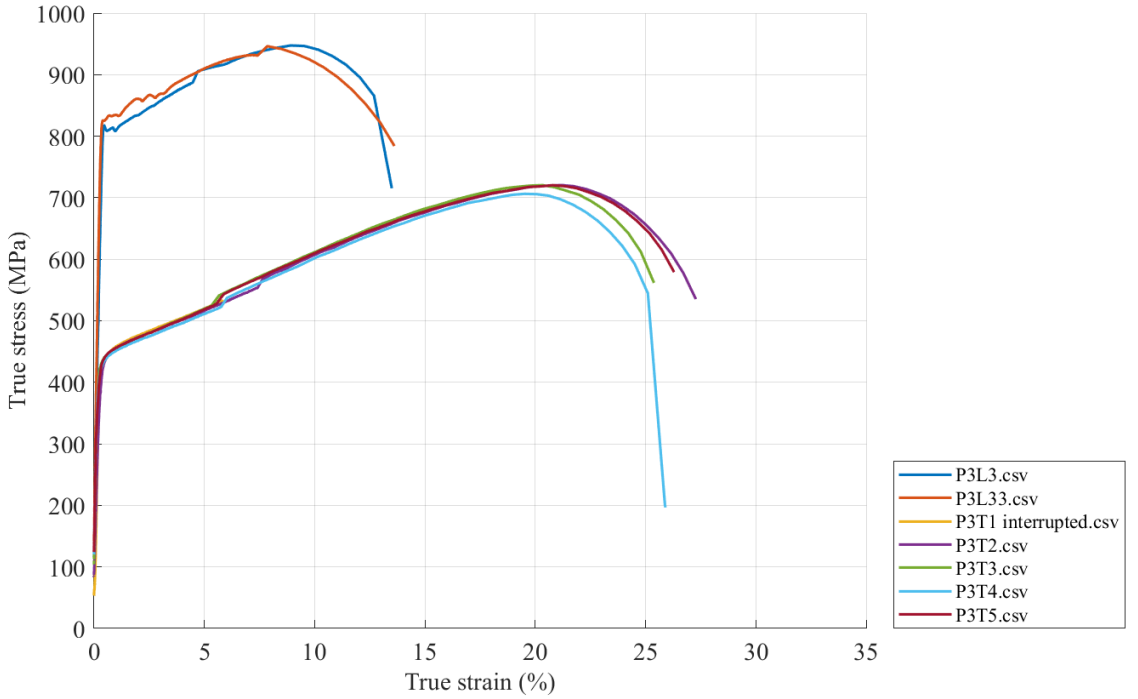

Figure 74: True stress-strain curves for the P3 specimens measured with an 8 mm virtual extensometer.

Table 11: Tensile properties determined from true-stress strain curves

Specimen	Specimen location	σ_{ys} [MPa]	σ_{uts} [MPa]	Elongation to fracture [%]
P3L33	HAZ 1.3 mm from FB	827	947	13.5
P3L3	HAZ 1 mm from FB	820	946	13.6
P3T1	Transversal 50 % WM/LAS	439	n/a	n/a
P3T2	Transversal 50 % WM/LAS	430	720	27.3
P3T3	Transversal 50 % WM/LAS	440	720	25.4
P3T4	Transversal 50 % WM/LAS	432	706	25.9
P3T5	Transversal 50 % WM/LAS	440	720	26.3

Figure 75 contains the true stress-strain curves measured with the three virtual strain gages for the different weld specimens. The three different areas (BM, HAZ, WM) are separated by colour. Figure 76 to Figure 78 show the curves separated according to the measurement area. The HAZ and BM curves remain low as the strains are distributed early into the softer WM, and the higher strength of the base material is not fully utilized. The HAZ and WM curves are similar indicating that they were most likely both measured in the WM.

The differences in elongations to fracture measured with the virtual strain gages are mostly caused by differences in the location of the virtual strain gage in relation to the site of the final fracture (for example in case of P3T4). The closer the strain gage is to the final fracture zone, the higher the local strain measurement in that region becomes. The highest local strains are experienced in the necking / final fracture zone that converge into a local maxima. The magnitude of the measured local maxima depends on the spatial resolution of the measurement and length scale of the strain measurement in relation to the real deformations that the material experiences. In theory, the measured maxima would converge at some point into a specific maximum value, if the spatial resolution of the measurement was high enough when compared to the real deformation that the material experiences, most likely in the length scale of the materials microstructure.

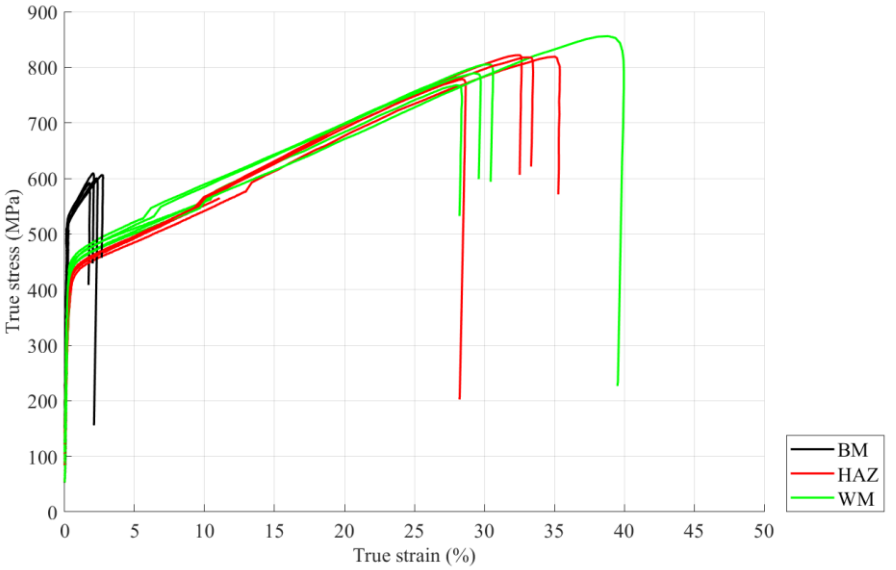

Figure 75: True stress-strain curves of BM, HAZ, and WM for the five P3T specimen.

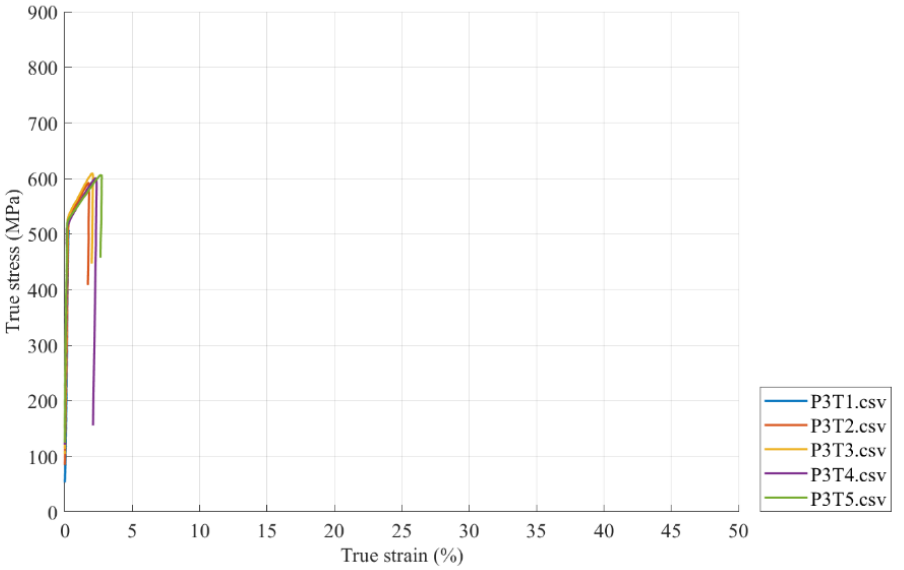

Figure 76: True stress-strain curves of BM for the five P3T specimens

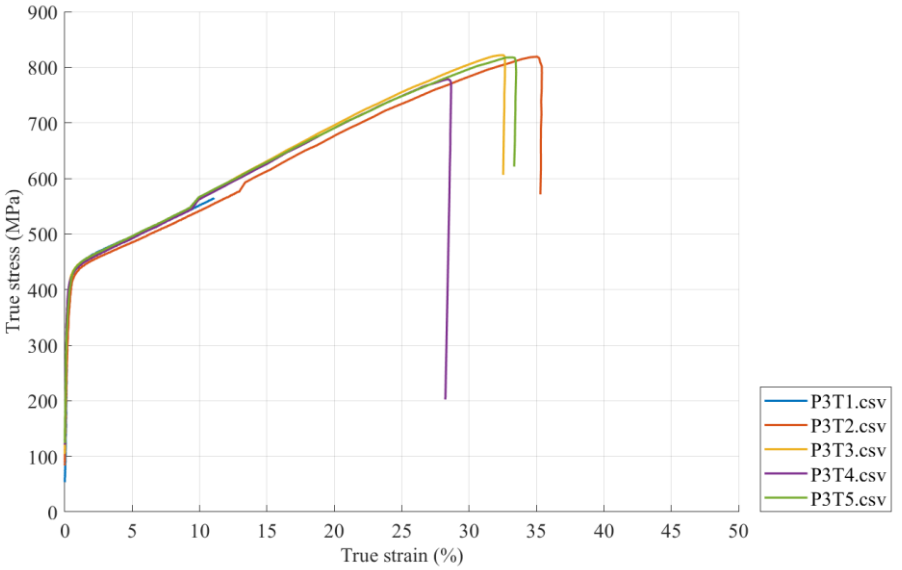

Figure 77: True stress-strain curves of HAZ for the five P3T specimens

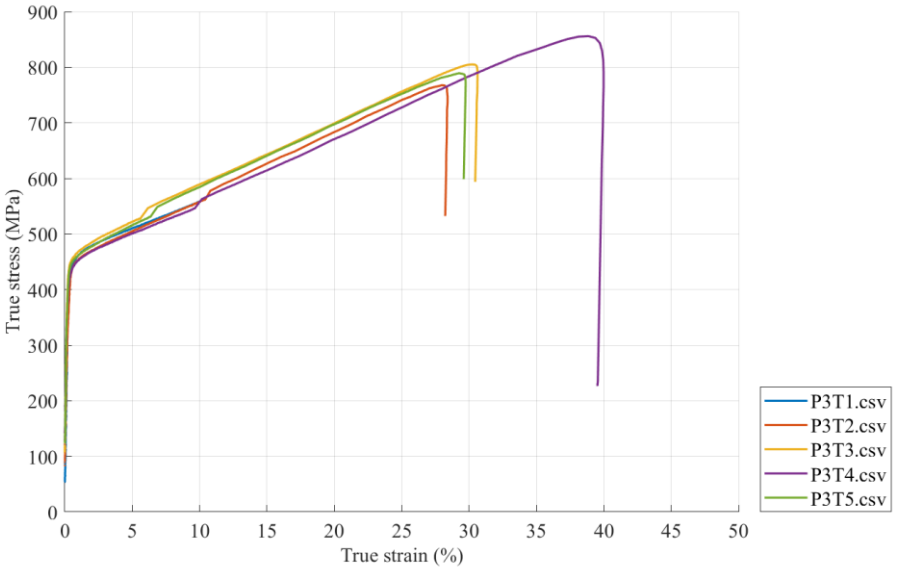

Figure 78: True stress-strain curves of WM for the five P3T specimens

The strain maps are presented in the following images (Figure 79 to Figure 81). Strain maps for the longitudinal specimens cut next to the FB in the base material side show typical behaviour of LAS. The strains are first localized in several locations on the specimen gauge length, and then localize into a single location prior to final fracture. The weld specimens show a markedly different behaviour. Most of the strains are localized early in the soft and ductile WM.

The strain maps are presented in the following images (Figure 79 to Figure 85). Strain maps in Figure 79 and Figure 80 for the longitudinal specimens cut next to the FB in the base material side show typical behaviour of SA508 LAS. The strains are first localized in several locations on the specimen gauge length and then localize into a single location prior to final fracture.

The weld specimens in Figure 81 to Figure 85 show a markedly different behaviour. Most of the strains are localized early in the softer and ductile Alloy 52 WM. Final fracture occurs in the middle of the WM section in all cases. Location of the virtual strain gauges is shown in the beginning of the test in Figure 81(a) and at the end of the test in Figure 85(b).

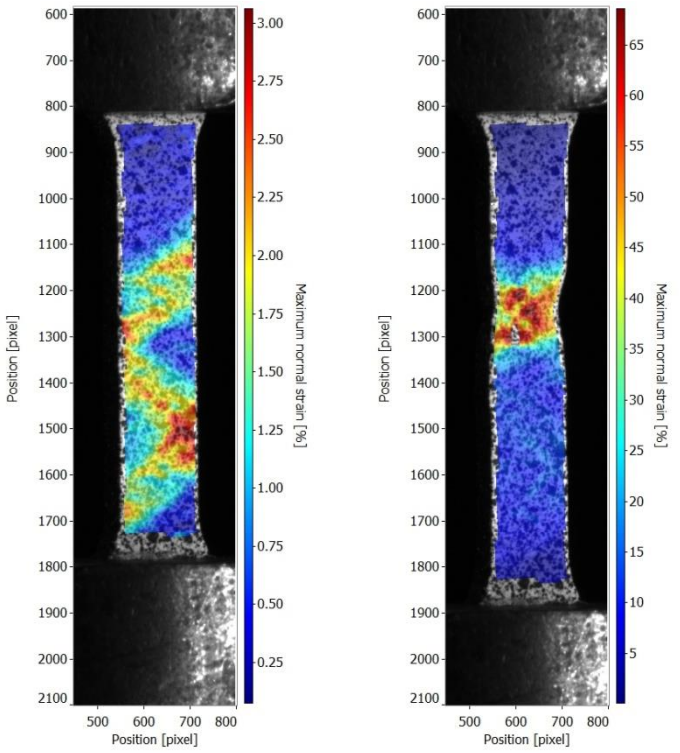

Figure 79: P3L3 - left: middle of test and right: prior to failure. Longitudinal specimen extracted from the HAZ. Specimen centre is 1 mm from FB.

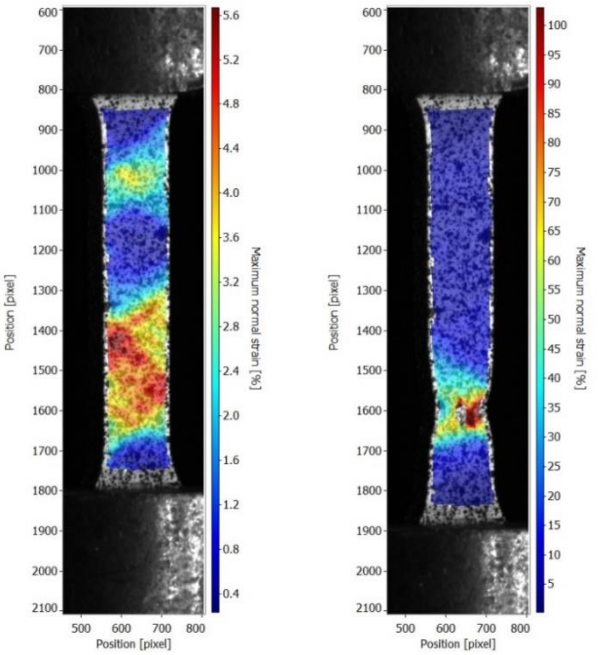

Figure 80: P3L33 - left: middle of test and right: prior to failure. Longitudinal specimen extracted from the HAZ. Specimen centre is 1.3 mm from FB.

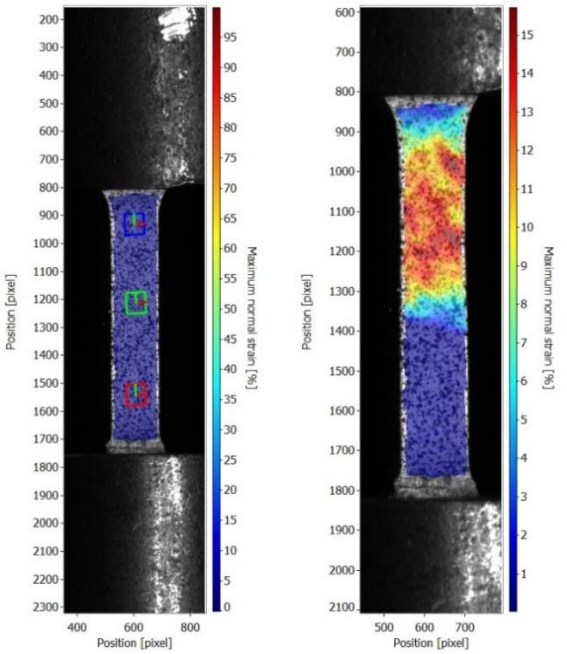

Figure 81. P3T1 (a) Virtual strain gauges shown in the beginning of the test. (b) Prior to interruption of the DIC measurement. Transversal specimen.

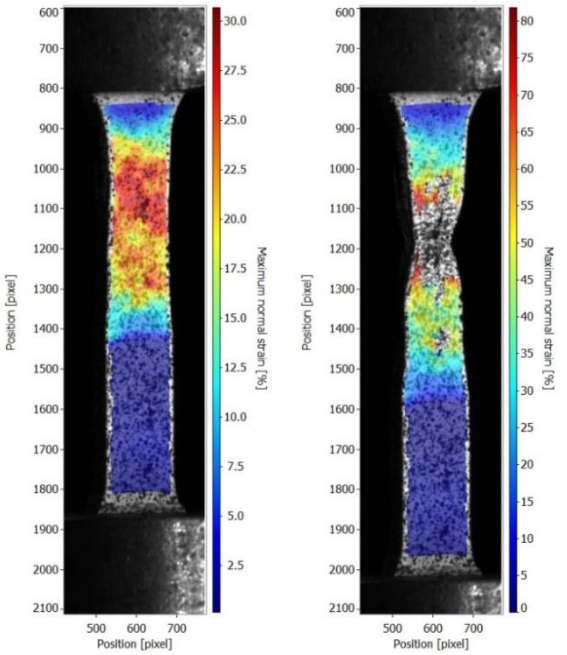

Figure 82. P3T2 (a) towards the end of the test, and (b) prior to failure. Transversal specimen.

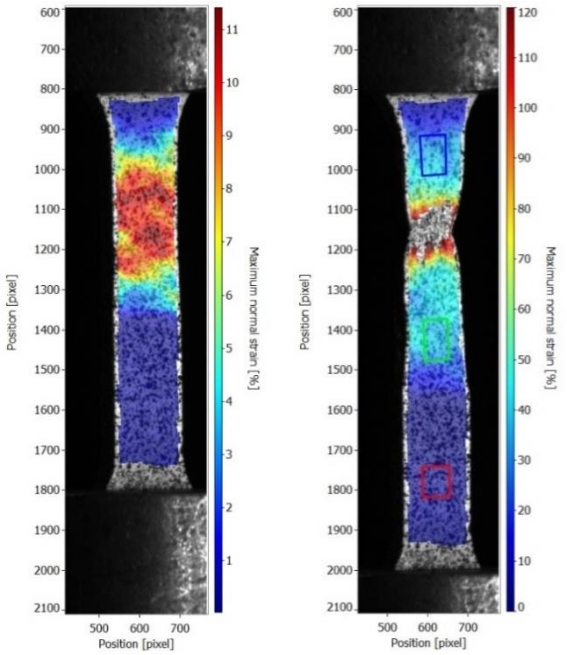

Figure 83: P3T3 - left: middle of test and right: prior to failure. Virtual strain gauges shown. Transversal specimen.

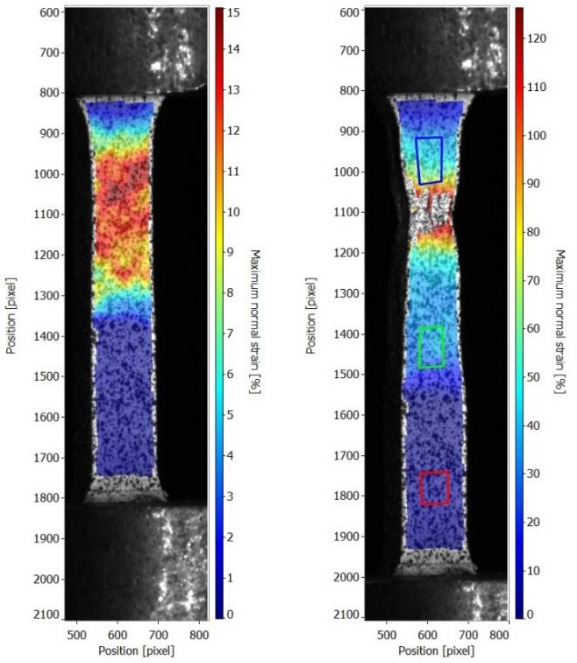

Figure 84. P3T4 (a) towards the end of the test, and (b) prior to failure. Virtual strain gauges shown. Transversal specimen.

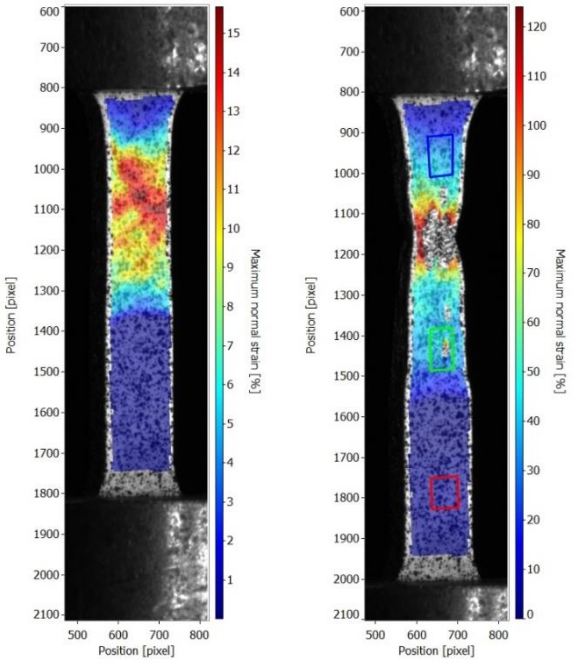

Figure 85. P3T5 (a) towards the end of the test, and (b) prior to failure. Virtual strain gauges shown. Transversal specimen.

High-temperature testing at 300 °C was performed for the longitudinal specimens, two with the specimen centre 1 mm from FB (P3L2, P3L3) and two with specimen centre 1.3 mm from FB (P3L32, P3L33). The engineering stress strain curves are shown in Figure 86. No big differences are observed in the stress strain behaviour 1 mm from FB. Compared to the room temperature results the strength is lower.

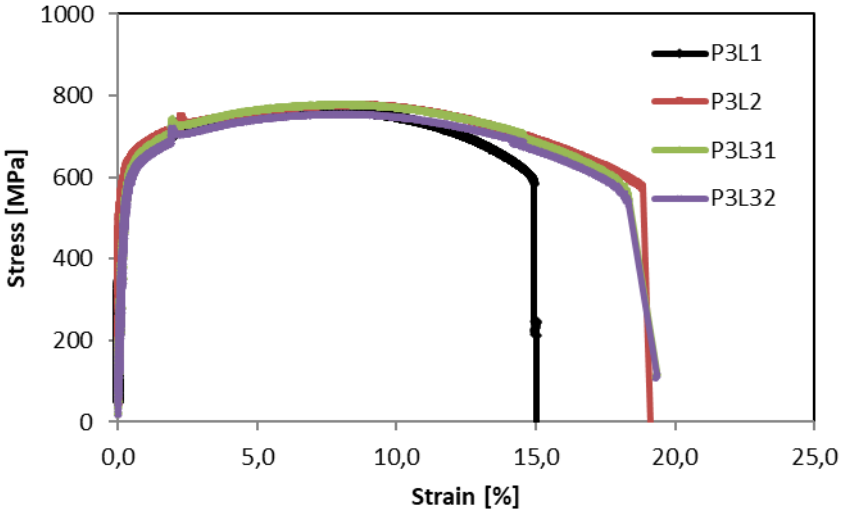

Figure 86. Engineering stress-strain data obtained at 300 °C.

4.3.2 J-R curves for Ringhals mock-up

The J-R curves of Ringhals mock-up with buttering are shown in Figure 87 and Figure 88. Stable crack growth by the ductile fracture mechanism is observed. Figure 87 shows the J-R curves for the HAZ cracks and Figure 88 shows the J-R curves for the Alloy 52 cracks. The crack locations given in the figures are nominal. Specimens with initial crack close to the FB, in the HAZ, resist crack growth less than the specimens with cracks in the HAZ, further away from the FB, or in the WM. The fracture toughness of the WM, Alloy 52, is higher compared to the HAZ.

The quality of the data was assessed according to ASTM E1820. The crack front straightness criterion is met. Also the predicted and measured crack lengths were within the limits. The maximum J capacity limit is exceeded approximately at 800 kJ/m^2. After exceeding the limit, the J-R curve is size dependent. After the limit is exceeded, the J-R curve becomes flatter compared to a bigger specimen.

Table 12 shows the J-R curve parameters. The cracks in the WM only blunt. For HAZ cracks, the applied fitting function describes the J-R curve after the blunting stage, approximately after 0.3 to 0.5 mm of crack growth.

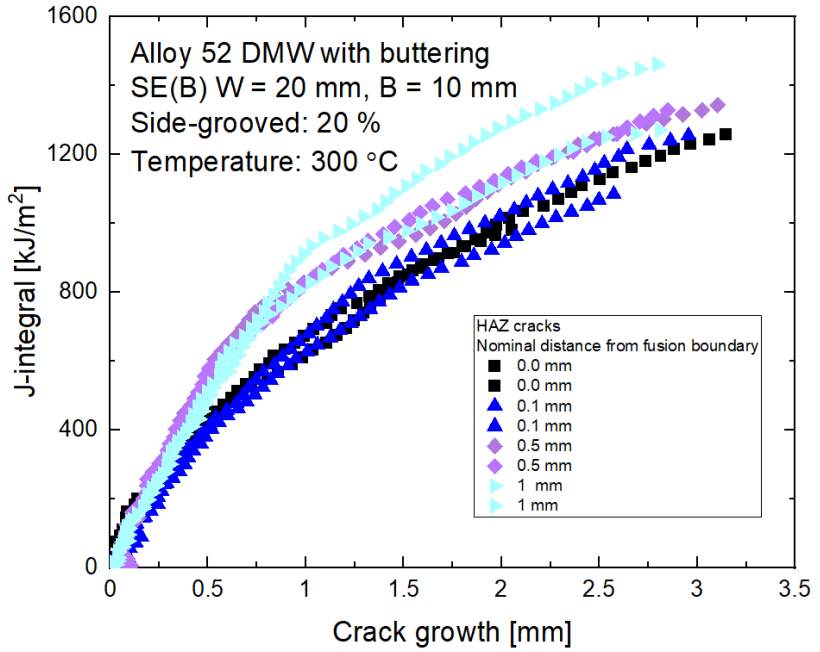

Figure 87. The J-R curves of Ringhals mock-up.

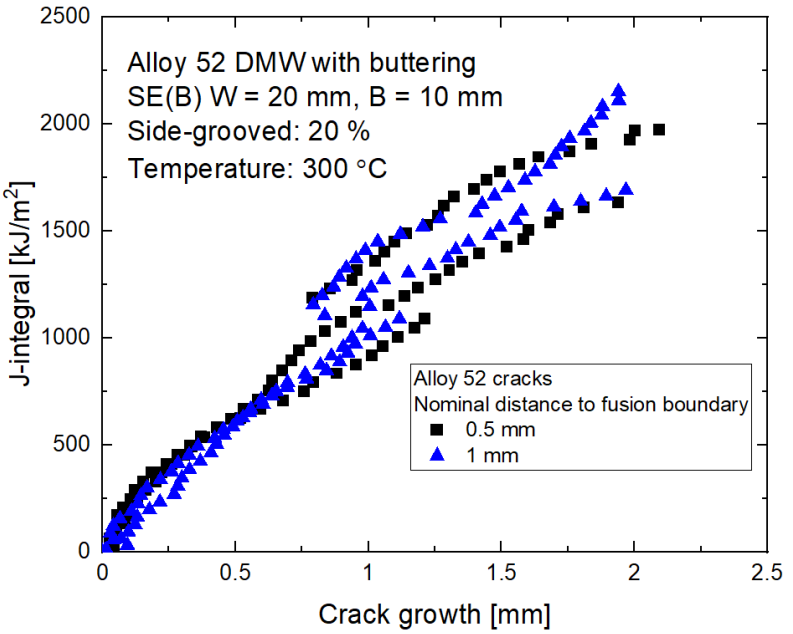

Figure 88. The J-R curves of Ringhals mock-up.

Table 12. J-R curve parameters for Ringhals DMW.

Nominal crack location	Specimen ID	$J = J_{1mm} \times \Delta a^m$		
		J_{1mm} [kJ/m^2]	m	J_Q [kJ/m^2]
HAZ 0 mm	P10A	636	0,636	459
HAZ 0 mm	P10B	666	0,578	521
HAZ 0.5 mm	P1-05A	820	0,439	772
HAZ 0.5 mm	P1-05B	805	0,503	738
HAZ 0.1 mm	P1-01A	614	0,638	431
HAZ 0.1 mm	P1-01B	685	0,584	681
HAZ 1 mm	P1-1A	814	0,459	760
HAZ 1 mm	P1-1B	905	0,487	896
Alloy 52 0.5 mm	P2+05A	1271	0,795	
Alloy 52 0.5 mm	P2+05B	1044	0,815	
Alloy 52 1 mm	P2+1A	1088	0,795	
Alloy 52 1 mm	P2+1B	1250	0,807	

Crack path analysis was carried out for selected J-R curve specimens of the Ringhals mock-up to obtain the actual crack location and path, with the details listed in Table 13. The cross-sectional images of the selected samples are shown in Figure 89 to Figure 91. The specimens were cut at the centre of the specimen.

The results show that the HAZ cracks deviate towards the FB, even from a distance of 900 µm. The nominal distances, distance between fatigue pre-crack tip and FB, are close to the actual measured distances. The crack appears to propagate along the FB but on the WM side. However, the fracture surfaces show that the HAZ crack propagate partly in the HAZ and the WM, see Figure 92, where both the oxides surface of the HAZ and the metallic surface of the WM can be seen on the fracture surface. WM cracks stay in the WM.

Table 13: Crack path analysis of fracture toughness specimens of the Ringhals mock-up.

Mock-up	**Test**	**Condition**	**Nominal location**	**specimen**	**Cutting direction**
Ringhals	J-R	ref	+0.1	P10A	Crack growth
Ringhals	J-R	ref	+0.5	P1+0.5A	Crack growth
Ringhals	J-R	ref	+1	P1+1B	Crack growth

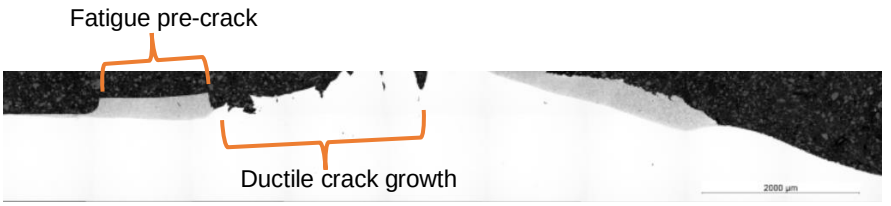

Figure 89. Crack path analysis of sample P10A along crack growth direction. Distance between the fatigue pre-crack tip and the FB is 200 µm.

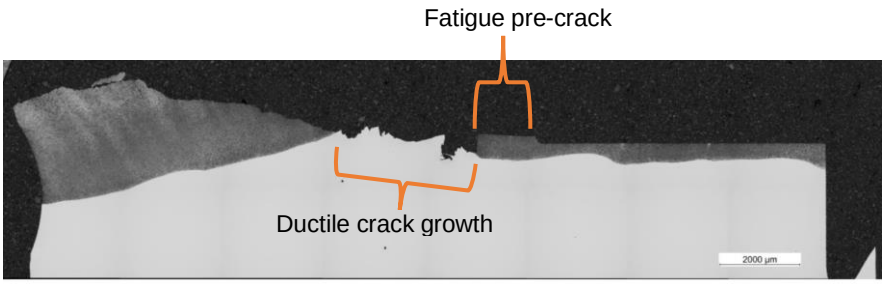

Figure 90. Crack path analysis of sample P1+0.5A along crack growth direction. Distance between the fatigue pre-crack tip and the FB is 400 µm.

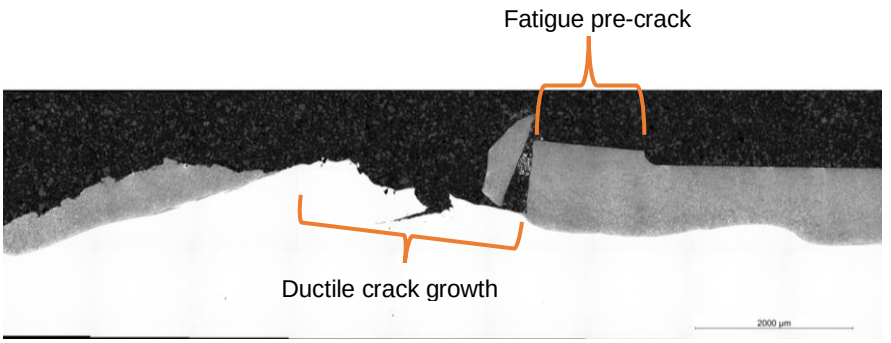

Figure 91. Crack path analysis of sample P1+1B along crack growth direction. Distance between the fatigue pre-crack tip and the FB is 900 µm.

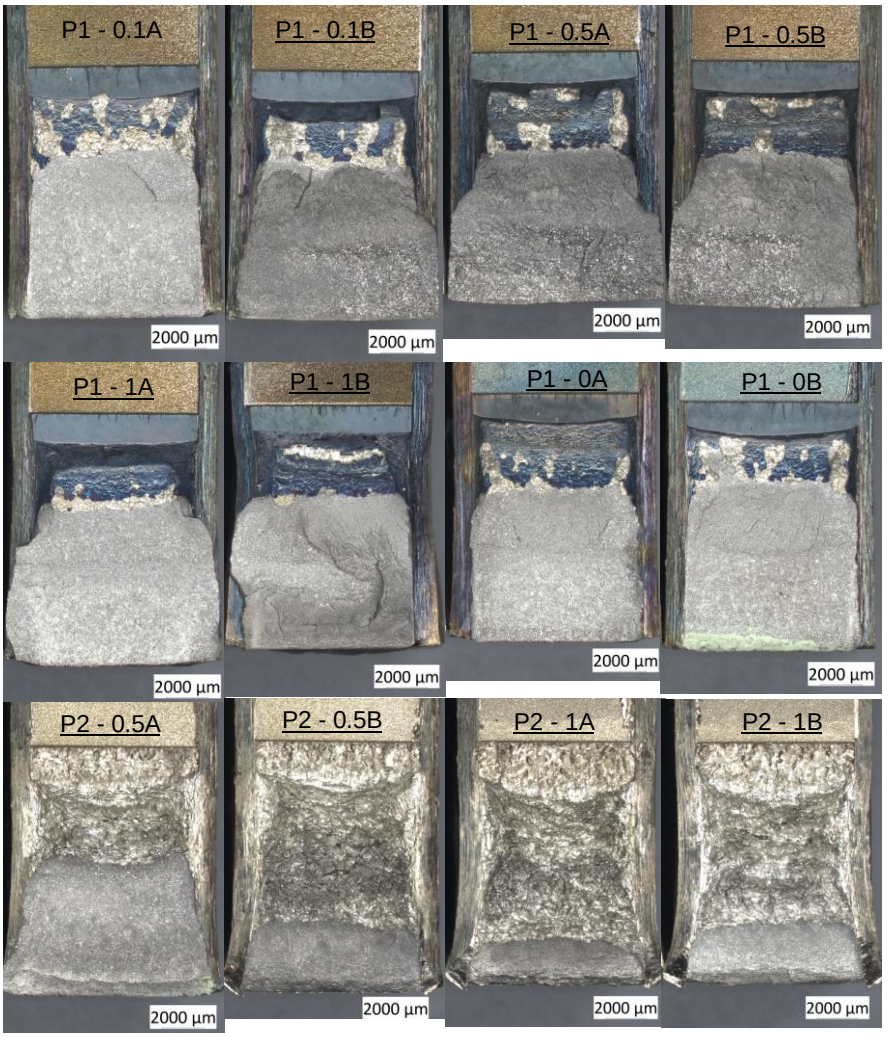

Figure 92. Fracture surfaces of the Ringhals specimens used for J-R curve testing.

4.3.3 Ductile-to-brittle transition testing

The fracture toughness in the DBT region was determined for the SA508/Alloy52 FB region for the Ringhals mock-up in non-aged PWHT condition. The fracture toughness testing was done according to ASTM E1921. The Ringhals mock-up has a pre-crack notch nominally placed both at the FB and 0.3 mm from the FB in the LAS HAZ, series FB and +0.3. The fracture toughness curves are shown in Figure 93. The Ringhals mock-up shows a dependence of toughness properties on the notch location; the T_0 is –117 °C and –176 °C with notch placed nominally at the FB

and at 0.3 mm from the FB in the HAZ, respectively. Two cracks are located slightly on the WM side, but brittle fracture initiation occurs on the LAS side after some ductile deformation. Three specimens of +0.3 series failed the crack straightness criteria.

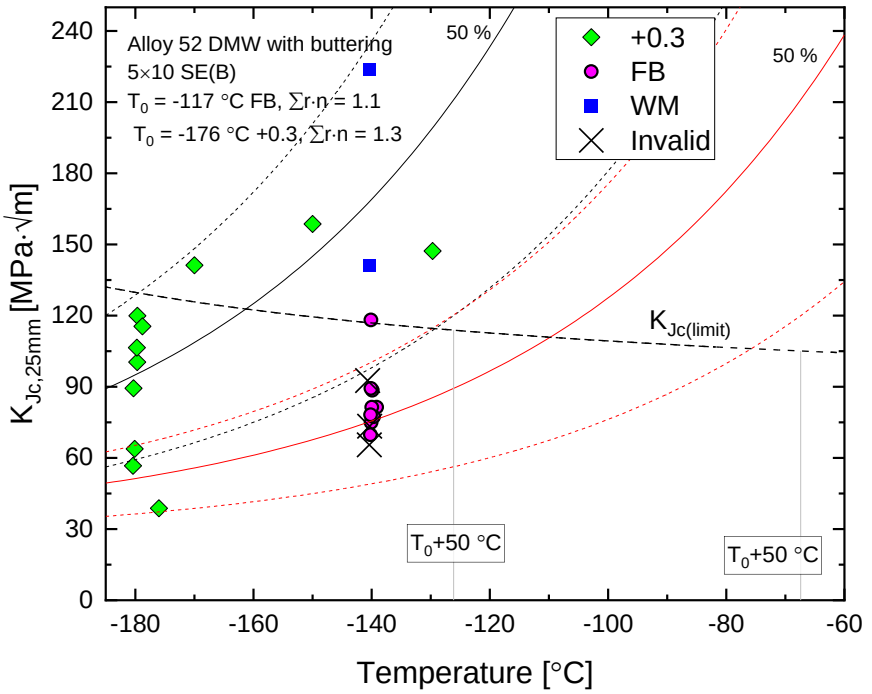

Figure 93. Fracture toughness results for (a) notch nominally at the FB and (b) notch nominally at the FB and at 0.3 mm from the FB.

A large variation in the toughness and cracking behaviour within the test series is seen in the Ringhals mock-up when the crack is located 0.3 mm from the FB, series +0.3. Part of the cracks deviate to the FB and the toughness is high. In other cases, the crack propagates along the original crack path, 0.3 mm from the FB in the LAS, and the toughness is lower.

In Figure 94, three types of fracture surfaces are shown of the fracture toughness specimens that was tested with crack nominally at the FB and at 0.3 mm from the FB in the HAZ. For series FB, when the crack is nominally at the FB (Figure 94(a)), the crack appears to propagate along the FB, especially if there are no major microstructural obstacles at the FB.

For series +0.3, three specimens result in lower fracture toughness values than the other specimens. Typical for the low results is that the crack does not deviate from the original crack path, Figure 97, similar to the TVO DMW. The fracture morphology appears to be rougher compared to the surface generated when the

crack progresses along the FB, *e.g.* compare to Figure 96 indicating that the crack would progress along a different path. Low-toughness specimens (Figure 94(c)) appear to have the crack propagating in the HAZ through the fracture path parallel to the FB without deviating from the pre-fatigue crack plane to the FB. For the results with higher fracture toughness, the crack deviates abruptly at initiation towards the FB, and the crack appears to follow the FB, Figure 99. The T_0 is −176 °C for series +0.3 when all results are accounted for. Few similar fracture surfaces with crack propagating in the HAZ parallel to the FB were observed in the TVO specimens as well.

For series FB, one result deviates from the rest of the population. Typical for the fracture toughness results closer to each other is that the crack is very close to the FB, and an abrupt deviation of the crack cannot be observed. In one instance the crack was partly in the WM and the LAS, Figure 95, and the fracture toughness did not differ from the results with the crack completely in the LAS but in direct contact with the FB. On the fracture surface, the bead structure can be seen, and the surface has moderate roughness, Figure 95 and Figure 96. The T_0 for series FB is −117 °C when the high toughness specimen is not included in the analyses.

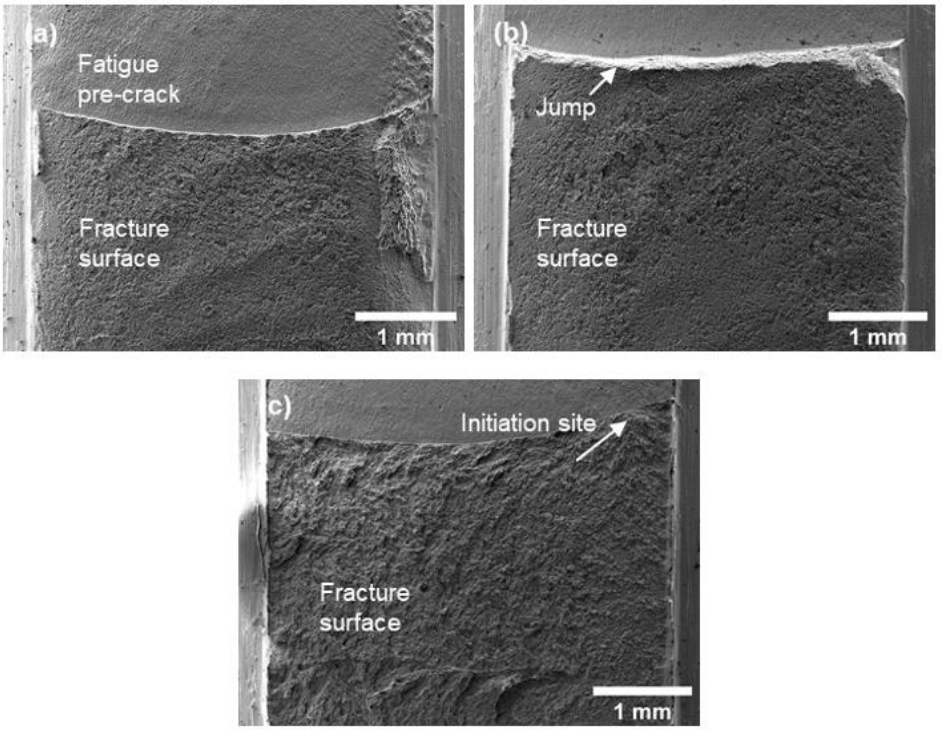

Figure 94. Fracture surfaces of the weld B with a) notch nominally at the FB, b) notch nominally at 0.3 mm from the FB with crack path deviates to FB, and c) notch nominally at 0.3 mm from the FB with crack propagates parallel to FB in the HAZ.

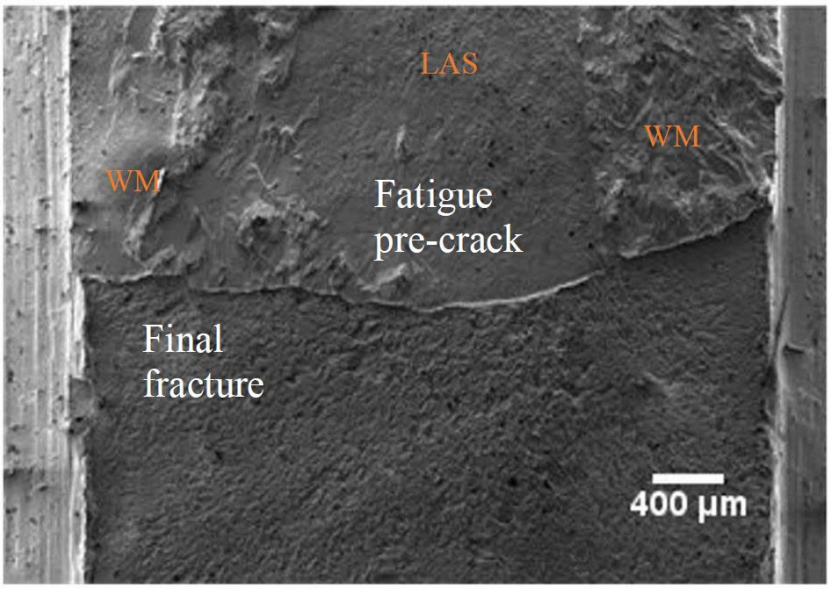

Figure 95. Series FB. Pre-crack in WM and LAS. Moderate toughness.

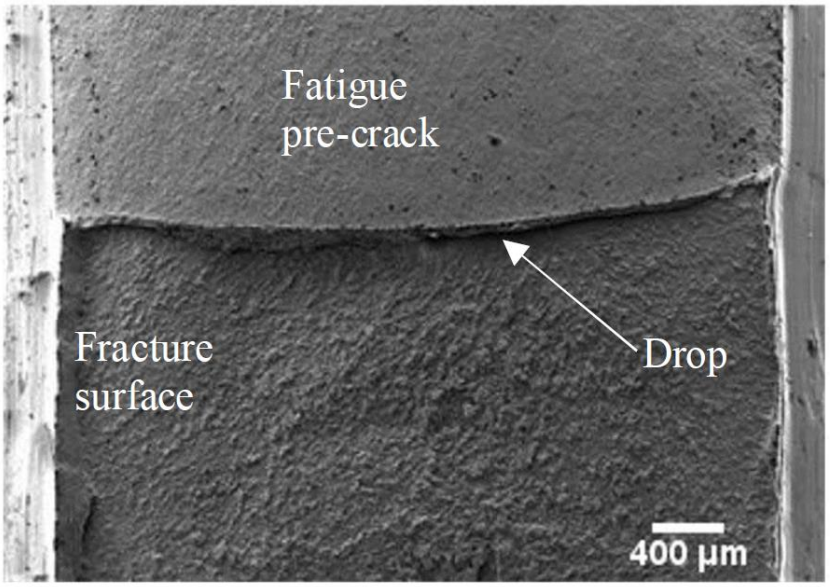

Figure 96. Series FB. High toughness.

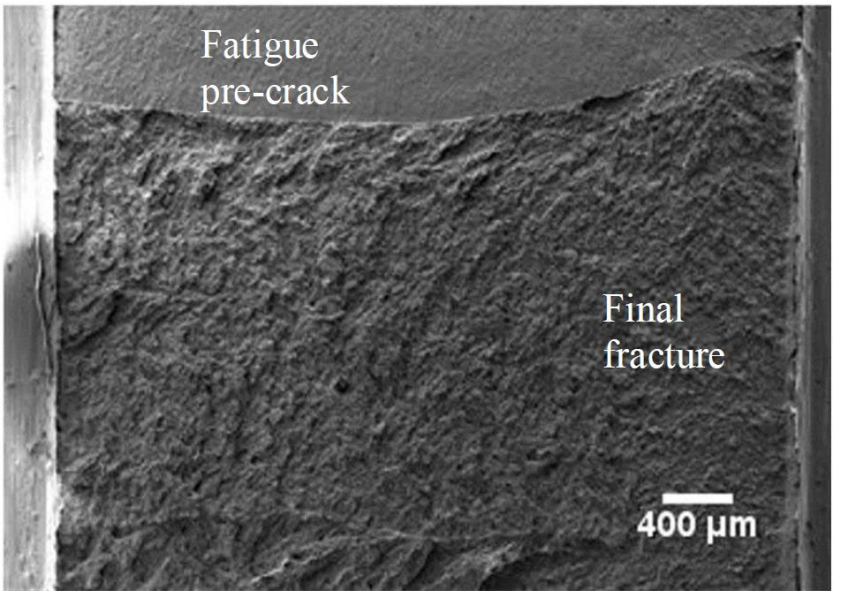

Figure 97. Series +0.3 mm. A low toughness specimen. The crack progresses on the same plane.

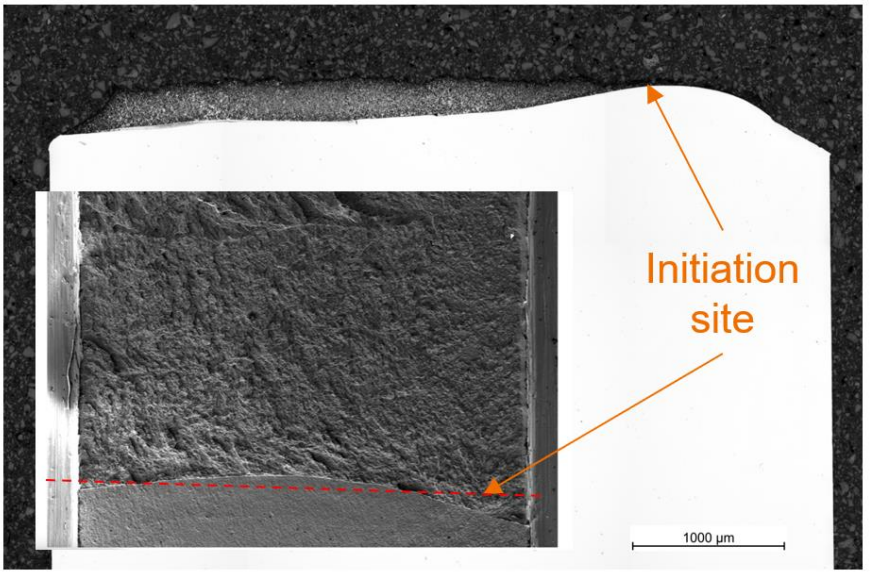

Figure 98. Same specimen as in the previous image. Series +0.3 mm. A low toughness specimen. The red line shows the location of the cross-cut of the specimen. Brittle fracture initiation occurs next to the FB but majority of the crack front is farther away from the FB in the HAZ.

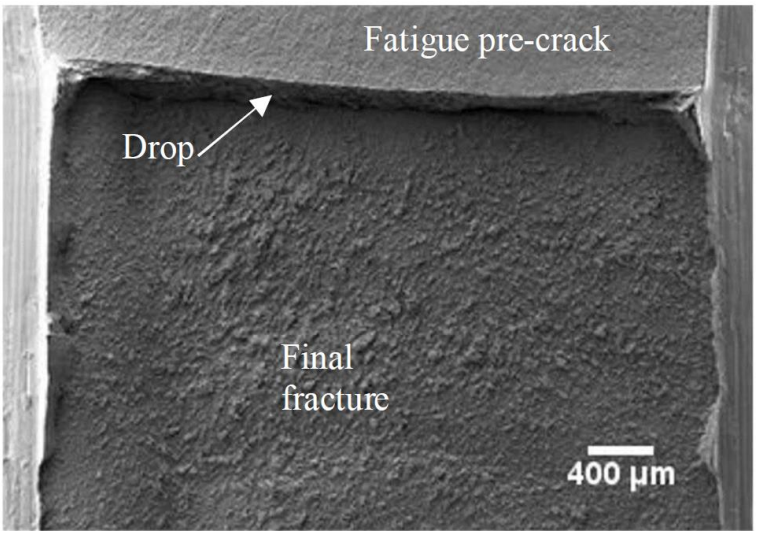

Figure 99. Series +0.3 mm. A moderate toughness specimen. The crack appears to deviate to the FB.

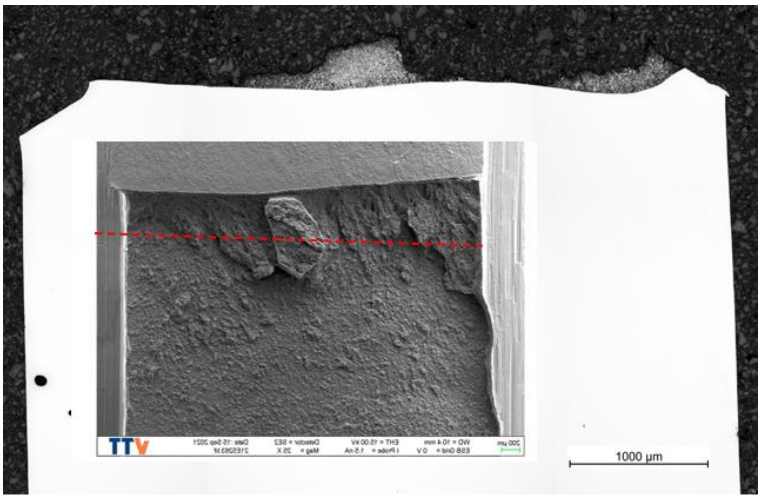

Figure 100. Series +0.3 mm. A high/moderate toughness specimen. The red line indicates the location for the cross-cut on the fracture surface. The cross-cut shows that the crack deviates towards the FB and propagates along the FB. Initially the fatigue pre-crack is located farther from the FB.

Cross-sectional studies of the fracture toughness specimen indicates that the local boundary area microstructure and notch locations strongly affect the fracture path and therefore the resulting fracture toughness properties. In Figure 101, the specimen with relatively low fracture toughness from Figure 94(c) have cracked propagating in the HAZ approximately 0.3 mm from the FB. At a closer look with

SEM of the horizontal cross-section specimen, in the region with fracture along the FB, no distinct microstructure at FB is observed whereas fracture at ~0.3 mm in the HAZ (see Figure 101), a PMZ microstructure is seen along the FB. Hence, the fracture path may deviate depending on the elemental dilution and microstructure at the FB.

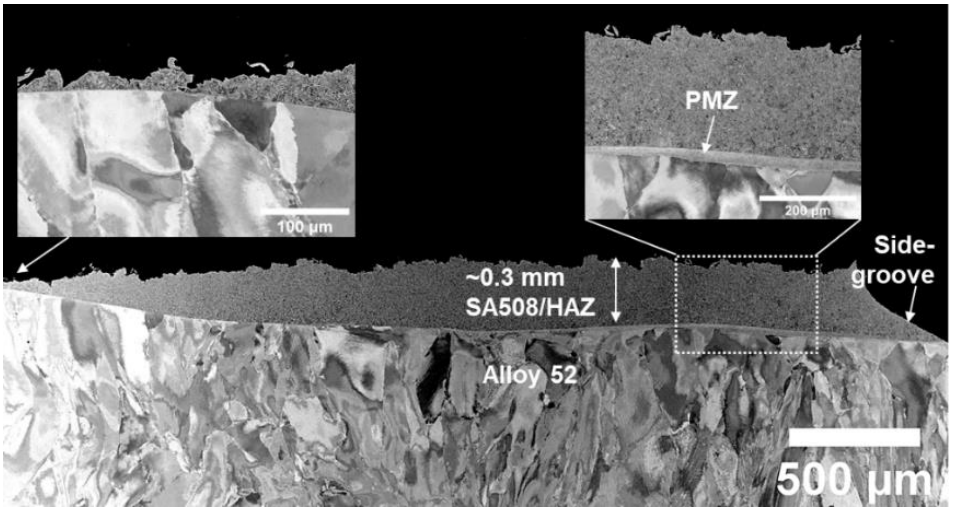

Figure 101. Horizontal cross-section of the fracture surface of Ringhals mock-up fracture toughness specimen with notch at 0.3 mm from the FB.

4.3.4 Macroscopic homogeneity screening of the T_0 data

The data sets were screened for macroscopically homogeneous material behaviour with two methods, one according to ASTM E1921, marked as screening 1, and the second based on the log-likelihood parameter, screening 2, giving the likelihood that the standard Master Curve cumulative distribution describes the data set. For the Ringhals DMW with buttering, both screening procedures indicate macroscopic homogeneity. The scatter in test series FB is quite low, and the log-likelihood is closer to the upper bound. The reason can be connected to the weak properties of the FB causing the initiation to occur on a specific plane instead of a volume ahead of the crack.

For the TVO NG mock-up, when all results are accounted for, screening 1 indicates homogeneous material behaviour whereas screening 2 indicates inhomogeneous behaviour. The crack location and path analyses show that four specimens differ from the general trend and the fracture toughness is lower. The crack location and path analyses indicate inhomogeneous material behaviour and validates the result of the screening method 2. The inhomogeneity screening results are shown in Table 14.

Table 14. Inhomogeneity screening. NG DMW = TVO, NG DMW with buttering = Ringhals.

Material	Series	T_0 [°C]	*Screening 1	*Screening 2
NG DMW	FB & +0.3	-129	Macroscopically **homogeneous** −127 °C step 5	Macroscopically **inhomogeneous** ln(L)/r = -5.7 Expected to be between -4.6 and -4.1
NG DMW with buttering	FB	-117	Macroscopically **homogeneous** −133 °C step 2	Macroscopically **homogeneous** ln(L)/r = -3.8 Expected to be between -4.5 and -3.8
NG DMW with buttering	+0.3	-176	Macroscopically **homogeneous** −178 °C step 2	Macroscopically **homogeneous** ln(L)/r = -4.6 Expected to be between -4.7 and -4.0

*Inhomogeneity screening

5 Discussion

5.1 TVO mock-up

5.1.1 Microstructure and carbides of TVO mock-up

The microstructure and carbides size distribution from different regions in LAS of the TVO NG AR and NG TA materials are shown in Chapter 3.2 and summarized in Table 15. At the FB, nanometre-sized precipitates were observed. In the NG TA material these are nano-carbides. However, in the NG AR material, the majority of the nano-precipitates at the FB (tens of nanometres wide zone) are nitrides whereas nano-carbides dominate in regions slightly further away from the FB. These nano-carbides at the FB of the NG TA material have a perfect Bargaryatskii's orientation relationship with the BCC matrix, which is reported for the first time in DMW, according to the knowledge of the authors. The orientation relationship between nanometre-sized carbides with the BCC matrix indicates that they precipitated directly on the crystal defects of ferrite matrix during PWHT.

Long-term thermal aging widens the width of the CPZ. In the CPZ, the number of carbides is much lower and the size of the carbides is also smaller in the AR material than in the TA material. This is in line with the result that the long-term thermal aging increases microhardness peak close to the FB. Except nano-sized nitrides /carbides at FB, the dominant carbides in the CPZ are $(Fe, Cr, Mn)_3C$ with a size about 50–100 nm. The CPZ contains the highest density of intergranular and intragranular $(Fe, Cr, Mn)_3C$ carbides in all regions in the LAS side. Even though $(Fe, Cr, Mn)_3C$ carbides also contain a small amount of Mo, Mo_2C carbides, the population is very low in the CPZ. It is interesting to note that Mo_2C carbides are frequently observed at the interface between the CPZ and the CDZ. These features of CPZ are common in both the AR and TA materials even when a wide CPZ was formed associated with a tempered martensite type FB. The columnar grains in the narrow CPZ are similar to the lath grains in the tempered martensite since they may be formed with the same mechanism resulting from high cooling rate at FB.

Long-term thermal aging slightly reduces the width of CDZ. This indicates a continuous diffusion of carbon from the WM to the HAZ during TA. The grain size is much smaller and the dislocation density is higher in the CPZ than in the CDZ. The

carbides population is the lowest in CDZ compared to CPZ and HAZ. Only small-sized Mo_2C carbides decorating mainly the grain boundaries can be found in the CDZ. Occasionally, few (Fe, Mn, Cr) M_3C carbides can be found at grain boundaries too. In the CDZ, (Fe, Mn, Cr)$_3$C carbides contain higher Mn content than Cr, which is different to the CPZ where (Fe, Cr, Mn)$_3$C were formed with higher Cr content than Mn.

The carbide density in the HAZ is evidently higher than in the CDZ but lower than in the CPZ. In the LAS HAZ, carbides were identified as (Fe, Mn, Cr)$_3$C and Mo_2C. Long-term thermal aging coarsens the carbides size in the HAZ, which corresponds well to the WAXS measurement in HAZ where higher percentage of carbides was observed in the TA than the AR material. In the HAZ there is a small fraction of carbide-free grains, which are formed likely during phase transformation where C partitioning occurred.

Table 15: Summary of grain size and carbides distribution in AR and TA materials.

		CPZ	**CDZ**	**HAZ**
Zone width	AR	≤500 nm	50 μm	N/A
	TA	≥1500 nm or ~11 μm (tempered martensite FB)	40 μm	N/A
Grain size	AR	100–300 nm	4.2 μm	1.2 μm
	TA	100–300 nm	4.0 μm	1.4 μm
Carbide type and size	AR	Nano-sized nitrides: ≤10 nm; (Fe, Cr, Mn)$_3$C: ≤100 nm	Mo_2C: ≤40 nm; (Fe, Mn, Cr)$_3$C: ≤150 nm	(Fe, Mn, Cr)$_3$C: ≤300 nm; Mo_2C: ≤100 nm
	TA	Nano-sized carbides: ≤20 nm; (Fe, Cr, Mn)$_3$C: ≤200 nm	Mo_2C: ≤80 nm; (Fe, Mn, Cr)$_3$C: ≤150 nm	(Fe, Mn, Cr)$_3$C: ≤2 μm (fibre) or ≤300 nm (round); Mo_2C: ≤100 nm
Carbide density	AR	Higher than in HAZ	Much lower than in HAZ	Similar to normal reactor pressure vessel steel
	TA	Higher than AR	Similar to AR	Higher than AR

The welding techniques (*e.g.* NG or buttering) have a significant effect on the solidification, cooling rate, internal stresses and mixing of metals, impacting the forming solidification microstructure and carbides at the FB in a DMW [74]. The microstructure and carbides in the FB and HAZ regions have a direct influence on the local brittle fracture behaviour and cracking susceptibility of a DMW [8]. During long-term thermal aging in the NG mock-up, more carbon in the LAS side can diffuse

from the CDZ to the FB [36]. As shown in this work, long-term thermal aging leads to moderate changes in the microstructure and carbides in the FB and HAZ regions in NG DMW. The peak hardness for the NG DMW coincides well with the position of carbon peak value [7] [29]. After thermal aging, the higher microhardness mismatch at the FB, the larger/denser carbides in CPZ and the coarsened carbides and local carbide-free grains in HAZ may lead to local brittle zone and may even cause very low fracture toughness [75]. Nevasmaa *et al.* [76] reported that a decrease in fracture resistance was concluded to stem from increased metallurgical constraint and crack (growth) driving force accentuated by the high, local mismatch state, coupled with inherent local inhomogeneity of the near-interface regions. Under high local strength mismatch, the inherent strength and toughness properties of two neighbouring, mismatching microstructures become increasingly important, which may, in some cases, dictate the entire fracture behaviour of a DMW.

In majority of the DMW literatures, the carbides were referred to as chromium carbide precipitates without detailed information of the chemistry and crystal structure [77]. Choi [25] reported that $Cr_{23}C_6$ precipitated at the FB immediately after DMW welding and the number of $Cr_{23}C_6$ precipitates in the FB regions increased after thermal aging for 1713 h at 400 °C. However, the number of precipitates decreased by the coarsening and coalescence of precipitates with a thermal aging of 3427 h. In this paper, thermal aging at 400 °C for 15 000 h results in both the number increase and coarsening of precipitates at FB, CPZ and HAZ. This will result in the increase of contact surface between the LAS (anode) and Cr-rich precipitates (cathode) and then cause the increase of the corrosion rate if the DMW is exposed to high-temperature oxidizing water. In the present study the dominant carbides are M_3C θ carbides (verified by index under multiple zone axes), $M_{23}C_6$ was not detected in any of our TEM samples. One possible reason is that the chemical composition, cooling rate, temperature gradient and PWHT affect the FB carbides type. Another reason may be due to the similarity of a few high index zone axes in electron diffraction patterns with the minor differences in closed pack plane distance between BCC and FCC lattice at FB, which may have caused mis-indexation in literatures.

The APT results suggests that no significant P segregation was observed. However, the APT measurements were only done on a few specimens within HAZ grains. Though a higher amount of grain boundary cracking has been seen in mechanical tested thermally aged samples, which can be assumed to be due to P-segregation, the amount could be small, as is the shift in T_0.

5.1.2 Fracture mechanical behaviour of TVO mock-up

The effect of thermal aging at 400 °C up to 15 000 h on DBT region was investigated for the TVO mock-up, and the results are reported in Chapter 4.2. The cracks and the notches were placed close to the FB between the LAS and the WM. Fracture toughness testing and instrumented impact toughness testing were performed according to ASTM E1921 and EN ISO 148-1, respectively. The T_0 reference temperature does not change significantly with aging time, but the shift in T_{28J}

transition temperature is 49 °C after 15 000 h and appears to saturate after 10 000 h. The shift in reference temperature for crack arrest toughness, T_{Kla}, is 35 °C. The results indicate that the aging mechanism affects more the crack propagation and arrest properties than brittle fracture initiation.

5.1.2.1 Shifts in fracture toughness and impact toughness

Figure 102 shows the difference in the shifts for crack location corrected T_0 and impact toughness based T_{28J} and T_{41J}. The shift after thermal aging at 400 °C for 15 000 h is 51 °C based on the impact toughness testing and 10 °C based on fracture toughness testing. The effect of aging on the shift in impact toughness appears to saturate after 10 000 h of thermal aging. The T_0 shift is of the same order as the standard deviation of the T_0 estimate, but the crack location corrected T_0 values for the aged conditions are systematically above the reference condition. In conclusion, the effect of thermal aging on T_0 is marginal.

The different shifts from the impact toughness and fracture toughness testing can be explained by the nature of the test methods. The fracture toughness describes the stress intensity required to initiate brittle fracture in the DBTT region, whereas the impact toughness describes the energy required to initiate, propagate and arrest a crack. Additionally, the fracture toughness specimens are more sensitive for crack/notch location relative to the FB in the HAZ compared to impact toughness specimens since the fracture process zone of an impact toughness specimen samples a larger region [73]. However, the results show that if part of the notch of the impact toughness specimens is in the WM, the impact toughness increases significantly, and the applied crack location correction procedure reduces this difference.

Impact toughness and fracture toughness can be affected differently by the aging mechanism. The assumed main thermal aging mechanism is P segregation. Due to thermal aging, the P content increases on the grain boundaries leading to a shift in transition temperature and sometimes to an increase in intergranular fracture [54]. Previously, for the same DMW [36], the fraction of intergranular fracture increases on the fracture surface as a function of aging time were observed. P segregation to grain boundaries can mechanistically affect more the crack propagation and arrest properties than crack initiation.

The impact toughness testing was done with an instrumented impact hammer enabling characterization of the effect of aging on the crack arrest transition temperature, T_{Kla}, estimated based on

$$T_{Kla} = T_{Fa4kN} + 11.4\,[°C] \pm \sigma = 12.0\,°C \tag{12}$$

Figure 103 shows that the crack arrest transition temperature increases with 35 °C after aging at 400 °C for 15 000 h, which is 15–16 °C smaller than the shift in T_{28J} or T_{41J}.

Based on the results, thermal ageing appears to affect more the crack arrest properties of the FB region than the brittle fracture initiation properties. A similar

result is observed in [78] where a reactor pressure vessel LAS of a hydrotreating reactor in an oil refinery operated at 400 °C for 17 years shows a 60–70 °C shift in impact toughness, whereas the T_0 remains practically unchanged.

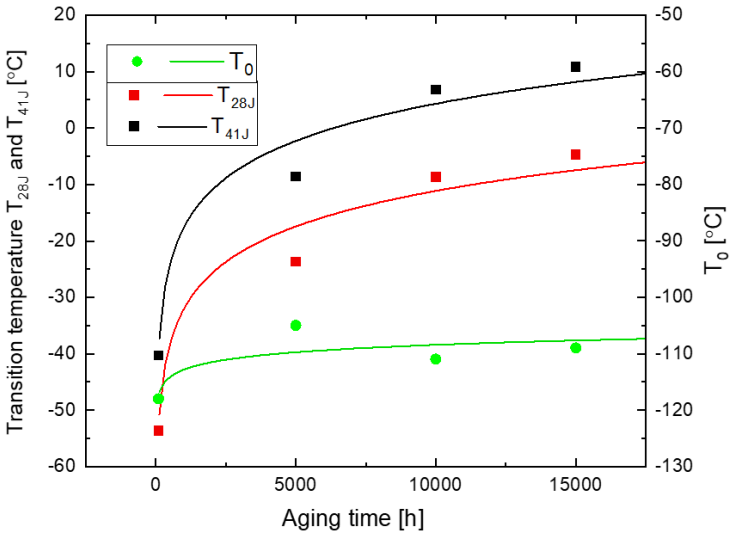

Figure 102. Effect of aging time at 400 °C on transition temperature.

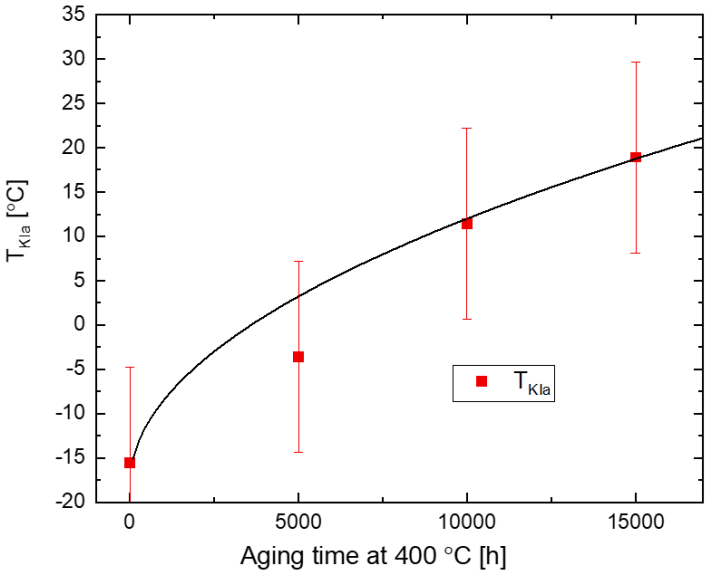

Figure 103. Shift in arrest transition temperature T_{KIa}. A common uncertainty, 2σ = 10.8 °C, for the different conditions was calculated based on the upper part of the transition curve. The transition curves are presented in Figure 73.

5.1.2.2 T_0 and T_{28J} dependence

In [79], Kocak *et al.* give a generic dependence for T_0 and T_{28J}, $T_0 = T_{28J} - 18$ °C, with a standard deviation of 15 °C. The assessment in [73] shows that the dependence is applicable for C(T) specimens, but the standard deviation is 22.5 °C. And the same correlation for SE(B) specimens is an offset of 10 °C due to the constraint effect.

Figure 104 shows that the T_0 and T_{28J} values obtained from this study are closer to the lower part of the 2σ scatter band already in the reference condition. The difference to the general dependence grows as the material ages since aging affects more T_{28J}. The $T_0 = T_{28J} - 28$ °C dependence gives a conservative estimate of the T_0 values. The cause for the difference could be in the future investigated through comparative material simulations of impact and fracture toughness specimens with the crack/notch at a soft/hard interface. The aim would be to compare how the softer WM affects the stress fields ahead of the crack in the different specimens and under different loading rates.

Structural integrity codes (API, ASME, BS 7910, R6, SINTAP/FITNET) allow the DBT toughness assessment to be done directly or indirectly using T_0, or impact toughness-based transition temperature estimate. The results from this study underline the mechanistic differences in these two methods yielding different DBTT shifts due to aging. The T_0 reference temperature describes more precisely the brittle fracture initiation process, and the resulting Master Curve is directly applicable without the need for conversion. For the investigated material, the impact toughness-based transition temperature gives a more conservative estimate of the DBTT. In this case, impact toughness testing can be applied to get a first estimate of the DBTT, if better precision is needed fracture toughness testing is recommended.

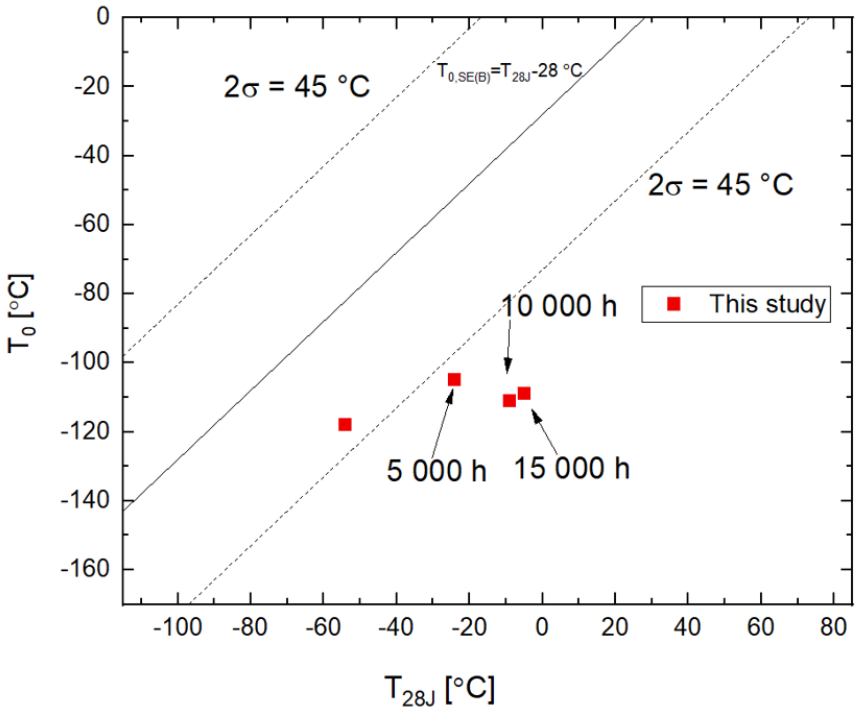

Figure 104. Correlation between impact toughness based T_{28J} and fracture toughness based T_0.

5.1.2.3 Comparing the DBTT shifts to similar materials

In this study, the shift in T_0 is marginal. In [13] and [80], Joly *et al.* investigated a similar Alloy 52 DMW. The material was aged for 10 000 h at 400 °C and for 50 000 h at 350 °C. The shift in T_0 is higher compared to this study, ΔT_0 is approximately 30 °C in both cases, and the absolute T_0 values are lower, see Table 16 and Figure 105. From chemical perspective the materials are similar. The P content differs slightly (Table 16), but not significantly according to previous investigations [54].

One important reason for the difference in fracture toughness behaviour is the PWHT. The PWHTs differ between the two DMWs. The PWHT of mock-up investigated in [13] and [80] lasted 6+10 h at 600 °C, compared to 14.8 h at 550 °C and 7.7 h at 610 °C for the DMW from this study. Consequently, the CDZ is reported to be 50 µm wider in [13] and [80]. The PWHT in [13] and [80] was optimized to enhance the effect of thermal ageing on the transition temperature shift.

The fracture toughness can also be affected by the crack location and specimen size. Compared to this study, the average crack location was farther from the FB closer to the grain-refined region. In [60], Joly *et al.* reported a larger shift in DBTT in the grain-refined region than in the grain-coarsening region of the HAZ of a

18MND5 LAS (similar to SA 533). Noticeably, for the investigated DMW after 15 000 h of aging, a lower fracture toughness is measured at 0.3 mm from the FB when the crack no longer deviates to the FB, as explained in Chapter 4.2. Yet, the observation cannot be connected to be due to thermal aging, since there is no reference data for that region.

For the investigated material, as long as the crack deviates to the FB, the fracture toughness increases with the distance of the crack location to the FB, which can explain the difference in the absolute T_0 values between the two DMWs. Though, in [13] and [80], similar crack path behaviour is not reported. Future investigations could focus on better understanding the fracture path and aging behaviour farther from the FB and specimen size effects. In this study, the fracture toughness was measured with smaller specimens, see Table 16. A larger specimen with a larger process zone is more affected by the softer WM and not necessary as affected by the local microstructural regions.

Table 16. Comparison of two similar DMWs.

	DMW from this study	DMW from [13] and [80]
Shift in T_0 [°C]	10	27
T_0 in non-aged condition [°C]	–118	–153
Average distance of the crack to the FB	≈ 0.1 mm	≈ 0.3 mm
Crack propagation	Deviates to the FB and grows along the FB	No evident jumps
Chemistry	Ni = 0.71%, Mn 1.44%, P = 0.005%	Ni = 0.71%, Mn 1.46%, P = 0.007%
PWHT	14.8 h at 550 °C and 7.7 h at 610 °C	6+10 h at 600 °C
Size of the CDZ	100 µm	150 µm
Microstructural location of the crack	In average, the cracks are in the CDZ	Less than 150 µm in average from the CDZ
Specimen	5x10 SE(B)	1T C(T)

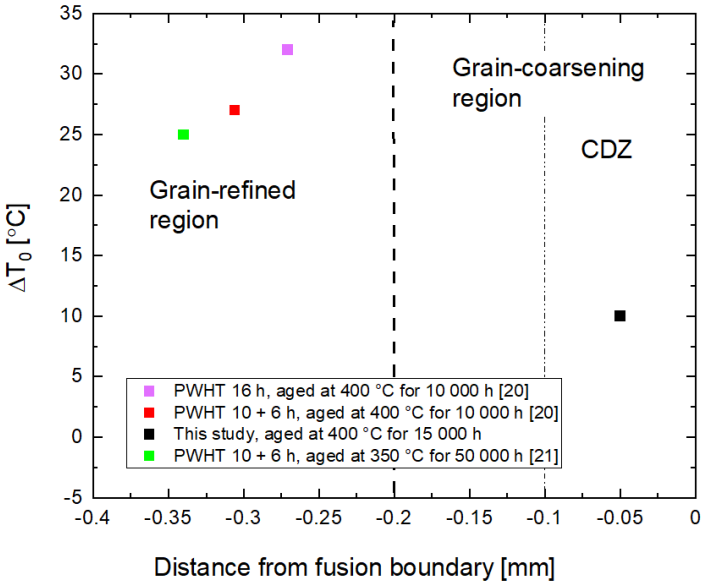

Figure 105. Shifts in ΔT_0 as function of distance to FB for two different Alloy 52 DMWs. [13] [80]

Figure 106 compares impact toughness-based transition temperature shifts due to thermal aging at 400 °C for the Alloy 52 DMW from this study, a 533 BM, a coarse-grained HAZ (CGHAZ) of SA 508 class 3 RPV weldment and a simulated CGHAZ of SA 508. The 533 BM is similar to the SA 508 LAS. Compared to the BM, the shifts for the DMW are more than 30 °C higher after 10 000 h aging. The grain size and the P content is smaller in the CDZ of the DMW than for the 533 BM, see Table 17. A significant difference between the BM and the DMW is the PWHT and the heating during welding.

The transition temperature shift for the DMW is similar to the CGHAZ of SA 508. In both instances, the shift saturates. The notches of the DMW are also located in the CGHAZ. Table 17 summarizes key parameters for the materials affecting the sensitivity to thermal aging. The bulk P content is slightly smaller for the DMW, and the grain size also, typically decreasing the sensitivity to thermal aging but not making a significant difference in this case.

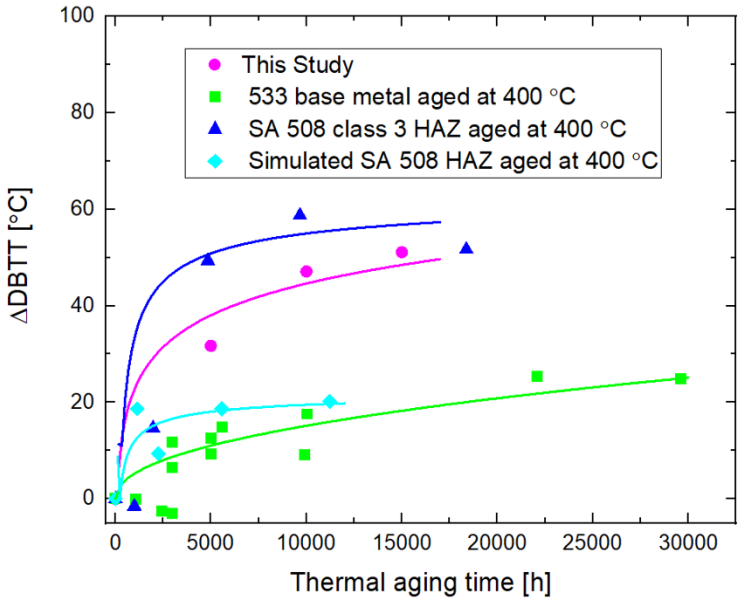

Figure 106. DBTT shifts for 533 BM, SA508 HAZ of a similar metal weld and HAZ of the DMW from this study.

Table 17. Key parameters affecting thermal aging. The effect of welding parameters and PWHT on thermal embrittlement could not be analysed.

	CDZ of the DMW	533 BM	GC HAZ of a WM	Simulated CG HAZ
Material	BM is SA 508	SA 533	SA 508	SA 508
P %	0.002 for BM and 0.005 for WM	0.005–0.012	0.006 for BM and 0.019 for WM	0.007
Ni %	0.77 for BM and 59 for WM	0.6–0.7	0.8	0.75
Grain size [um]	2.5 close to the FB	4–22 µm	22, typical for RPVs	125

5.2 Ringhals mock-up

5.2.1 Fusion boundary microstructure of Ringhals mock-up

The Ringhals DMW with double-sided buttering and a V-groove weld between the bainitic LAS and austenitic stainless steel safe-end was investigated with the focus on the FB of the SA508 LAS/Alloy 52 buttering. The FB was divided into three distinct types based on variations in microstructure and width, *i.e.*, narrow FB (~80–

85% of whole FB), tempered martensitic transition region (~15%) and wide PMZ (~1–2%). The studied FBs can be divided into three types based on the microstructural features and the width of the transition zone. The different FB types were induced by the local heat flow and respective elementary diffusion, which significantly influence the hardness mismatch locally across the DMW interface. The correlation between FB type, microstructure, elemental diffusion, crystal structure, hardness and local heat input was reported in Chapter 3.3.

The characteristics of the different FB types were analysed, focusing on the metallurgical and mechanical mismatch. The welding parameters have a significant effect on the solidification, cooling rate, internal stresses and mixing of metals, impacting the forming solidification microstructure at the FB. The orientation of the buttering weld is perpendicular to the typical V-groove or NG weld. During the multi-pass welding, a low local heat input can normally improve the toughness properties by decreasing the cooling rate and minimizing the HAZ grain coarsening [74]. Furthermore, the subsequent beads may have a slight chemical compositional change in *e.g.* C or Cr contents compared to the first beads at the interface as the weld pool mixes with matrix by forming *e.g.* swirls and dilution zones, which cause some variation in the forming FB microstructure.

The three types of FB microstructures were found to associate with the different FB widths, chemical dilution and the width of the CDZ and carbide density in the LAS HAZ, indicating a different local heat flow and cooling profile. Type-B boundary occupied around 15% of the whole analysed FB whereas 1–2% of the FB was categorized as the type-C boundary. The type-B FB may be a result from re-melting of metals during multi-pass welding and rapid cooling to form martensite microstructure which has been tempered by subsequent weld beads. Furthermore, the ~10 µm low nano-hardness in Alloy 52 buttering can be explained by a relatively high local heat input and the resulted carbon diffusion across the transition zone. In the nanoindentation measurements, the type-B FB with tempered martensite phase showed a peak in nano-hardness whereas no such significant peak was seen at the type-C PMZ. The nano-hardness peak associated with the hardened microstructure, *i.e.*, tempered martensite, results in a stronger strength mismatch between the weld and LAS than in the type-C FB. The PMZ is distinct in the indentation map in Figure 30(c), however, the absence of an evident nano-hardness peak in Figure 30(d) and the nearly constant chemical composition of alloying elements at the PMZ relates to a stronger mixing of materials and a different solidification structure with lower cooling rate compared to the type-B FB. Similar microstructure to the type-C PMZ is often seen in swirls that are formed during welding when turbulent weld pool enters the base material and a partially melted metal solidifies. In the investigated buttering weld, the welding orientation and technique inhibit effectively the swirl formation.

A high local heat input, *e.g.* at the location between two weld beads, results into higher Gibbs free energy, stronger elemental diffusion and dilution between the buttering weld and the LAS [10], which was consistent with the results in this work. Moreover, ~30 µm lower-bound nano-hardness in the LAS CDZ was observed in type-C FB but not in type-B FB, revealing the effect of annealing and stress relief

by the buttering process on the LAS side and that higher internal stresses are left in the LAS side in the tempered martensitic FB. The division between tempered martensite and PMZ is supported by the EBSD analysis and the EDS line scan, where the mixing of BCC and FCC phases and chemical compositions in the PMZ is relatively more significant compared to the type-B FB. Similar elemental dilution curves have been reported by Hou *et al.* [35] and Wang *et al.* [81]. The relatively high C content in the LAS side lowers the starting temperature of martensite transformation. The local heat input and rapid cooling rate together with carbide precipitations at the FB create a favourable system for a diffusion-less process of martensite formation [21]. The carbon migration from the LAS to the weld side and dissolution of primary carbides enhances the carbon equivalent near the interface at high austenitizing temperatures, enhancing hardenability and martensite formation [11]. Chen *et al.* reported that a gradual change of the alloy elements' contents across the FB may result in the formation of martensite at the FB whereas a sharp change will not lead to martensite formation [82]. There is a K–S orientation relationship between the WM and the formed martensite [82]. The formation of the martensite was mainly controlled by the diffusion of the alloy elements and the residual stress result from welding [28]. Martensite typically is determined having a BCT crystal structure, but the tetragonality is obviously lost in this study due to tempering at a sufficient C-content. The XRD analysis of the crystallography of tempered martensite FB showed a BCC structure. Below 0.18 wt% C content in the FB, tempered martensite is reported to have a cubic crystal structure, which is confirmed experimentally by Liu *et al.* [83] , and is in agreement with the current observation. Moreover, all bands in type-B FB Kikuchi pattern were diffused compared to the sharp Kikuchi bands in the LAS metal matrix, which indicates a lower band contrast or coincidence index value due to distortion at the type-B FB. This also correlates with high residual strains and high density of dislocations in the tempered martensite phase.

Martensite at the FB has been reported to link with the formation of type-II boundaries, which are known to be prone to cracking or FB debonding [84]. The evolution of type-II boundary that is parallel to the FB is reported as a consequence of the allotropic transformation in the BM [23]. Wang *et al.* studied a buttered and a V-groove DMW microstructure and fracture behaviour from the interfaces of SA508/Alloy 52 [8] [27]. Due to a high heat input, at the base material/weld interface, larger area of lath martensite was observed and relatively significant type-I boundary and type-II boundaries in the weld side adjacent to the interface were found [8] [27]. The type-II boundary has been observed in both buttering and NG welds, correlating with the evolution of the weld pass structure [29] [21]. Ming *et al.* also reported that high heat input and long high temperature duration welding process can promote the element diffusion, grain boundary migration, type-I and type-II boundaries formation and thus a wider CDZ and deteriorated cracking resistance [12]. In the present study, however, no type-II boundaries and only negligible number of type-I boundaries were found in the buttering weld side, even along the tempered martensitic FBs. The absence of type-II boundaries reduces the

risk of SCC or impurity segregation during ageing and thus could enhance the structural integrity of the interface of LAS/buttering weld [24].

Ductility dip cracking (DDC) is another concern for DMW particularly in WMs, which has a negative influence on the total lifetime and the reliability of the key components with its high cracking susceptibility [42]. With the heat inflow of multi-pass welding, intergranular solid-state DDC may form between migrated grain boundaries with the sufficient activation energy in as-welded interdendritic grain boundaries and decreased ductility in the temperature range of 0.5–0.8 of their melting points [85]. However, DDC was not found in the investigated DMWs. Both the double-sided buttering technique with the selected parameters as well as the NG welding process used seems to ensure a low susceptibility to DDC.

5.2.2 Microstructure on local mechanical properties

A detailed understanding of metallurgical boundaries, phases and properties at the FB regions can provide more reliable integrity assessment of DMW joints, which is however not required in the existing codes [86]. This chapter discusses the effect of FB microstructure and mismatch on the DMW structural integrity.

The mismatch in local mechanical properties in the FBs has a direct influence on the local fracture resistance and cracking susceptibility of DMW [8]. Earlier fracture mechanical tests on NG-DMWs [76] have demonstrated abrupt crack path deviations from the original crack initiation position into the neighbouring microstructures (*e.g.* the CDZ) and this deflection tendency is affected by the strength mismatch state and the local microstructures. Nevasmaa *et al.* [76] suggested that the increased strength mismatch was responsible for the lowered fracture resistance in the near-interface regions between the LAS and the Alloy 52 weld of the NG-DMW. The decrease in fracture resistance was concluded [76] to stem from increased metallurgical constraint and crack (growth) driving force accentuated by the high, local mismatch state, coupled with inherent local inhomogeneity of the near-interface regions.

SE(B) specimens (5 mm thick and 10 mm wide) were tested in the temperature range of –130 °C to –180 °C. Preliminary study on the fracture surfaces and cross-sections of the brittle fracture toughness specimens to analyse the fracture path deviation in terms of FB microstructure was performed. In Figure 107 is shown a horizontal cross-section of a specimen with the notch placed nominally at 0.3 mm from the FB in the HAZ and a variety of FB microstructures is revealed. Figure 107(a) is a LOM image after etching, where the white area in the middle along the FB is a swirl. The horizontal cross-section was prepared near the brittle fracture crack initiation site. The crack has propagated mainly along the FB and in the HAZ, and the weld bead solidification and FB microstructures appear to have an effect on the crack path. With a swirl or a distinct type-B FB microstructure (Figure 107(b,c)), the fracture deviates into the HAZ but with a type-A FB microstructure (Figure 107(d)) the crack propagates very near to or at the FB. Further investigations are ongoing to investigate the effect of *e.g.* carbides on the fracture behaviour, and how the local tempered martensite influences the interface toughness and if the HAZ is

weakened due to elemental diffusion. The varying FB microstructure makes the brittle fracture path propagation less predictable.

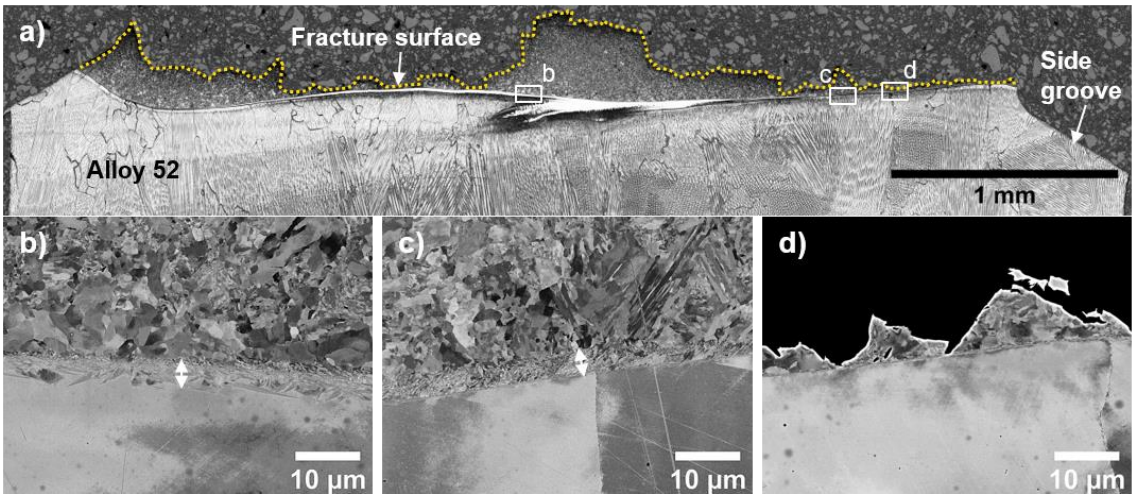

Figure 107: Horizontal cross-section of a fracture toughness specimen with pre-crack notch at 0.3 mm from the FB, (a) LOM image after etching shows a swirl in the middle and deviating fracture path in the LAS HAZ (yellow line), (b-c) tempered martensite microstructure at the FB with fracture deviated away from the FB, (d) no distinct FB microstructure and fracture along the FB.

5.2.3 Fracture mechanical behaviour of Ringhals mock-up

The crack path behaviour for the cracks of the Ringhals mock-up is similar to the TVO mock-up. The HAZ crack close to the FB deviate to the FB and propagate along the FB in close vicinity of the FB. The WM cracks do not deviate to the FB.

In the ductile regime, HAZ cracks approximately 1 mm from the FB deviate to the FB. In the DBT region, the HAZ crack path deviation to the FB might stop after the distance between the crack and the FB exceeds 0.5 mm. For TVO mock-up, this distance is 0.3 mm. The variations are affected by the strength mismatch profile. For the Ringhals mock-up, the hardness profile is farther from the FB.

The fracture toughness of the Ringhals mock-up is higher in the HAZ close to the FB. Figure 108 compares J_{1mm} values for the two mock-ups. Figure 109 show that the fracture toughness of the Ringhals mock-up is also slightly higher in the DBT region. Major difference between the FB of the two mock-ups is the PWHT and the manufacturing where for Ringhals DMW a buttering layer is manufactured. These factors are known to affect the mechanical properties.

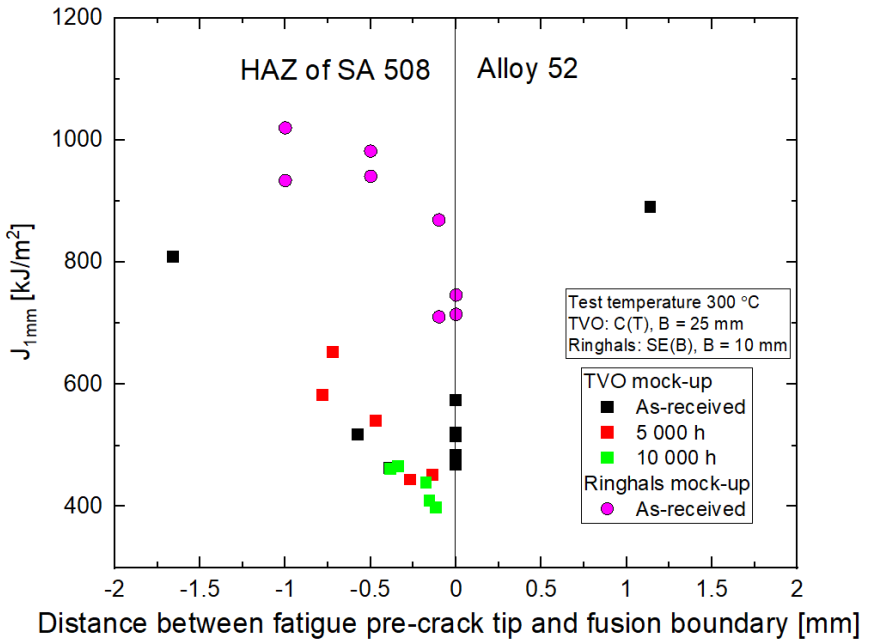

Figure 108. The comparison of J_{1mm} values of the Ringhals and TVO mock-ups.

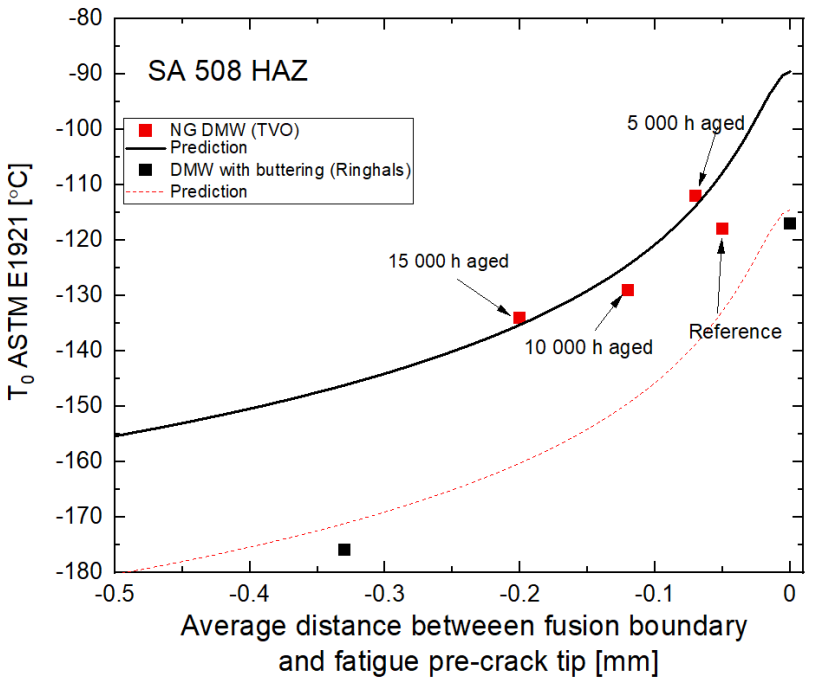

Figure 109. Comparison of TVO and Ringhals T_0 results.

Figure 110 shows the strength behaviour across the LAS/WM FB for the Ringhals mock-up. Peak strength is obtained approximately 1 mm from the FB. The strength is lower at 300 °C. The strength profile is similar to another Alloy 52 DMW investigated in Euratom project MULTIMETAL, but the strength is higher. Possibly, the strength peak is also farther from the FB. However, the strength variations are relatively intense compared to the size of the tensile specimens and a better estimation of the peak location is obtained using hardness measurements. The MULTIMETAL DMW is similar to the TVO mock-up.

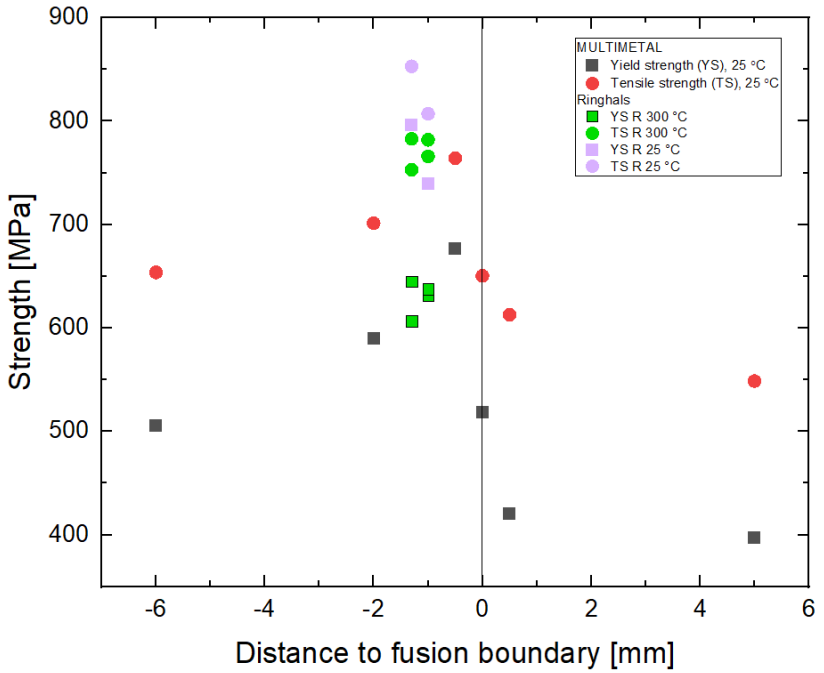

Figure 110. Comparison of tensile properties of the DMWs, Ringhals and MULTIMETAL. Both DMWs are Alloy 52 DMWs.

6 Conclusions

The main conclusions from the extensive investigations performed and reported in this report are summarized as following.

6.1 TVO mock-up

Since the microstructure adjacent to the FB controls the fracture behaviour and carbides can act as brittle fracture initiators, the microstructure and carbides crystal structure, chemistry, morphology and size in the fusion boundary (FB) and low alloy steel (LAS) heat-affected zone (HAZ) were analysed for the narrow-gap (NG) SA508/Alloy 52 dissimilar metal weld (DMW) mock-up, which is fully representative of an actual nuclear component. Based on the obtained results, the following conclusions can be drawn:

- The microstructure and precipitations in the LAS FB carbide precipitation zone (CPZ, normally up to 1.5 µm from FB), carbon depletion zone (CDZ, up to 40–50 µm from FB) and HAZ (up to 2 mm from FB) were analysed.
- The nanometre precipitates at FB are nano carbides in the NG thermally-aged (TA for 15 000 h) material and nano nitrides in the NG as-received (AR) material. These nanometre Cr/Mn rich carbides at the FB have fixed Bagaryatskii orientation relationship with a BCC matrix, which is reported for the first time in a DMW.
- In the CPZ, the number of carbides is lower and the size of the carbides is smaller in the AR material than in the TA material. Long-term thermal aging widens the width of the CPZ.
- The dominant carbides are $(Fe, Cr, Mn)_3C$ in CPZ but $(Fe, Mn, Cr)_3C$ in CDZ and HAZ. These carbides are M_3C θ carbides instead of $M_{23}C_6$ (that is widely mix-indexed in literatures).
- Long-term thermal aging coarsens the carbides size in HAZ (up to 2 mm from FB) and the length of the carbide can be a magnitude longer after aging. The fraction of grains devoid of visible carbides in HAZ is higher in the NG TA material than in the NG AR material.
- Long-term thermal aging increases microhardness peak close to the FB in the HAZ. The microhardness result is different from NIWEL project,

possibly due to a finer step size and more controllable indentations in the current project.

- After thermal aging, the higher microhardness mismatch at the FB, the larger/denser carbides in the CPZ and the coarsened carbides and local carbide-free grains in the HAZ may lead to a local brittle zone and may cause low fracture toughness.
- There is no evidence of a significant phosphorus segregation to grain boundaries in HAZ due to thermal ageing, based on the APT measurements performed on a few specimens within HAZ grains. The APT measurements suggest that about half of the phosphorus is segregated already before aging. Additional future work is needed to get a more statistical and representative estimate of the phosphorus segregation.

In this study, the fracture properties were characterized according to ASTM E1921 to obtain transition temperature T_0 and EN ISO 148-1 to obtain T_{28J} and T_{41J}. The impact toughness testing was done using an instrumented impact hammer to obtain the arrest force and arrest toughness. The crack was nominally placed at the FB between the weld metal (WM) and the LAS.

- T_0 results in a lower shift than impact toughness. The crack location corrected T_0 shift is 10 °C after 15 000 h at 400 °C, whereas ΔT_{28J} is 49 °C. The ΔT_{28J} and ΔT_{41J} saturate after 10 000 h at 400 °C, while ΔT_0 appears to saturate after 5 000 h.
- The crack location corrected T_0 after 15 000 h aging is -110 °C and T_{28J} = -5 °C.
- The initiation of brittle fracture tends to occur next to the FB in the CDZ. For cracks farther from the FB located in the HAZ, the crack deviates to the FB and progresses in that region, in most cases.
- The T_0 for the NG DMW after 15 000 h of aging at 400 °C is of the same magnitude as after 10 000 h, 5 000 h and in AR references condition, as long as the crack is close enough to the FB. For cracks farther away, the fracture toughness appears to be lower.
- The thermal aging mechanism can affect more the crack arrest and propagation mechanism than the initiation mechanism. The crack arrest toughness increases with 35 °C after 15 000 h at 400 °C.
- The thermal aging treatment of the NG Alloy 52 DMW does not significantly affect the T_0 reference temperature of the FB. Further research is needed to better understand the lower boundary fracture toughness behaviour at approximately 300 µm from the FB.

6.2 Ringhals mock-up

The microstructure, crystal structure, elemental diffusion and mismatch of the bainitic SA508/austenitic Ni-base Alloy 52 buttering interface in the Ringhals DMW mock-up consisting of Alloy 52 buttering on both sides was studied in this work. The mock-up is the first-of-a-kind in Europe and is representative of Ringhals pressurizer

surge nozzle DMW repair solution. The main nominal differences between the two mock-ups are the welding orientation between the buttering and the NG weld, and post-weld heat treatment (PWHT) conditions.

- Three types of FBs were identified in Ringhals mock-up: a type-A narrow FB (~80–85% of whole FB and with width <1 μm), a type-B feathery-like tempered martensitic FB with fine lath-like microstructure (~15% of whole FB and up to 8 μm in width) and a type-C wide partially-mixed zone (PMZ, ~1–2% of the whole FB and up to 25 μm in width).
- In TVO NG mock-up, majority of the SA508/A52 FB is a narrow and straight boundary and few large swirls with PMZ, where also type-II boundaries were found on the weld side. In Ringhals mock-up, in addition to the mostly narrow and straight FB, additionally tempered martensitic transition zone and PMZ were observed (as reported in the last bullet point). No significant swirls or type-II boundaries were found in Ringhals mock-up, which may be due to the different welding orientation affecting the weld pool mixing.
- In Ringhals mock-up, the macro- and micro-hardness peak was found in the LAS HAZ and the nano-hardness peak was observed within the FB region, particularly for the type-B FB. The Ringhals mock-up has overall higher hardness than the TVO NG mock-up of ~20 HV. In the TVO NG mock-up, the HV0.3 revealed a soft zone next to the HAZ hardness peak.
- The nanoindentation hardness peak was observed at the type-B FB in Ringhals mock-up. The type-C PMZ FB did not show an evident nano-hardness peak. The nanoindentation hardness peak was observed in the A52 in TVO NG mock-up. The CDZ in the TVO NG mock-up is relatively wider, more homogeneous and lower in hardness compared to that in Ringhals mock-up. The wider CDZ and the observed nano-hardness peak in the A52 side of the DMW interface in TVO NG mock-up compared to the Ringhals mock-up, are likely results of accentuates carbon migration and enhancement of the formation of carbon pile-up.
- The relatively high local heat input-induced diffusion at the type-C PMZ FB in Ringhals mock-up promotes the mixing of BCC and FCC phases and grain coarsening in LAS adjacent to the FB, resulting into the low bound nano-hardness in Alloy 52 buttering and the nearly constant chemical composition in the PMZ.
- The rapid cooling rate together with carbide precipitations at the type-B FB in Ringhals mock-up leads to the nano-hardness peak with the presence of tempered martensite at the transition zone and result in a strong strength mismatch between the weld and LAS.
- The XRD analysis revealed the BCC and FCC crystal structures at the type-B FB in Ringhals mock-up, but no tetragonal martensite phase was observed. The relative volume fraction of martensite at the FB is low and likely the martensite has lost its tetragonality due to tempering.
- The carbide density and distribution evolve with the distance from the FB in the LAS side in Ringhals mock-up. At the FB the carbide density is the

highest. Carbide density is significantly reduced in the CDZ adjacent to the FB. Beyond the first 100 µm of the CDZ to HAZ transition, the carbide density increases again to that of the regular distribution of carbides in a LAS bainitic microstructure.

- The dominant carbides are (Fe, Mn, Cr)$_3$C in HAZ of Ringhals mock-up, which is similar as in TVO NG mock-up. However, the (Fe, Mn, Cr)$_3$C carbides are with relatively larger Mn content in TVO mock-up whereas with almost equal contents of Mn and Cr in Ringhals mock-up.
- The FB microstructure have an effect on brittle fracture crack path, as with a swirl or type-B tempered martensitic FB the crack grows in the LAS HAZ and with a type-A narrow FB the crack propagates along or adjacent to the FB.

The miniature tensile testing, J-R testing, transition temperature T_0 and impact toughness testing were performed.

- The T_0 transition temperature for the DMW with buttering is −117 °C, indicating marginally higher toughness compared to the NG DMW. The cracks close to the FB (approximately 200 µm) in both DMWs deviate from the HAZ towards the FB. The fracture toughness increases with distance to FB, at least up to 0.3 mm from the FB.
- Future investigations should also focus on understanding the significance on fracture toughness of the region 0.3 mm from the FB in the HAZ. The FB microstructures*, i.e.*, tempered martensite or elemental dilution and PMZ, may increase the local FB toughness properties, and promote cracking in the local regions in HAZ.
- At 300 °C, the J-R curves are continuous and rising. The fracture mode is stable tearing. Compared to the TVO mock-up, the fracture toughness is higher. J_{1mm} at FB is 710 kJ/m^2, where a local minimum is obtained.
- The crack path behaviour in the HAZ is similar to previous investigations. The crack deviates to the FB and grows along the FB.
- The yield strength of the hard zone in the HAZ is approximately 750 MPa at room temperature. The region has higher strength compared to a similar Alloy 52 DMW.

The results contribute to long-term operation assessment of nuclear power plants, and development of analysis and characterization methods for DMWs related to the effect of crack path and location.

6.3 Future work

Although the FEMMA project during 2020-2022 has been very successful and produced valuable extensive fracture mechanical testing and microstructural analysis data, several key questions remain to be investigated:

(i) In FEMMA, a Ringhals mock-up has been investigated in as received condition. During 2022-2023, the RPVH from Ringhals 2 unit will be harvested and cut, where the decommissioned thermally aged DMW will become available after

21 full years of operation at 323 °C. This offers a unique opportunity to study the effect of thermal aging and the validation of the lab thermal aging conditions (by comparing the lab furnace accelerated thermal aging condition of Ringhals mock-up to the decommissioned nuclear power plant component).

(ii) Earlier investigations have demonstrated that the low toughness values are frequently associated with near-interface microstructures in the immediate vicinity of the FB. The present results show, this is not always the case and low toughness values are also encountered in HAZ microstructures further away from the FB, at distances where cracks no longer deviate towards the FB because of mismatch. The underlying reasons of this phenomenon have remained unexplained. Why is the fracture toughness of specimens with crack path following the HAZ with a distance of around 300 µm to FB much lower than the fracture toughness of specimens with crack path following the FB? What is the structural significance of this result? What are the mechanisms for the low toughness value? Are these low toughness values originating from effects of thermal aging or just local microstructural feature in the HAZ? Detailed investigation of the low toughness T_0 specimens via cross sectional metallography will be important. Moreover, the microstructure analysis should focus also on the LAS HAZ CDZ in addition to the FB region.

(iii) What are the exact effects of notch location on the toughness values and what is the effect of specimen size on T_0? More fracture mechanical testing data on these two respects will be highly valuable.

Continuation of the DMW study is of high importance. Developing and maintaining the knowledge of DMW-related issues is vital for the Nordic nuclear power industry. Project like FEMMA, which is the only research programme on the topic at least in Finland, create a unique opportunity to keep close contacts between researchers and nuclear industry. As the past has shown, *e.g.* new cracking (*e.g.* SCC) issues typically come unexpected, thus proactivity is the wisest way to ensure continuous production of safe nuclear power.

Acknowledgements

The authors wish to express their gratitude for the funding and support from Ringhals AB, OKG AB, Teollisuuden Voima Oyj and VTT Technical Research Centre of Finland within the FEMMA (Forum for the Effect of Thermal Ageing and Microstructure on Mechanical and EAC Behaviour of Ni-based Alloy Dissimilar Metal Welds) research project. The authors also thank NKS for funding the NKS-FEMMA (AFT/NKS-R(22)134/4) project. Ringhals AB and TVO are acknowledged for the delivery of plant-relevant material to the project. The authors would like to thank J. Alhainen, J. Lukin, T. Lehtikuusi, J. Hietikko, J. Saarinen, J. Rantala, J. Leporanta and A. Nurmela for the experimental contributions. The authors would like to thank P. Efsing, B. Forssgren, H. Reinvall and H. Hänninen for suggestions and discussions. The APT experiments were performed at Chalmers Materials Analysis Laboratory (CMAL). The authors also acknowledge the provision of facilities and technical support by Aalto University at OtaNano - Nanomicroscopy Center (Aalto-NMC) and the help on nanoindentation from FemtoTools AG.

References

[1] D. Féron, “Overview of Nuclear Materials and Nuclear Corrosion Science and Engineering,” in *Nuclear Corrosion Science and Engineering*, Woodhead Publishing, 2012, p. 31–56.

[2] D. MacDonald and G. Cragnolino, “Corrosion of Steam Cycle Materials,” in *ASME Handbook on Water Technology for Thermal Power Systems*, ASME, 1989, p. 659–1031.

[3] P. Efsing, B. Forssgren and R. Kilian, “Root cause failure analysis of defected J-groove welds in steam generator drainage nozzles,” in *Proceedings of the Twelfth International Conference on Environmental Degradation of Materials in Nuclear Power Systems-Water Reactors*, 2005.

[4] A. Jenssen, K. Norrgard, J. Lagerstrom, G. Embring, C. Jansson and P. Efsing, “Structural assessment of defected nozzle to safe-end welds in Ringhals-3 and -4,” in *Proc. Fontevraud V Intl. Symp.*, 2000.

[5] P. Efsing and J. Lagerström, “Analysis of a defected dissimilar metal weld in a PWR power plant,” in *10th Int Conf Nucl Eng*, 2002.

[6] S. Yoo, K. Choi, C. Bahn, S. Ki, J. Kim and J. Kim, “Effects of thermal aging on the microstructure of Type-II boundaries in dissimilar metal weld joints,” *Journal of Nuclear Materials,* vol. 459, p. 5–12, 2015.

[7] A. Akhatova, F. Robaut, M. Verdier, M. Yescas, F. Roch, C. Tassin and H. Landeghem, “Microstructural and mechanical investigation of the near fusion boundary region in thermally aged 18MND5 / alloy 52 narrow-gap dissimilar metal weld,” *Materials Science & Engineering A,* vol. 788, no. 139592, 2020.

[8] H. Wang, G. Wang, F. Xuan, C. Liu and S. Tu, “Local mechanical properties of a dissimilar metal welded joint in nuclear power systems,” *Materials Science & Engineering A 568,* p. 108–117, 2013.

[9] A. Blouin, S. Chapuliot, S. Marie, C. Niclaeys and J. Bergheau, “Brittle fracture analysis of Dissimilar Metal Welds,” *Engineering Fracture Mechanics,* vol. 131, p. 58–73, 2014.

[10] Z. Chen, Y. Lu, X. Ding and T. Shoji, “Microstructural and hardness investigations on a dissimilar metal weld between low alloy steel and Alloy 82 weld metal,” *Materials Characterization,* vol. 121, p. 166–174, 2016.

[11] K. Ravikiran, H. Mehtani, K. Sivaprasad, M. Prasad, S. Kumar, P. Singh and M. Ghosh, “Influence of nickel-based buttering material on welded joint between SA508 low alloy steel and 304LN stainless steel,” *International Journal of Pressure Vessels and Piping,* vol. 195, no. 104576, 2022.

[12] H. Ming, J. Wang and E. Han, “Comparative study of microstructure and properties of low-alloy-steel/nickel-based-alloy interfaces in dissimilar metal weld joints prepared by different GTAW methods,” *Materials Characterization,* vol. 139, p. 186–196, 2018.

[13] P. Joly, M. Yescas and E. Keim, “Fracture toughness in the ductile-brittle transition and thermal ageing behavior of decarburized heat affected zone of Alloy 52 dissimilar metal welds of nuclear components,” in *Proceedings of the ASME-2014 Pressure Vessel and Piping Conference*, Anaheim, California, USA, 2014.

[14] P. Aaltonen and H. Hänninen, “Water Chemistry and Behavior of Materials in PWRs and BWRs,” in *IAEA-TECDOC-965*, 1997, p. 205–222.

[15] U. Ehrnstén, “Corrosion and Stress Corrosion Cracking of Austenitic Stainless Steels,” in *Comprehensive Nuclear Materials*, Elsevier Ltd., 2012, p. 93–104.

[16] S. Fyfitch, “Corrosion and Stress Corrosion Cracking of Ni-Base Alloys,” in *Comprehensive Nuclear Materials*, Elsevier Ltd., 2012, p. 69–92.

[17] P. Scott, “Environment Assisted Cracking in Austenitic Components,” *International Journal of Pressure Vessels and Piping,* vol. 65, no. 3, p. 255–264, 1996.

[18] Z. Lu, “Characterization of Microstructure, Local Deformation and Microchemistry in Alloy 690 Heat-Affected Zone and Stress Corrosion Cracking in High Temperature Water,” *Journal of Nuclear Materials,* vol. 465, p. 471–481, 2015.

[19] B. Payne, “Nickel-base Welding Consumables for Dissimilar Metal Welding Applications,” *Metal Construction,* vol. 1, no. 12, p. 79–87, 1969.

[20] F. Cattant, “Materials Ageing in Light Water Reactors,” in *Handbook of Destructive Assays*, Materials Ageing Institute, 2014, p. 1166 .

[21] W.-C. Chung, J.-Y. Huang, L.-W. Tsay and C. Chen, “Microstructure and Stress Corrosion Cracking Behaviour of the Weld Metal in Alloy 52-A508 Dissimilar Welds,” *Materials Transactions, Vol 52, No. 1,* p. 12–19, 2011.

[22] G. Sui, “Stress Corrosion Cracking of Alloy 600 and Alloy 690 in Hydrogen/Steam at 380 °C,” *Corrosion Science,* vol. 39, no. 3, p. 565–587, 1997.

[23] L. Dong, Y. Zhang, Y. Han, Q. Peng and E. Han, “Environmentally assisted cracking in the fusion boundary region of a SA508-Alloy 52M dissimilar weld joint in simulated primary pressurized water reactor environments,” *Corrosion Science,* vol. 190, no. 109668, 2021.

[24] J. Gao, J. Tan, Z. Zhang, M. Jiao, X. Wu, L. Tang and Y. Huang, “Effects of welding columnar grain orientation and strain rate on corrosion fatigue behavior of Alloy 52/52M weld metal in high-temperature water,” *Corrosion Science,* vol. 180, no. 109196, 2021.

[25] K. Choi, S. Yoo, S. Kim, T. Kim, J. Ham, J. Lee and J. Kim, “Microstructural evolution and corrosion behaviour of thermally aged dissimilar metal welds

of low-alloy steel and nickel-based alloy," *Corrosion Science,* vol. 153, p. 138–149, 2019.

[26] J. Kim, S. Kim, K. Choi, C. Bahn, I. Hwang and J. Kim, "In-situ investigation of thermal aging effect on oxide formation in Ni-base alloy/low alloy steel dissimilar metal weld interfaces," *Corrosion Science,* vol. 86, p. 295–303, 2014.

[27] G. Wang, H. Wang, F. Xuan, S. Tu and C. Liu, "Local fracture properties and dissimilar weld integrity in nuclear power plants," *Frontiers of Mechanical Engineering, 8,* p. 283–290, 2013.

[28] Z. Chen and Y. Lu, "TEM Observation of Martensite Layer at the Weld Interface of an A508III to Inconel 82 Dissimilar Metal Weld Joint," *Metallurgical and Materials Transactions A,* vol. 46A, p. 5494–5498, 2015.

[29] M. Ahonen, R. Mouginot, T. Sarikka, S. Lindqvist, Z. Que, U. Ehrnstén, I. Virkkunen and H. Hänninen, "Effect of thermal ageing at 400°C on the microstructure of ferrite-austenite interface of Nickel-base alloy narrow-gap dissimilar metal weld," *Metals, 10,* 2020.

[30] J. Parker and G. Stratford, "Characterisation of microstructures in nickel based transition joints," *Journal of Materials Science,* vol. 35, p. 4099–4107, 2000.

[31] M. Toloczko, "Alloy 152/52-LAS Dilution Zone and Interface/Fusion Line PWSCC Testing. In EPRI 690/152/52 PWSCC Research Collaboration Meeting," EPRI 690/152/52 PWSCC Research Collaboration Meeting, Tampa, FL, 2016.

[32] A. Laukkanen, "Charasteristics Relevant to Ductile Failure of Bimetallic Welds and Evaluation of Transferability of Fracture Properties," *Nuclear Engineering and Design,* vol. 237, pp. 1-15, 2007.

[33] T. Sarikka, "Microstructural, Mechanical, and Fracture Mechanical Characterization of SA 508-Alloy 182 Dissimilar Metal Weld in View of Mismatch State," *International Journal of Pressure Vessels and Piping,* vol. 145, p. 13–22, 2016.

[34] T. Sarikka, "Effect of Mechanical Mismatch on the Fracture Mechanical Behavior of SA 508-Alloy 52 Narrow Gap Dissimilar Metal Weld," *International Journal of Pressure Vessels and Piping,* vol. 157, pp. 30-42, 2017.

[35] J. Hou, Q. Peng, Y. Takeda, J. Kuniya, T. Shoji, J. Wang, E.-H. Han and W. Ke, "Microstructure and mechanical property of the fusion boundary region in an Alloy 182-low alloy steel dissimilar weld joint," *Journal of Materials Science, 45,* p. 5332–5338, 2010.

[36] M. Ahonen, S. Lindqvist, T. Sarikka, R. Mouginot, E. Leskelä, J. Lydman, U. Ehrnstén, P. Nevasmaa, T. Seppänen, P. Arffman and H. Hänninen, "Thermal ageing and mechanical performance of narrow-gap dissimilar metal welds," VTT Technology 333, 2018.

[37] H. Hänninen, "Structural Integrity of Ni-base Alloy Welds," VTT Technology 175, Espoo, 2014.

[38] S. Lindqvist and J. Kuutti, "Dependence between η -factor and crack location relative to a fusion boundary between hard and soft materials in a SE (B) specimen," *Int J Fract,* vol. 211, p. 281–293, 2018.

[39] R. Mouginot, Effect of thermal ageing on Alloys 690 and 52 in pressurized water reactor applications, Doctoral dissertation, Aalto University, 2017.

[40] H. Wang, G. Wang, F. Xuan and S. Tu, “Fracture mechanism of a dissimilar metal welded joint in nuclear power plant,” *Engineering Failure Analysis,* vol. 28, p. 134–148, 2013.

[41] Z. Zhai, H. Abe, Y. Miyahara and Y. Watanabe, “Effects of phosphorus segregation on stess corrosion cracking in the heat-affected zone of a dissimilar weld joint between a Ni-base alloy and a low alloy steel,” *Corrosion Science 92,* p. 32–42, 2015.

[42] J. Gao, J. Tan, M. Jiao, X. Wu, L. Tang and Y. Huang, “Role of welding residual strain and ductility dip cracking on corrosion fatigue behavior of Alloy 52/52M dissimilar metal weld in borated and lithiated high-temperature water,” *Journal of Materials Science & Technology,* vol. 42, p. 163–174, 2020.

[43] J. Kim, K. Choi, C. Bahn and K. J.H., “In situ Raman spectroscopic analysis of surface oxide films on Ni-base alloy/low alloy steel dissimilar metal weld interfaces in high-temperature water,” *Journal of Nuclear Materials,* vol. 449, p. 181–187, 2014.

[44] T. Nelson, J. Lippold and M. Mills, “Nature and evolution of the fusion boundary in ferritic-austenitic dissimilar weld metals, Part 1: Nucleation and growth,” *Welding research,* p. 329–337, 1999.

[45] W. R. Corwin, “Thermal Embrittlement of Reactor Pressure Vessel Steels,” UNT Digital Library, 1995.

[46] J. Hudson, “Thermal Ageing Effects in Structural Steels,” *Theoretical and Applied Fracture Mechanics,* vol. 10, pp. 123-133, 1988.

[47] G. Young, “The Kinetics of Long Range Ordering in Ni-Cr and Ni-Cr-Fe Alloys,” in *Proceedings of the 16th International Conference on the Environmental Degradation of Materials in Nuclear Power Systems - Water Reactors*, 2013.

[48] “Materials Reliability Program: Resistance to Primary Water Stress Corrosion Cracking of Alloy 690 in Pressurized Water Reactors (MRP-258),” EPRI, 2009.

[49] W. Server and M. Brumovský, “International Review of Nuclear Reactor Pressure Vessel Surveillance Programs,” 2018.

[50] A. V. Nikolaeva, Y. Nikolaev and A. Kryukov, “Grain boundary embrittlement due to reactor pressure vessel annealing,” *J Nucl Mater,* vol. 211, 1994.

[51] B. Gurovich, A. Chernobaeva, D. Erak, E. Kuleshova, D. Zhurko and V. Papina, “Chemical composition effect on VVER-1000 RPV weld metal thermal aging,” *J Nucl Mater,* vol. 465, 2015.

[52] Y. Shtrombakh, B. Gurovich, E. Kuleshova, A. Frolov, S. Fedotova and D. Zhurko, “Effect of Ni content on thermal and radiation resistance of VVER RPV steel,” *J Nucl Mater,* vol. 461, p. 292–300, 2015.

[53] M. Boåsen, K. Lindgren, M. Öberg, M. Thuvander, J. Faleskog and P. Efsing, “Analysis of thermal embrittlement of a low alloy steel weldment using fracture toughness and microstructural investigations,” *Eng Fract Mech,* vol. 108248, 2022.

[54] “Integrity of Reactor Pressure Vessels in Nuclear Power Plants: Assessment of irradiation embrittlement effects in reactor pressure vessel steels,” IAEA, 2009.

[55] I. Vatter, C. Hippsley and S. Druce, “Review of thermal ageing data and its application to operating reactor pressure vessels,” *Int J Press Vessel Pip,* vol. 54, p. 31–48, 1993.

[56] H. Nakata, K. Fujii, K. Fukuya, R. Kasada and A. Kimura, “Grain boundary phosphorus segregation in thermally aged low alloy steels,” *J Nucl Sci Technol,* vol. 43, 2006.

[57] R. Nanstad, D. Mccabe, M. Sokolov, C. English and S. Ortner, “Investigation of temper embrittlement in reactor pressure vessel steels following thermal aging, irradiation and thermal annealing,” in *Eff Radiat Mater 20h Int Symp ASTM STP*, 2001.

[58] S. Druce, G. Gage and G. Jordan, “Effect of ageing on properties of pressure vessel steels,” *Acta Metall,* vol. 34, 1986.

[59] G. Gage, S. Druce and E. Popkiss, “Thermal ageing embrittlement of the heat-affected zone in a PWR RPV steel weldment.,” in *Proceedings of the topical meeting on nuclear power plant life extension*, 1988.

[60] P. Joly, F. Roch and C. Primault, “Effect of thermal ageing on properties of pressure vessel low alloy steel,” in *ASME PVP*, 2013.

[61] Z. Que, M. Lindroos, J. Lydman, N. Hytönen, S. Lindqvist, P. Efsing, P. Nevasmaa and P. Arffman, “Brittle fracture initiation in decommissioned boiling water reactor pressure vessel head weld,” *Journal of Nuclear Materials,* vol. 569, no. 153925, 2022.

[62] N. Hytönen, Z. Que, S. Lindqvist, J. Lydman, Y. Ge, I. Virkkunen, U. Ehrnstén, P. Rautala, P. Efsing and B. Forssgren, “Fusion Boundary Microstructure and Fracture Behaviour of a narrow-gap Alloy 52 Dissimilar Metal Weld and an Alloy 52 Dissimilar Metal Weld with Buttering,” in *International Symposium Contribution of Materials Investigations and Operating Experience to LWRs’ Safety, Performance and Reliability, FONTEVRAUD 10*, Avignon, France, 2022.

[63] N. Hytönen, Y. Ge, Z. Que, S. Lindqvist, J. Lydman, U. Ehrnstén, P. Rautala, I. Virkkunen and P. Efsing, “Effect of Microstructure on Mechanical Behaviour of Ni-base Alloy Dissimilar Metal Welds,” in *The 20th International Conference on Environmental Degradation of Materials in Nuclear Power Systems-Water Reactor meeting, ED2021-17104*, Colorado, USA, 2022.

[64] L. Lutterotti, “Maud: a Rietveld analysis program designed for the internet and experiment integration,” *Acta Crystallographica Section A: Foundations of Crystallography,* vol. 56, no. s1, p. 54, 2000.

[65] Y. Ge, Z. Que, K. Lindgren, N. Hytönen and M. Thuvander, “Effect of Thermal Aging on Microstructure and Carbides of SA508/Alloy 52 Dissimilar Metal Weld,” *Materials Characterization,* vol. 200, no. 112880, 2023.

[66] Y. Bagaryatskii, “Veroyatnue mechanezm raspada martenseeta,” *Dokl. Akad. Nauk SSSR,* vol. 73, p. 1161, 1950.

[67] L. Zhang, B. Radiguet, P. Todeschini, C. Domain, Y. Shen and P. Pareige, “Investigation of solute segregation behavior using a correlative EBSD/TKD/APT methodology in a 16MND5 weld,” *Journal of Nuclear Materials,* vol. 523, pp. 434-443, 2019.

[68] M. Thuvander, J. Weidow, J. Angseryd, L. Falk, F. Liu, M. Sonestedt, K. Stiller and H. Andren, “Quantitative atom probe analysis of carbides,” *Ultramicroscopy,* vol. 111, no. 6, 2011.

[69] N. Hytönen, Y. Ge, Z. Que, S. Lindqvist, P. Nevasmaa, I. Virkkunen and P. Efsing, “Study of Fusion Boundary Microstructure and Local Mismatch of SA508/Alloy 52 Dissimilar Metal Weld,” *Journal of Nuclear Materials,* vol. 583, no. 154558, 2023.

[70] K. Wallin, “Master Curve analysis of inhomogeneous ferritic steels,” *Engineering Fracture Mechanics,* vol. 71, p. 2329–2346, 2004.

[71] S. Lindqvist, N. Hytönen, L. Sirkiä, P. Arffman, J. Lydman, Y. Ge, P. Nevasmaa and Z. Que, “Fracture in the Ductile-To-Brittle Transition Region of A Narrow-Gap Alloy 52 and Alloy 52 Dissimilar Metal Weld With Buttering,” in *ASME PVP*, Las Vegas, US, 2022.

[72] S. Lindqvist, M. Ahonen, J. Lydman, P. Arffman and H. Hänninen, “A crack-location correction for T0 analysis of an Alloy 52 dissimilar metal weld,” *Eng Fract Mech,* vol. 214, 2019.

[73] K. Wallin, Fracture toughness of engineering materials - estimation and application, EMAS publishing, 2011.

[74] S. Kou, Welding Metallurgy, 2nd edition, John Wiely & Sons, Inc., 2003.

[75] S. Lindqvist, Z. Que, P. Nevasmaa and N. Hytönen, “The effect of thermal aging on fracture properties of a narrow-gap Alloy 52 dissimilar metal weld,” *Engineering Fracture Mechanics,* vol. 281, no. 109056, 2023.

[76] P. Nevasmaa, P. Holmström, P. Karjalainen-Roikonen, T. Sarikka, M. Ahonen, R. Mouginot, U. Ehrnstén, A. Brederholm, P. Aaltonen and H. Hänninen, “Fracture mechanical characterisation of ferrite-austenite dissimilar metal welds (DMWs) for elevated temperature service in view of metallurgical mismatch,” in *International Conference on Life Management and Maintenance for Power Plants*, Helsinki, 2013.

[77] K. Choi, J. Kim, B. Lee, C. Bahn and J. Kim, “Effects of thermal aging on microstructures of low alloy steel–Ni base alloy dissimilar metal weld interfaces,” *Journal of Nuclear Materials,* vol. 441, p. 493–502, 2013.

[78] K. Wallin, A. Laukkanen and P. Nevasmaa, “Risk informed plant life management - application of the Master-Curve approach for hydrotreating reactors in an oil refinery,” in *Plant life Manag. - Prog. Struct. Integr.*, Espoo: VTT, 2003.

[79] M. Kocak, S. Webster, J. Janosch, R. Ainsworth and R. Koers, FITNET - fitness for service - fracture, fatigue, creep, corrosion., Germany, 2008.

[80] M. Yescas, P. Joly and F. Roch, “Thermal aging assessment and microstructural investigations of Alloy 52 dissimilar metal welds for nuclear components,” in *Proc ASME 2019 Press Vessel Pip Conf*, 2019.

[81] S. Wang, J. Ding, H. Ming, Z. Zhang and J. Wang, “Characterization of low alloy ferritic steel–Ni base alloy dissimilar metal weld interface by SPM techniques, SEM/EDS, TEM/EDS and SVET,” *Materials Characterization,* vol. 100, p. 50–60, 2015.

[82] Z. Chen, B. Zhao, T. Liu, Y. Lu and T. Shoji, “Oxidation behavior of the dilution zone of a dissimilar metal weld between low alloy steel and Alloy 82

in high temperature water," *Materials Characterization,* vol. 155, no. 109816, 2019.

[83] X. Liu, F. Zhong, J. Zhang, M. Zhang, M. Kang and Z. Guo, "Lattice-parameter variation with carbon content of martensite I. X-ray diffraction experimental study," *Physical Review B,* vol. 52, pp. 9970-9978, 1995.

[84] T. W. Nelson, J. C. Lippold and M. J. Mills, "Nature and evolution of the fusion boundary in ferritic-austenitic dissimilar weld metals, Part 2: On-cooling transformations," *Welding Journal, 79,* p. 267–277, 2000.

[85] H. Liang, C. Wang and Z. Wu, "Corrosion behavior of alloy 52M and 52MSS weld surfacing," *International Journal of Pressure Vessels and Piping,* vol. 191, no. 104356, 2021.

[86] D. Rathod, S. Pandey, P. Singh and S. Kumar, "Microstructure-dependent fracture toughness (JIC) variations in dissimilar pipe welds for pressure vessel system of nuclear plants," *Journal of Nuclear Materials,* vol. 493, pp. 412-425, 2017.

Appendix A: Publications and oral presentations from FEMMA project

Multiple peer reviewed conference proceedings and journal papers are published in FEMMA project:

- S. Lindqvist, Z. Que, P. Nevasmaa and N. Hytönen, “The effect of thermal aging on fracture properties of a narrow-gap Alloy 52 dissimilar metal weld,” *Engineering Fracture Mechanics* 281:109056, 2023, 10.1016/j.engfracmech.2023.109056.
- Y. Ge, Z. Que, K. Lindgren, N. Hytönen, M. Thuvander, “Effect of Thermal Aging on Microstructure and Carbides of SA508/Alloy 52 Dissimilar Metal Weld,” *Materials Characterization* 200:112880, 2023, 10.1016/j.matchar.2023.112880.
- N. Hytönen, Y. Ge, Z. Que, S. Lindqvist, P. Nevasmaa, I. Virkkunen and P. Efsing, “Study of Fusion Boundary Microstructure and Local Mismatch of SA508/Alloy 52 Dissimilar Metal Weld,” *Journal of Nuclear Materials* 583:154558, 2023, 10.1016/j.jnucmat.2023.154558.
- Lindqvist, S., Hytönen, N., Sirkiä, L., Arffman, P., Lydman, J., Ge, Y., Nevasmaa, P. & Que, Z., “Fracture in the Ductile-To-Brittle Transition Region of A Narrow-Gap Alloy 52 and Alloy 52 Dissimilar Metal Weld With Buttering,” ASME PVP, Nov 2022, doi: 10.1115/PVP2022-80690.
- N. Hytönen, Y. Ge, Z. Que, S. Lindqvist, J. Lydman, U. Ehrnstén, P. Rautala, I. Virkkunen and P. Efsing, “Effect of Microstructure on Mechanical Behaviour of Ni-base Alloy Dissimilar Metal Welds,” The 20th International Conference on Environmental Degradation of Materials in Nuclear Power Systems-Water Reactor meeting, ED2021-17104. 2022, Colorado, USA.
- N. Hytönen, Z. Que, S. Lindqvist, J. Lydman, Y. Ge, I. Virkkunen, U. Ehrnstén, P. Rautala, P. Efsing, B. Forssgren, Fusion Boundary Microstructure and Fracture Behaviour of a narrow-gap Alloy 52 Dissimilar Metal Weld and an Alloy 52 Dissimilar Metal Weld with Buttering, International Symposium Contribution of Materials Investigations and Operating Experience to LWRs’ Safety, Performance and Reliability, FONTEVRAUD 10, September 2022, Avignon, France.

Oral presentations on FEMMA progress were given at:

- EPRI Alloy 690/52/152 Primary Water Stress Corrosion Cracking Research Collaboration Meetings, Jan 2021 and Dec 2021, online.
- International Cooperative Group on Environmentally-Assisted Cracking (ICG-EAC) meeting, May 2022, Tampere, Finland.
- European Conference on Fracture 2022, June 2022, Madeira, Portugal
- ASME Pressure Vessels & Piping Conference, July 2022, Las Vegas, USA.

- International Symposium Contribution of Materials Investigations and Operating Experience to LWRs' Safety, Performance and Reliability, FONTEVRAUD 10, September 2022, Avignon, France.

Series title and number

VTT Technology 420

Title	**Forum for the Effect of Thermal Aging and Microstructure on Mechanical and EAC Behaviour of Ni-base Alloy Dissimilar Metal Welds (FEMMA)**
Author(s)	Zaiqing Que, Sebastian Lindqvist, Noora Hytönen, Yanling Ge, Pekka Nevasmaa, Jari Lydman, Laura Sirkiä, Pentti Arffman, Antti Forsström, Ulla Ehrnstén
Abstract	Dissimilar metal welds (DMWs) are commonly used to join austenitic and ferritic components in the reactor coolant pressure boundary and can become potential concerns regarding the structural integrity of the nuclear power systems, structures and components. In particular, the knowledge on the local strength mismatch at the low alloy steel (LAS)/nickel-based alloy weld metal interface upon post-weld heat treatment (PWHT) and during long-term ageing is lacking. Understanding the fracture mechanical and microstructural changes occurring at the fusion boundary after buttering, welding, PWHT and long-term ageing is crucial for both the improvement of nuclear component integrity and to ensure safe long-term operation. In this study, materials representative of actual power plant components are studied, including a Ringhals SA508/Alloy52 DMW mock-up consisting of Alloy 52 buttering on both sides and a TVO narrow gap DMW mock-up. The project deals with the structural integrity, long-term operation, and ageing management. The technical results provide a basis for assessment of long-term operation for the Finnish and Swedish nuclear power plants for both the operators and the regulatory perspectives.
ISBN, ISSN, URN	ISBN 978-951-38-8783-4 ISSN-L 2242-1211 ISSN 2242-122X (Online) DOI: 10.32040/2242-122X.2023.T420
Date	June 2023
Language	English, Finnish abstract
Pages	141 p. + app. 2 p.
Name of the project	FEMMA
Commissioned by	
Keywords	Dissimilar metal weld, Alloy 52, fusion boundary, characterisation, fracture mechanical test
Publisher	VTT Technical Research Centre of Finland Ltd P.O. Box 1000, FI-02044 VTT, Finland, Tel. 020 722 111, https://www.vttresearch.com

Julkaisun sarja ja numero

VTT Technology 420

Nimeke	**Forum for the Effect of Thermal Aging and Microstructure on Mechanical and EAC Behaviour of Ni-base Alloy Dissimilar Metal Welds (FEMMA)**
Tekijä(t)	Zaiqing Que, Sebastian Lindqvist, Noora Hytönen, Yanling Ge, Pekka Nevasmaa, Jari Lydman, Laura Sirkiä, Pentti Arffman, Antti Forsström, Ulla Ehrnstén
Tiivistelmä	Erilaisia metallihitsejä (DMW) käytetään yleisesti yhdistämään austeniittisia ja ferriittisiä komponentteja reaktorin jäähdytysaineen painerajalla, ja niistä voi tulla potentiaalisia ongelmia ydinvoimajärjestelmien, -rakenteiden ja -komponenttien rakenteellisen eheyden suhteen. Erityisesti puuttuvat tiedot paikallisesta lujuuserosta matalaseosteisen teräksen (LAS) ja nikkelipohjaisten seosmetallien rajapinnassa hitsin jälkeisessä lämpökäsittelyssä (PWHT) ja pitkäaikaisen vanhenemisen aikana. Voitelun, hitsauksen, PWHT:n ja pitkäaikaisen vanhentamisen jälkeen fuusiorajalla tapahtuvien murtumismekaanisten ja mikrorakenteellisten muutosten ymmärtäminen on ratkaisevaa sekä ydinkomponenttien eheyden parantamisen että turvallisen pitkän aikavälin toiminnan varmistamiseksi. Tässä tutkimuksessa tutkitaan todellisia voimalaitoksen osia edustavia materiaaleja, mukaan lukien Ringhals SA508/Alloy52 DMW-maketti, joka koostuu Alloy 52 -voiteesta molemmilta puolilta, sekä TVO:n kapearakoinen DMW-malli. Projekti käsittelee rakenteellista eheyttä, pitkäaikaista toimintaa ja ikääntymisen hallintaa. Tekniset tulokset antavat pohjan Suomen ja Ruotsin ydinvoimalaitosten pitkän aikavälin toiminnan arvioinnille sekä toiminnanharjoittajien että viranomaisnäkökulmasta. Hanke edistää tiedon siirtoa, parantaa ydinmateriaalien ja murtumismekaniikan osaamista sekä vahvistaa yhteyksiä ja kokemusten vaihtoa pohjoismaisten tutkimusorganisaatioiden, yliopistojen, teollisuuden, viranomaisten ja erityisesti nuoren sukupolven välillä.
ISBN, ISSN, URN	ISBN 978-951-38-8783-4 ISSN-L 2242-1211 ISSN 2242-122X (Verkkojulkaisu) DOI: 10.32040/2242-122X.2023.T420
Julkaisuaika	Kuukausi 2023
Kieli	Englanti, suomenkielinen tiivistelmä
Sivumäärä	141 s. + liitt. 2 s.
Projektin nimi	FEMMA
Rahoittajat	
Avainsanat	
Julkaisija	Teknologian tutkimuskeskus VTT Oy PL 1000, 02044 VTT, puh. 020 722 111, https://www.vtt.fi/

Forum for the Effect of Thermal Aging and Microstructure on Mechanical and EAC Behaviour of Ni-base Alloy Dissimilar Metal Welds (FEMMA)

Dissimilar metal welds (DMWs) are commonly used to join austenitic and ferritic components in the reactor coolant pressure boundary and can become potential concerns regarding the structural integrity of the nuclear power systems, structures and components. In particular, the knowledge on the local strength mismatch at the low alloy steel (LAS)/nickel-based alloy weld metal interface upon post-weld heat treatment (PWHT) and during long-term ageing is lacking. Understanding the fracture mechanical and microstructural changes occurring at the fusion boundary after buttering, welding, PWHT and long-term ageing is crucial for both the improvement of nuclear component integrity and to ensure safe long-term operation. In this study, materials representative of actual power plant components are studied, including a Ringhals SA508/Alloy52 DMW mock-up consisting of Alloy 52 buttering on both sides and a TVO narrow gap DMW mock-up. The project deals with the structural integrity, long-term operation, and ageing management. The technical results provide a basis for assessment of long-term operation for the Finnish and Swedish nuclear power plants for both the operators and the regulatory perspectives. The project promotes the knowledge transfer, improve the nuclear materials and fracture mechanics competence and strengthen the connections and experience exchange between the Nordic research organizations, universities, industries, authorities, and especially the young generation.

ISBN 978-951-38-8783-4
ISSN-L 2242-1211
ISSN 2242-122X (Online)
DOI: 10.32040/2242-122X.2023.T420

VTT

beyond the obvious